UNIVERSITY OF CALIFORNIA
RIVERSIDE

Synthesis and Characterization of Ternary Layered Transition Metal Borides and Chalcogenides for Energy Applications

A Dissertation submitted in partial satisfaction
of the requirements for the degree of

Doctor of Philosophy

in

Materials Science and Engineering

by

Amir Ardalan Rezaie

September 2021

Dissertation Committee:
Dr. Boniface Fokwa, Chairperson
Dr. Suveen Mathaudhu
Dr. Pingyun Feng

The Dissertation of Amir Ardalan Rezaie is approved:

Committee Chairperson

University of California, Riverside

Acknowledgments

The text in this dissertation, is in part or in full, is a reprint of the materials as they appear in the following publications. The co-author (supervisor) Prof. Boniface Fokwa listed in the publications directed and supervised the research which forms the basis for this dissertation:

Chapter 3: Rezaie AA, Yan Z, Scheifers JP, Zhang J, Guo J, Fokwa BP. Synthesis and Li-ion electrode properties of layered MAB phases Ni n+ 1 ZnB n (n= 1, 2). Journal of Materials Chemistry A. 2020;8(4):1646-51.

Chapter 4: Rezaie AA, Lee E, Yapo JA, Fokwa BP. Highly Active and Abundant MAB Phases Nin+ 1ZnBn (n= 1, 2) toward Hydrogen Evolution. Advanced Energy and Sustainability Research.:2100052.

Chapter 6: Rezaie AA*, Lee E*, Luong D*, Yapo JA, Fokwa BP. Abundant Active Sites on the Basal Plane and Edges of Layered van der Waals Fe3GeTe2 for Highly Efficient Hydrogen Evolution. ACS Materials Letters. 2021 Feb 22;3(4):313-9.

(Rezaie AA*, Lee E*, Luong D* are co-first authors and contributed equally)

I would like to thank my co-first authors (Eunsoo Lee and Diana Luong), my co-authors and all those who contributed to this work and the above publications for providing technical expertise. I sincerely acknowledge the financial support by UC Riverside and National Science Foundation Career award to BPTF (no. DMR-1654780).

I would like to take the opportunity here and thank all the people who supported me for the last several years supporting and standing next to me in my PhD at University of California, Riverside.

First, I want to thank and show my deep gratitude to my supervisor, Professor Boniface Fokwa. Without his trust, support, patience, and kindness this path may have not been completed. He always inspired me with his ideas, scientific talks, mentality, and longtime discussions. All these

helped me to step wisely in the solid-state chemistry and materials science path building up future. Besides research, I learnt a lot of life lessons from him which I may never forget. THANK YOU, Boniface.

I would like to thank Professor Suveen Mathaudhu for his support and nonstop help in my PhD. I have known Suveen from the very first quarter of my PhD and ever since he has been supportive, available, and helpful. Thank you Suveen for all these years, I learnt a lot from you, and I wish you great years ahead at Colorado Schools of Mines.

I want to acknowledge my internal committee members and collaborators, Professor Suveen Mathaudhu, Professor Pingyun Feng, for their time, comments and suggestions for my work and going through my dissertation carefully. Also, my special thanks to my collaborator Professor Juchen Guo, his great team and Professor David Kisailus who I was his TA for two quarters.

I have to also thank Professor Reza Abbaschian, for giving me the opportunity to join UCR and the Materials Science Program. I learnt a lot from him in the field of metallurgy.

I am grateful to have wonderful lab mates and friends at UC Riverside. I want to thank my current and former lab mates at Fokwa Lab, Dr. Jan Scheifers, Dr. Abishek Iyer, Dr. Teresa Ortner, Dr. Yuemei Zhang, Dr. Palani Raja, Eunsoo Lee, Diana Luong, Johan Yapo and everyone else for providing a great, friendly and scientific environment for the past years. They have always been available and ready to discuss science, improving my work. My lab had the friendliest environment I could ever ask for, and I miss all you guys.

I want to especially thank Eunsoo, Diana and Jan for being my first co-authors and co-authors. Without their contribution, help, knowledge, and day long discussions, some of the work in this thesis may have not been completed. You guys are great scientists.

I am happy to have had great undergraduate students including Ashwin Bhupathy, Aly Rafaat, and Avery Hill working with me. They have all been hardworking and passionate in their work. I wish them a great future.

Finally, and most importantly, I would like to thank my parents, Hamid and Shiva, my younger brother Aryan for their non-stop support, deep love, and inspiration. I was not definitely able to make it this far without them. I miss them from the deepest part of my heart and wish they were here for my graduation. I should also deeply thank my relatives Shohre, Shabnam, Katy and Farkhonde which have been just like my family for the last five years. From the very first day I moved to US, they have helped and supported me on every occasion. I wish we can all get together soon with no boundaries.

Ardalan Rezaie
Riverside
2015 - 2021

Dedicated to the students all around the world who are apart from their families

ABSTRACT OF THE DISSERTATION

Synthesis and Characterization of Ternary Layered Transition Metal Borides and Chalcogenides for Energy Applications

by

Amir Ardalan Rezaie

Doctor of Philosophy, Graduate Program in Materials Science & Engineering
University of California, Riverside, September 2021
Dr. Boniface Fokwa, Chairperson

Layered materials have been studied for several decades but only after the discovery of graphene, the vast potential of these materials have been widely explored. These materials such as graphite, hexagonal boron nitride, van der Waals chalcogenides, MAX / MAB phases etc. have been investigated for their anisotropic properties and potentials to be tailored in to nano and two-dimensional structures. The research presented in this dissertation, focuses on the synthesis and characterization of two of these layered compounds, investigates their possible exfoliation toward 2D and nano sheets and finally introduces them as potential materials for energy applications such as Li-ion batteries and hydrogen evolution. In the first part of this dissertation, $Ni_{(n+1)}ZnB_n$ (n=1, 2) nano laminated MAB phases, were synthesized through a two-step melt solidification technique leading to the formation of pure, preferred oriented bulk MAB sheets. Studying these MAB phases for possible chemical exfoliation, led to the formation of high surface area MAB particles which led to the discovery of the first MAB phases as active Li-ion battery anodes.

Subsequently, different electrodes of the synthesized $Ni_{(n+1)}ZnB_n$ Phases were studied for their hydrogen evolution properties. It was observed that forming densified pellet of $Ni_{(n+1)}ZnB_n$ phases provide the lowest overpotential among all the other reported MAB phases. Studying the exposed

surface of the disk electrodes through microscopy and spectroscopy techniques suggested the potential basal plane activity of the synthesized MAB phases which our DFT calculations supported. While studying the synthesized layered $Ni_{(n+1)}ZnB_n$ phases, it was observed that they tend to delaminate and break along their basal plane hinting the possibility of forming quasi-2D sheets through more severe forces such as liquid phase exfoliation.

Finally, we studied the layered vdW Fe_3GeTe_2 (FGT) compound for its hydrogen evolution reaction (HER) activity. Liquid phase exfoliation followed by densification led to the discovery of active basal plane and edge sites in FGT, suggesting it as an active bulk hexagonal layered vdW compound, thus paving the way for future studies of iron based layered materials for HER. This dissertation contributes to the layered materials field, demonstrating the high potential of these materials for energy applications.

Contents

List of Tables

List of Figures

Chapter 1

Introduction

1.1 An Overview on Layered Materials:

Van der Waals (vdW) layered materials have been studied for the last 50 years.[1] These layered materials were defined as solids containing strong in plane and weaker out plane bonds.[2] The graphene discovery and its outstanding properties led to a huge attention on layered materials in the scientific community.[3, 4] The idea of peeling of one atomic layer of a 3D parent (bulk) layered material led to the formation of 2D materials such as h-BN [5], transition metal dichalcogenides (TMDs) [6] and other inorganic nano materials through chemical or mechanical exfoliation of their parents.

For the last two decades, MAX phases ($M_{n+1}AX_n$), layered hexagonal transition metal carbides (X = C) and nitrides (X = N) have seen widespread interest due to their advantageous thermal, electrical, and elastic properties if compared to their binary metal carbide and nitride counterpart. Recently, the discovery of a new family of 2D carbides or nitrides called MXenes have brought MAX phases into extra attention. These 2D layers are directly exfoliated from their corresponding layered MAX phases after selectively etching the “A” interlayer atoms using different etching mechanisms.[7] Very recently, a new MAX-related family of layered materials called MAB phases - MAX phases with X = boron, have become widely studied due to their unique bonding characteristics and mechanical properties.[8, 9] These novel ternary layered borides have shown a great potential to form the first 2D metal boride. Detailed description of these layered structures and their properties are described in this chapter.

1.2 MAX Phases

MAX phases are a large group of ternary layered materials holding a composition of $M_{n+1}AX_n$, in which M, A and X represent an early transition metal, an element mostly from group 13-16 and carbon and/or nitrogen, respectively. The MAX phases show a unit cell consisting of MX_6 octahedra sandwiched between layers of "A" element. These metal-ceramic materials crystallize in the hexagonal space group of $P6_3/mmc$.[10] MAX phases were first discovered in the 1960's by Nowotny et al.[11, 12] However it was not until the 1990's, that Barsoum et al. re-studied their properties more broadly [10] and introduced them as excellent materials with properties such as machinability, high corrosion resistance, high ductility, excellent electrical and thermal conductivity, thermal shock resistance etc.[13-15] **Figure 1** shows the crystal structures for different MAX phases with compositions 211, 312 and 413. As seen in this figure, all the MAX phases contain one layer of Al (or a group 13-15 elements in general) as an interlayer, however the thickness of the MX-slabs changes with "*n"*, which defines the composition and M/X ratio.

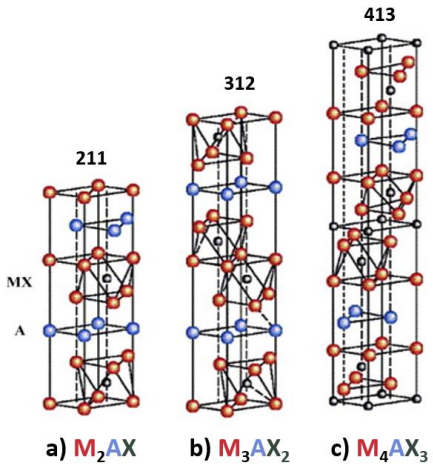

Figure 1. Crystal structures of a) 211 b) 312 c) 413 related MAX phases – reproduced from [16] – adapted from [15]

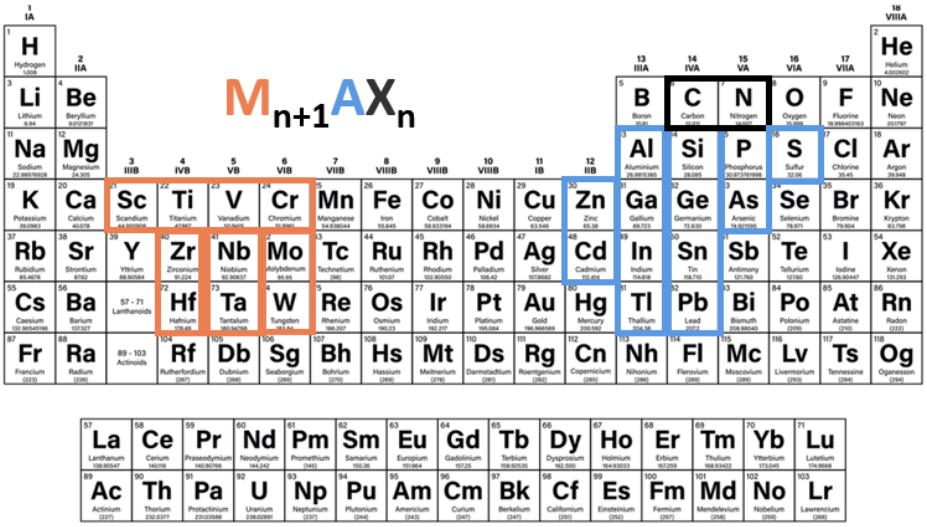

Figure 2. Summary of known MAX phases - updated from the MAX phases book [17]

Due to the high melting point of the starting materials, the layered MAX carbides have been mainly synthesized through solid state synthesis or thin film growth methods such as [18]: hot isostatic pressing [10, 19], powder alloying [20], spark plasma sintering (SPS) [21], CVD [22, 23] etc. So far more than 60 MAX phases have been synthesized and studied. The possibility of forming different solid solutions in the M, X, or A site, has broadened MAX phases properties and compositions [24] and made them interesting for various applications. MAX phases metallic conductivity, layered morphology and mechanical strength combined with the existence of Si or Sn as the "A" element have made them interesting for Li-ion battery applications.[25, 26]

1.3 MXenes

The existence of a strong M-X bonds and a weaker M-A bond in MAX phases has led to formation of novel 2D materials named MXenes. MXenes are new type of 2D materials composed of transitional metal carbide and nitrides holding a chemical composition of $M_{n+1}X_n$ (n=1-4) where M is a transition metal and X is either carbon or nitrogen.[7, 27, 28] These 2D materials are synthesized via selectively etching of the weakly bonded "A" atoms by using strong etchants such

as HF (HCl / LiF) and subsequently exfoliating the detached layers via sonication or with deintercalation of large organic molecules. In this process, the exposed "M" atoms get terminated with F/OH or O atoms which weakens the interaction between the layers. Several MXene layers have been synthesized up to now including 3, 5 and 7 atomic layers and experiments show that the MXene layers are stabilized when "*n*" has higher values.[28-30]

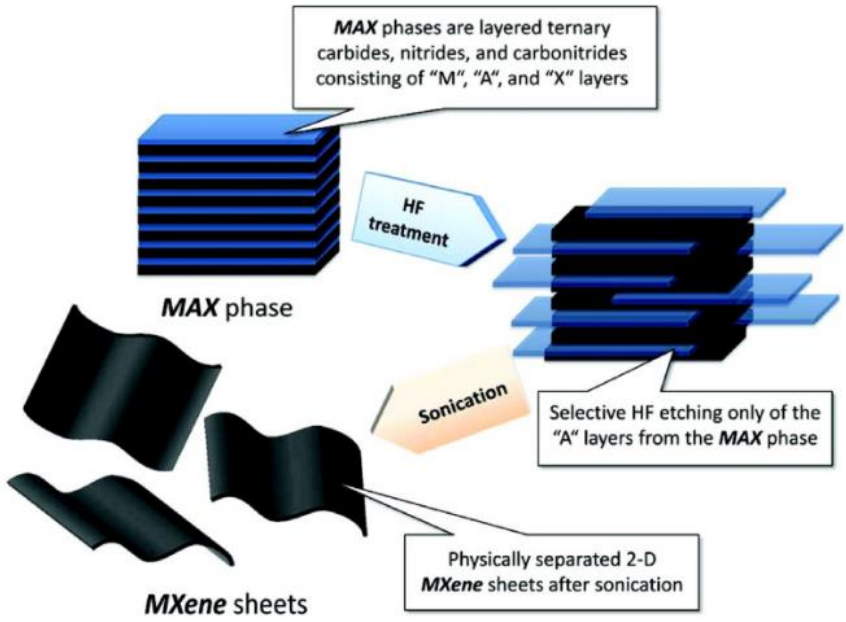

Figure 3. Schematic of exfoliation process of MAX phases leading to MXenes novel 2D carbides – reproduced from [31]

Due to the metallic nature and high surface area of the exfoliated MXenes, they have been widely used as electrodes in Li-ion and beyond Li-ion batteries . After the first MXene discovery, Gogotsi et al. investigated Ti_2CT_X MXene for its specific capacities in LIBs.[32] Later on, other MXenes, such as V_2CT_x and Nb_2CT_x were demonstrated as promising materials for Li-ion batteries.[33] Studies have shown that both the composition (transition metal element and the composition) and

the surface area (multi-layered compared to delaminated) affect the MXene electrode performance. Further MXenes investigations also demonstrated that, introducing additives such as carbon nano tubes (CNT), carbon fibers etc. may increase the interlayer distancing between the MXenes, improving the ion-accessibility and boosting the performance and specific capacity of MXene electrodes.[30, 34, 35]

Besides battery applications, MAX phases and MXenes have been reported as promising materials for other energy related applications such as hydrogen evolution reaction (HER).[36] MXenes have shown a drastic increase in their electrocatalytic activity upon becoming two-dimensional compared to their MAX form. The synthesis, properties, and wide variety of applications of MXenes, have made MAX related phases such as ternary MAB layered borides, highly attractive.

1.4 MAB Phases – Layered Ternary Borides

Transition metal borides mainly show high hardness and low compressibility due to the strong covalent bonding nature between the boron and metal atoms.[8, 37] Contrary to metal carbides, the crystal structures of borides are based on trigonal prisms BM_6 leading to a high anisotropy in their structures.[38, 39] Kiessling et al. had previously classified the boride structures based on their metal/boron (M:B) ratio.[39] Phases with high M:B ratio show a structure with isolated boron while decreasing the ratio leads to the formation of B-B linkages. For example, Cr_5B_3 (M:B = 1.6) and FeB (M:B = 1) show B-B dumbbells and zigzag chains in their respective structures.[40, 41] In a structure with a M:B ratio below one, 2D boron layers (graphene like) or 3D boron frameworks occur in the crystal structures.[42] Understanding the M:B ratio may help in discovering new boride structures and tune their physical properties. Due to their unique structure and physical properties, borides have been used in wide variety of applications. $Nd_2Fe_{14}B$ and MgB_2 have been known for their permanent magnetic and superconductive properties, respectively.[43, 44] Recently some

binary borides have been investigated for their HER properties for clean energy application.[45] However, many properties of borides are still under investigation.

A new family of layered ternary borides called MAB phases has become much of an interest due to its physical and mechanical properties.[8] These MAB phases, while they are chemically and structurally different than MAX phases, have similar properties to MAX phases such as high conductivity [46], stiffness [46] and resistant to thermal shock.[47, 48] In contrast to MAX phases and MXenes, MAB phases have not been studied much yet.

The very first ternary MAB phase, MoAlB, was first synthesized in the 1940s. The crystal structure was solved with a *Pmmm* orthorhombic space group.[49] Later, in the 1960s the crystal structure was correctly resolved with a *Cmcm* orthorhombic structure.[50] Next, WAlB was synthesized and characterized with a similar structure to MoAlB.[51] Meanwhile till 2015 other ternary layered borides such as Mn_2AlB_2 and Cr_2AlB_2 were synthesized and characterized as ternary layered borides.[52, 53] However, it was in 2015 that Ade et al. introduced the term "MAB phase" for the first time by the discovery of Cr_4AlB_6.[8] This phase, next to Cr_2AlB_2 and Cr_3AlB_4 made a $(CrB)_2Al(CrB_2)_y$ ternary series which is similar to the MAX phase series. However, their composition does not follow the exact $M_{n+1}AX_n$ type. Since the rediscovery of MAB phases as ternary atomically laminated borides, different types of this new family have been studied. MAB phases include compounds with different compositions and structures such as Cr_2AlB_2 (212 type - *Cmmm*) [8], MAlB (*Cmcm*) [9], Cr_3AlB_4 (314 type -*Pmmm*) [8] , Cr_4AlB_6 (416 type -*Cmmm*) [8], Ru_2ZnB_2 (*I*4$_1$*/amd*) [54], Y_2SiB_8 (*P*4*/mbm*) [55], Cr_5SiB_3 [47], i-MAB phases [56] Ni_2ZnB [57] and Ni_3ZnB_2 (*C*2*/m*).[57-60] The variety of MAB structures differentiate them from the MAX phases which are mainly hexagonal (space group *P6$_3$/mmc).* This significant structural difference is directly related to the boron substructure which varies from dumbbells, to zigzag B_4 fragment, to zigzag boron chain, to chain of boron hexagons and chain of boron double hexagons.[8] In MAX

phases, however, no bond exists between X (C, N) atoms. The specific crystal structures of some of the known MAB phases are shown in **Figure 4.** However, recently a group of ternary layered borides – MAX phase borides – which hold crystal structures similar to MAX phase have been identified.[61, 62]

Table 1 reports the experimentally synthesized and reported ternary layered borides including MAB phases and MAX phase borides. All the reported MAB phases have been synthesized through a high-temperature technique mainly including flux-method and solid-state synthesis.

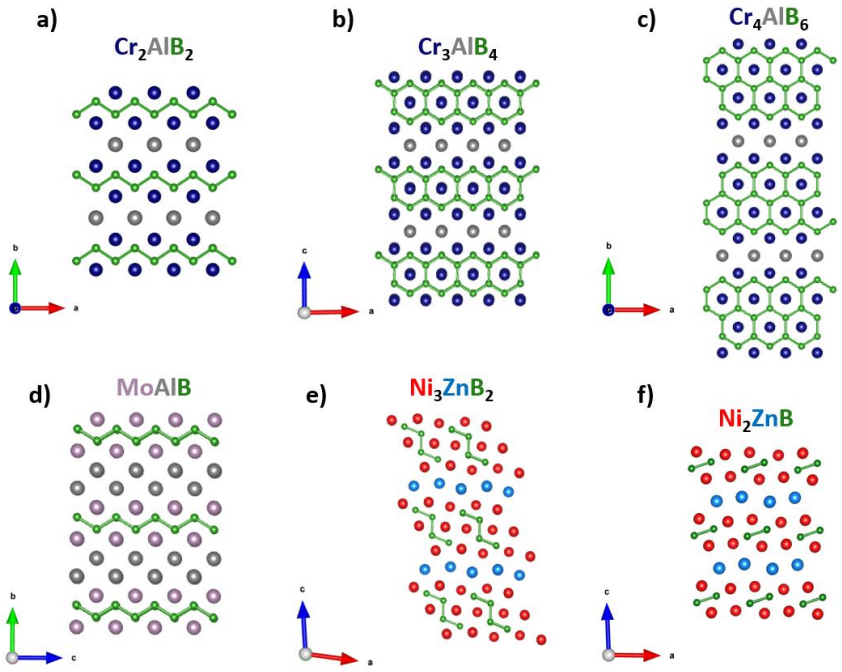

Figure 4. Crystal structures of different MAB phases a) 212 type b) 314 type c) 416 type d) MoAlB structure e, f) $Ni_{(n+1)}ZnB_n$ (n = 2, 1)

Table 1. Reported MAB phases, their space groups and synthesis conditions

MAB Phase	Synthesis	Crystal structure	Space Group	Reference
Cr_2AlB_2	Solid-State, Al Flux	Orthorhombic	*Cmmm*	[8, 63]
Cr_3AlB_4	Solid-State, Al Flux	Orthorhombic	*Pmmm*	[8, 64]
Cr_4AlB_6	Al Flux	Orthorhombic	*Cmmm*	[8]
Cr_4AlB_4	Solid-State	Orthorhombic	*Immm*	[65]
WAlB	Al Flux	Orthorhombic	*Cmcm*	[8]
MoAlB	Powder/Excess Al, Al Flux, Hot-Pressing	Orthorhombic	*Cmcm*	[8, 9, 66]
Mn_2AlB_2	Powder/Excess Al, Hot-Pressing	Orthorhombic	*Cmmm*	[8, 67]
Fe_2AlB_2	Arc melting, Solid-State	Orthorhombic	*Cmmm*	[8, 68, 69]
$Ni_{(n+1)}ZnB_n$	Solid-State / Solidification Technique	Monoclinic	*C*2/*m*	[57, 60, 70]
Ru_2ZnB_2	-	Tetragonal	*I*41/*amd*	[71]
Zr_2SB	Solid-State / Induction Melting	Hexagonal	$P6_3/mmc$	[62]
Hf_2SB	Solid-State / Induction Melting	Hexagonal	$P6_3/mmc$	[62]
$Mo_{1.33}Y_{0.66}AlB_2$	Solid-State	Hexagonal	$R\bar{3}m$	[56]
$Mo_{1.33}Sc_{0.66}AlB_2$	Solid-State	Hexagonal	$R\bar{3}m$	[56]
Ti_2InB_2	Solid-State	Hexagonal	$P6_3/mmc$	[72]

Analogous to MXenes (2D materials) derived from MAX phases, MAB phases have been recently studied for their potential of forming novel 2D borides. In contrast to MAX phases and MXenes, the chemical exfoliation of MAB phases and MBenes synthesis is still in its infancy and only partially etched samples have been reported to date. Cr_2AlB_2 was the first MAB phase investigated toward potential CrB 2D layers. However, no CrB 2D MBenes were observed.[63, 73] In another study, Schaak *et al*. investigated Al deintercalation in MoAlB MAB phase. However, Al was not fully etched out leading to the formation of Mo_2AlB_2 phase containing less aluminum.[66, 74, 75] In another study, Ti_2InB_2 MAB phase was de-alloyed leading to formation of the TiB bulk structure.[72] In general, previous works suggest that exfoliating MAB phases is more challenging than exfoliation of MAX phases. This significant change might be related to the structural

difference of MAB and MAX phases. The boron substructure in the MAB phases, varies all the way from dumbbell to chain of boron hexagons. However, in MAX phases, no bond exists between the X (C, N) atoms. Additionally, the interaction of boron and the "A" element is more significant than the "X" and "A" element in MAX phases.

Although no MBene has been synthesized in bulk form, theoretical studies have shown the capability of these materials for magnetism [76], electrocatalysis [77] and battery applications.[78] Given the potential of these 2D borides, the exploration of these materials is high of interest.

Herein, we focus on two selected MAB phases, $Ni_{(n+1)}ZnB$ (n = 1, 2) by investigating their zinc deintercalation, their Li-ion battery performance and their hydrogen evolution catalytic activity for the first time. This dissertation consists of relevant manuscripts which are or will be published in peer reviewed journals. Chapter 2 consists of information on the experimental procedures, a brief introduction on the utilized instruments and characterization techniques. The other chapters contain detailed information of the procedure and methods, results, discussion, and suggested future works. Chapter 3 focuses on the synthesis, characterization, etching and Li-ion electrode properties of the MAB phases. In chapter 4, the hydrogen evolution properties of different type of MAB electrodes are discussed. Chapter 5 studies the possible exfoliation of Ni_3ZnB_2 MAB phase through various ultra-sonication techniques. Chapter 6 discusses the discovery of active sites and the high performance of Fe_3GeTe_2 (FGT) vdW layered material toward the hydrogen evolution. And finally, in chapter 7, a short summary and concluding points of this work are presented.

Chapter 2

Materials, Methods and Experimental Procedures

In this chapter, details of starting materials, synthesis routes, characterization techniques processing and property measurements of the proposed layered compounds are provided.

2.1 Synthesis and Processing Methods

2.1.1 Arc Melting

An arc melting furnace is made of an encapsulated jar, a water-cooled copper crucible and heart, an adjustable electrode (mainly tungsten) and a direct current (DC) power supply which provides current in the system. Herein, the sample is put in the crucible and the whole system is vacuumed providing a clean environment inside the jar. The current goes all the way through the copper heart to the electrode and the tungsten tip. In the next step, an arc (ionized species in the jar) is formed by the existence of high current completing the circuit by going through the sample all the way back to the DC power supply. In this work, the arc melting system used for synthesizing the preferred intermetallics and master alloys is shown in **Figure 5**. The chamber is vacuumed, and argon purged several times before melting to prevent oxidation.

Arc melting furnace was utilized to make Ni-B master alloys. A properly mixed nickel (Arcos Organic 99.9%) and boron (Alfa aesar-98%) powder were cold-pressed into a pellet and arc-melted in an inert atmosphere. Different samples were synthesized as a master alloy weighing from ~ 1-3 g. The arc-melting chamber was washed with argon gas 3-5 times before starting the synthesis. The synthesized master alloy button was flipped after the first melting (23 A) and re-melted (29A) to provide a better homogenous sample.

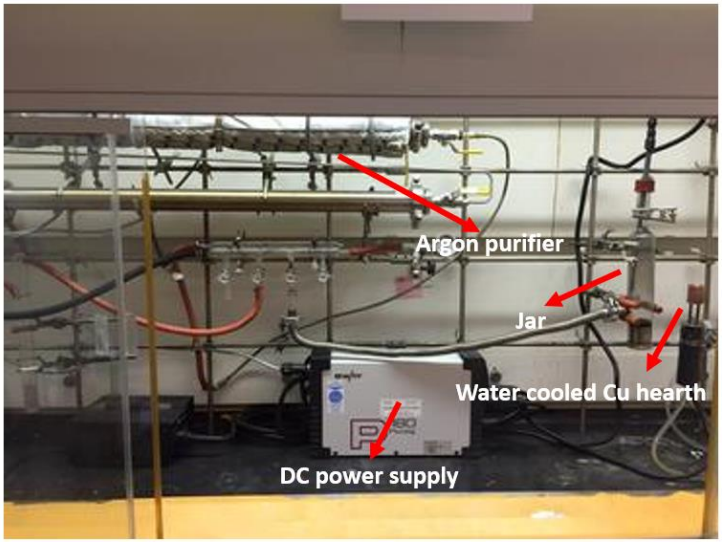

Figure 5. Arc melting furnace used in this work

2.1.2 Quartz Sealing Tube / Tube Furnace

The synthesized master alloy was crushed and mixed with proper amounts of zinc and nickel powder, pressed into a pellet, and heated in a tube resistance furnace to synthesize the final product. In order to provide an oxygen free environment, the pellets (250mg) were vacuumed and sealed in a quartz tube. The quartz ampules were vacuumed and purged with argon 3-5 times and then sealed in a vacuum atmosphere. The ampules were put in a vertical tube furnace (MTI – GSL 1100X – **Figure 6**). The samples were first pre-alloyed at 700 then re-crushed, remixed pressed and heated again in a tube furnace. The synthesis conditions and temperature time diagram for each cycle for the samples are discussed in the synthesis section.

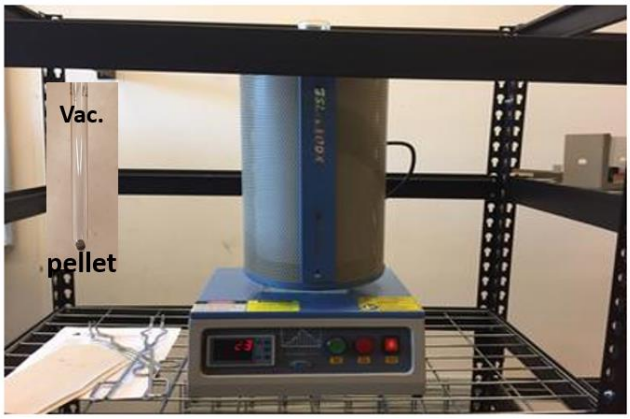

Figure 6. Vertical tube furnace used in this work – inset shows a sealed tube holding the pellet

2.1.3 Etching Procedure

The synthesized MAB phases were powdered with a mortar and pestle and stirred / ultra-sonicated in diluted 1M HCl in an 8 mL vial. During the etching process, hydrogen bubbles were evolved proving the etching step. The etching was done for 72h. Every few hours the solution was ultrasonicated for 5-10 mins to disperse the particles more in the solution and provide a better homogeneity. This resulted in three different particles: 1) the larger particles precipitating in the solution 2) high aspect ratio particles floating on the top 3) nano sheets/particles dispersed in the solution. Since no significant zinc deintercalation was observed for the studied MAB phases, in this thesis we mainly focus on the larger precipitated particles and the bulk MAB phases for further studies. The amount of the other parts was not enough to provide a mass amount for further studies.

2.1.4 Ultra-Sonication

The synthesized layered materials (MAB phases and FGT) were crushed, powdered and ultrasonicated in ethanol and water to exfoliate and break the particles towards nano size. All the sonication was done in a SHARPERTEK XP-PRO 40000 Hz bath sonication system. The MAB

particles were sonicated in water and ethanol in an ice/water bath to avoid any ethanol evaporation or addition heating. The FGT was sonicated only in ethanol in the same environment.

2.2 Characterization techniques

2.2.1 Powder X-ray Diffraction (XRD)

X-ray diffraction (XRD) analysis was performed using a Rigaku MiniFlex 600 diffractometer (**Figure 7**), using a Cu Kα radiation source (λ=1.5418 Å) to confirm the synthesis, understand the crystallinity, particle size and orientation of the synthesized phases. Phase analysis was continued with a Rietveld refinement technique using the FULLPROF program.[79] Based on the accuracy of the data required, and particle sizes, different step sizes and step times were used for the measurements.

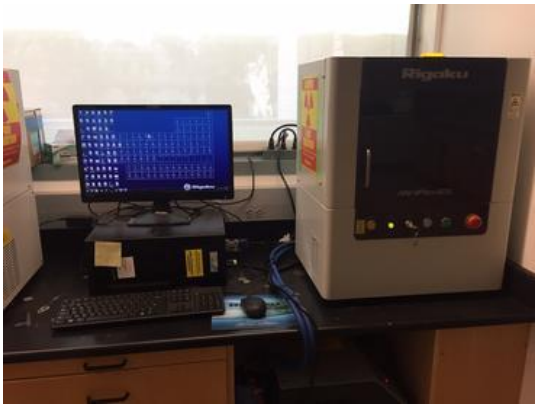

Figure 7. Rigaku MiniFlex 600 powder X-ray diffractometer

2.2.2 Electron Microscopy (SEM / TEM)

The synthesized phases were investigated under electron microscopy to study their morphology, microstructure, and crystal structure. Secondary electron images, backscatter imaging and energy-dispersive X-ray spectroscopy (EDS) were obtained with NovaNanoSEM 450 electron microscope

equipped with a 50 mm^2 X-Max50 SD EDX. The TEM imaging were obtained using a copper holey carbon grid under a ThermoFisher Scientific (formerly FEI/Philips) Titan Themis 300 instrument. After washing the solution precisely and sonicating it for few minutes, the layers were scooped from the liquid via the grids for further investigation. Both instruments are located at the center facility for advanced microscopy and microanalysis (CFAMM) of the University of California, Riverside.

2.2.3 Metallography / Optical Microscopy Analysis

A Nikon eclipse LV 100 D-U instrument was used in this study. The cast samples were cut in half, mounted in epoxy / resin, abraded with SiC sandpapers (up to 1200 grit) and polished with alumina powder. The polished cross section was investigated under an optical microscope to understand the tilt and phase distribution. The polished samples were investigated under SEM for any impurities.

2.2.4 Inductively Coupled Plasma (ICP-OES)

Inductively coupled plasma (ICP) is an analytical method to detect metals in a solution. ICP-OES was done on the synthesized MAB phases and in different stages to have a more precise understanding of the composition of the MAB particles. The particles were dissolved in an aqua regia solution and ICP measurement was done on the solution to trace nickel and zinc ratio. For the electrochemical measurements, the ICP-OES was done on the KOH solution diluted with HNO_3 and water. All the measurements were done in the Environmental Science Research Laboratory utilizing a Perkin-Elmer Optima 7300DV apparatus by the operator.

2.2.5 X-ray photoelectronic Spectroscopy (XPS)

X-ray photoelectron spectroscopy (XPS) data was collected on a Kratos AXIS Supra (Al Kα=1486.7 eV) instrument and at UC Irvine Materials Research Institute (IMRI) and the Kratos

AXIS ULTRADLD XPS system at UC Riverside. The synthesized MAB phases, their etched derivatives and the disassembled coin cells after electrochemical measurements were prepared for XPS analysis. The electrodes were washed by dimethyl carbonate and then dried under vacuum at 60°C inside a glovebox. After that, the prepared samples were stored in a stainless-steel tube with KF flange sealing. Then the samples were transferred to a glove box integrated to the Kratos AXIS Supra instrument for further XPS analysis.

2.3 Electrochemical Analysis

Battery electrochemical analyses were performed with two-electrode 2032-type coin cells. In the half cells to test the MAB phase materials and their derivatives (composites and etched particles), the working electrode was composed of 80 wt.% of the tested material, 10 wt.% of polyvinylidene difluoride (PVDF) as binder, and 10 wt.% of acetylene black and cast on copper foil. The typical areal loading was ~ 2 mg cm^{-2}. The electrolyte was composed of Lithium hexafluorophosphate ($LiPF_6$) solution (1 M) in a mixture of ethylene carbonate (EC) and diethyl carbonate (DEC) (volume ratio EC: DEC= 50:50). Commercial lithium foil (750 μm thickness) is used as the counter electrode. Galvanostatic cycling was performed between 0.01 and 3.0 V vs Li/Li^+ in half cells. The current densities for electrodes were 20, 100 and 300 mA g^{-1}. Cyclic voltammetry was performed using scan rates of 0.1 mV s^{-1} between 0.01 and 3.0 V vs Li/Li^+. All battery analysis and measurements were carried out by Prof. Guo group, at UC Riverside.

2.5 Hydrogen Evolution Reaction (HER) Catalytic Activity

Different MAB and FGT electrodes and were investigated for their possible HER activity. Below the electrode preparation, and the measurement conditions are elaborated. All the HER measurements were done by my lab mate, Eunsoo Lee at Fokwa Lab.

2.5.1 Electrode Preparation

One milligram of sample was sonicated in 95 µl IPA and 5 µl Nafion solution. Then, the 30 µl of solution was dropwise on a carbon cloth (0.3×0.3 cm^2). The carbon cloth was dried for 5 h at 50 °C in an oven (the catalyst loading: ~3 mg/cm^2). The dried carbon cloth was attached on copper sheet using conductive silver paste. The exposed surface of copper sheet was covered with epoxy adhesive and dried overnight at room temperature. Pt/C (20 %) electrode was prepared in the same method.

The pressed pellet electrodes were formed through pressing 100-130 mg of the bulk MABs via a hydraulic press. The FGT pressed electrodes were formed via pressing the layers through a spark plasma sintering (SPS) system at Mathaudhu group. All the densified disks were mounted in epoxy, polished, and attached to a copper sheet with silver adhesive.

2.5.2 Electrochemical Characterization

The electrochemical tests of the samples were carried out on a VSP electrochemical workstation (Bio-Logic Science Instruments, France) using a three-electrode system: prepared electrode of our sample as a working electrode, graphite rod and saturated calomel electrode (SCE) as the counter and reference electrodes, respectively, in 1 M KOH electrolyte solution (pH=14.2). All the potentials are translated into the reversible hydrogen electrode (RHE) according to the equation: $E_{RHE} = E_{SCE} + 0.242\ V + 0.059 \times pH$. All the measurements were obtained by *iR*-drop compensation. Linear sweep voltammetry (LSV) plots were used to measure electrochemical HER activity with a scan rate of 5 mV/s in the potential range of -2.0 to -1.0 V vs. SCE. It was recorded after 10 cycles of cyclic voltammetry (CV) tests in the potential range of -2.0 to -1.0 V to stabilize the current.

The Tafel equation $\eta = b\,log\,j + a$ (where j is the current density, b is the Tafel slope, and a is the intercept relative to the exchange current density j_o) was used to calculate the Tafel slopes by fitting the linear part of the Tafel plots.

Electrochemical impedance spectroscopy (EIS) was conducted at -0.22 V vs. RHE by applying an AC voltage over the frequency range from 100 kHz to 1 mHz with an amplitude of 10 mV versus the open-circuit potential.

The electrochemically active surface area was estimated CV tests using different scan rates within a non-faradic reaction region. The double-layer capacitance was calculated by plotting the □J (J_a-J_c) against the scan rate.

Chapter 3

Synthesis and Li-ion Electrode Properties of Layered $Ni_{(n+1)}ZnB_n$ (n =1, 2) MAB Phases

In this chapter we go through the synthesis and characterization of two MAB phases with the general formula of $Ni_{(n+1)}ZnB_n$ (n=1, 2). Subsequently, we investigate the effect of etching on their microstructure. Finally, we investigate and report the Li-ion electrode properties of the etched and unetched MAB phases for the first time. This chapter is adapted from the published manuscript:

DOI: *10.1039/C9TA12937E* - **Rezaie AA**, Yan Z, Scheifers JP, Zhang J, Guo J, Fokwa BP. Journal of Materials Chemistry A. 2020;8(4):1646-51.

3.1 Introduction

Since the discovery of MAX phases, these layered transition metal carbides and nitrides with general formula $M_{n+1}AX_n$ (n = 1-3) have gained interest in the field due to their mixed metallic and ceramic properties.[10-12] In 2011 Gogotsi et al.[7] introduced MXenes (M = early transition metal, X = C or N), which are derived from the MAX phases by chemical exfoliation of the A layer, as promising candidates for lithium-ion battery anodes.[30, 32] Currently MXenes have been considered for other applications such as batteries [30, 32], supercapacitors [30, 80], and for magnetic shielding [81] etc. In 2015, Hillebrecht et al. [8] introduced a MAX-related family of layered materials called MAB phases - MAX phases with X = boron. Even though these MAB phases are chemically and structurally different from the MAX phases, they have similar properties such as high conductivity [46], stiffness [46] and resistant to thermal shock.[47] MAB phases include compounds with different compositions and structures such as M_2AlB_2 (*Cmmm*) [8], MAlB (*Cmcm*) [9], Cr_3AlB_4 (*Immm*) [8], Cr_4AlB_6 [8], Ru_2ZnB_2 ($I4_1/amd$) [54], Y_2SiB_8 ($P4/mbm$) [55], Cr_5SiB_3 [47] and Ni_3ZnB_2 ($C2/m$).[57-60] These MAB phases mainly have different crystal structures

than the MAX phases which are mainly hexagonal (space group *$P6_3/mmc$)*. This significant structural difference is directed by the boron substructure which varies from dumbbells, to zigzag B_4 fragment, to zigzag boron chain, to chain of boron hexagons and chain of boron double hexagons.[8] In MAX phases, however, no bond exists between X (C, N) atoms. In addition, significant bonding interactions exist between boron and the A atoms in MAB structures, while no significant interaction exist between X and A in MAX structures. These significant A-B interactions are likely the main reason why A is rather difficult to be etched out of the MAB structures to produce MBenes [63, 66, 74], while the absence of A-X interactions in MAX phases supports the easy exfoliation of the "A" element.[82] This analysis shows that exfoliating $Ni_{n+1}ZnB_n$ phases will be as difficult as the other MAB phases. Although no MBene has been realized quantitatively yet, theory has suggested that these materials have great potential in battery and electrocatalysis applications.[78] Even though several binary transition metal borides such as VB_2 and TiB_2 have been investigated as anodes for non-rechargeable battery systems, [83, 84] the electrochemical properties of MAB phases for rechargeable battery electrodes has not been experimentally investigated, to best of our knowledge.

The structural diversity of MAB phases give them a unique and untapped advantage: Many of them contain M transition elements (spanning the whole 3d spectrum) [8] that are important for Li-ion battery performance: Ti, V, Cr, Fe, Mn and Ni.[85, 86] In this study, we will focus on Ni_2ZnB and Ni_3ZnB_2, which are evaluated for the first time for their Li-ion electrode properties as a proof of concept. We show that the bulk samples are largely inactive as battery materials, however, exposing Ni_2ZnB and Ni_3ZnB_2 to an acid treatment leads to two unexpected morphological behaviors that drastically increase their Li-ion battery performance.

3.2 Results and Discussion

The Ni-Zn-B system was previously investigated at 800°C by Malik *et al.* showing the existence of different phases such as $Ni_{12}ZnB_8$ (space group: *Cmca*), $Ni_{21}Zn_2B_{20}$ (space group: *Cmca)*, Ni_3ZnB_2 (space group: *C2/m)*, Ni_2ZnB (space group: *C2/m)*, and Ni_3Zn_2B (space group: *C2/m)*[57-60, 87]. Out of all these phases, only Ni_2ZnB and Ni_3ZnB_2 have layered structures [57, 58] with a general chemical composition ($Ni_{n+1}ZnB_n$) like the MAX phases ($M_{n+1}AX_n$). In these two layered MAB structures, beside the expected Ni-Zn and Ni-B bonding interactions, Zn and B atoms also significantly interact leading to wave-like arrangement of the zinc layer in both structures (**Figure 9)**.

The synthesis of phases in the Ni-Zn-B system is quite challenging: As the Ni-Zn-B isotherm at 800°C [57] suggests (**Figure 8**) Ni_2ZnB and Ni_3ZnB_2 are stable at this temperature. However, due to their small phase areas in the isotherm, a small shift in the composition will lead to the formation of impurities based on the scalene triangles representing a three-phase equilibrium. For example, in their recent discovery of Ni_2ZnB Rogl et al. obtained a multiphase product (Ni_2ZnB, Ni_3Zn_2B, Ni_2Zn_{11}).[57] The same authors previously synthesized single-phase Ni_3ZnB_2 by mixing NiB_x master alloy with fine Zn filings in proper compositional ratio. The mixture was then submitted to several preparation steps (milled/cold-pressed/heat-treated/annealed/quenched/re-milled/hot-pressed) that enabled the synthesis of a polycrystalline sample with isotropic particles (no preferred orientation observed).[60]

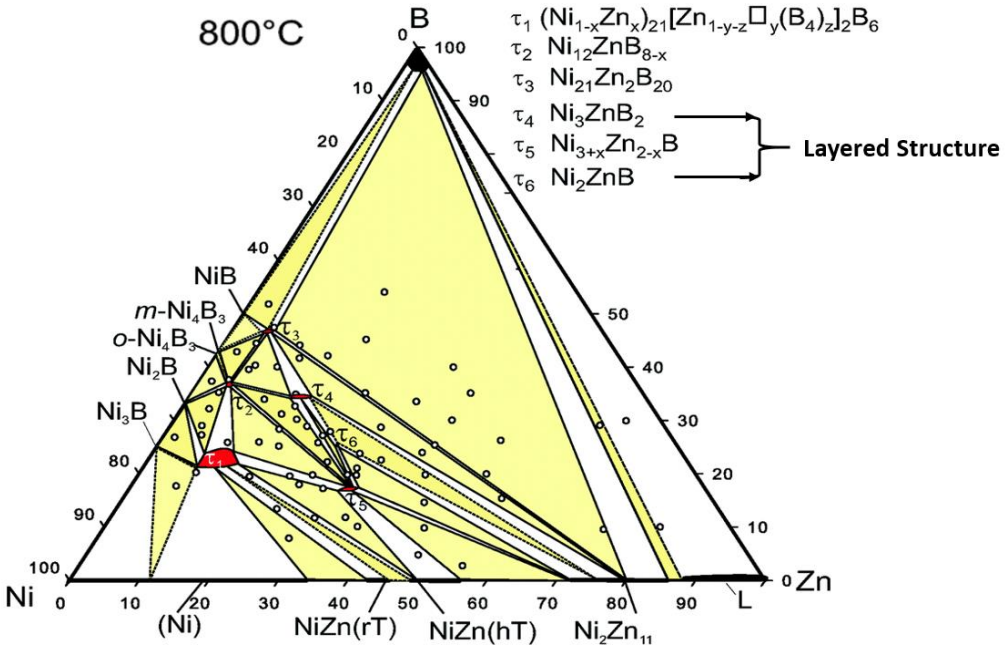

Figure 8. Ni-Zn-B ternary isotherm at 800 C - reproduced and adapted from [57]

We have developed a new approach in our synthesis, by first preparing a high quality Ni_2B master alloy through arc-melting as it melts congruently (**Figure 10**). Since Ni melts at 1455 °C, boron melts at 2095 °C and zinc has a melting point of 420 °C, the synthesis of Ni-Zn-B MAB phases, Ni_2ZnB and Ni_3ZnB_2, is challenging. Moreover, zinc boils at 907 °C which means that going through regular solidification synthesis, will lead to evaporation of zinc before melting the other elements. Using excess zinc, also known as the metal flux method, is also not the proper method to synthesize these MAB phases since Zn is involved in the reaction and the possibility of side reactions is very high. Thus, it is important to provide the Ni and B source in a procedure matching Zn melting and boiling temperature. Ni_2B was then powdered and mixed with the remaining elements according to the targeted composition, pressed to a pellet and submitted to a melting-solidification technique including pre-alloying and heat treatments with regrinding steps.

This synthesis method led to the formation of highly anisotropic particles of Ni_2ZnB and Ni_3ZnB_2, as proven by the following analysis. Rietveld refinements (**Figure 9**) of the powder X-ray diffraction (PXRD) patterns were conducted on both products. Severe intensity mismatches (**Figure 11**) were initially observed mainly for the 00*l* reflections, but they were successfully corrected using preferred orientation refinement along the *c*-axis, hinting at layered morphologies of the two samples. Indeed, high-resolution scanning electron microscopy (HRSEM) images of the bulk Ni_2ZnB and Ni_3ZnB_2 products showed highly stacked thin sheets (**Figures 12 and 13)**. The PXRD refinement results confirmed the expected crystal structures and no impurity peaks were detected, hinting at almost single-phase syntheses, but SEM backscattering imaging detected small Ni-rich impurity inclusions in the samples (see **Figure 14**). Energy dispersive X-ray spectroscopy (EDS) through elemental mapping confirmed the presence of all elements and their homogeneous distribution in both samples (**Figures 13)**. Inductively coupled plasma (ICP) spectroscopy measurements provided a Ni:Zn ratio of 3.16:1 and 2.20:1 for Ni_3ZnB_2 and Ni_2ZnB, respectively. The slight deviation of the ICP results from the ideal Ni:Zn ratios is likely due to the Ni-rich impurity inclusions mentioned above. Furthermore, selected area electron diffraction (SAED) from a transmission electron microscopy (TEM) image of a Ni_3ZnB_2 thin particle confirmed its crystallinity with diffraction peaks indexed according to its crystal structure (space group *C*2/*m*, **Figure 15**).

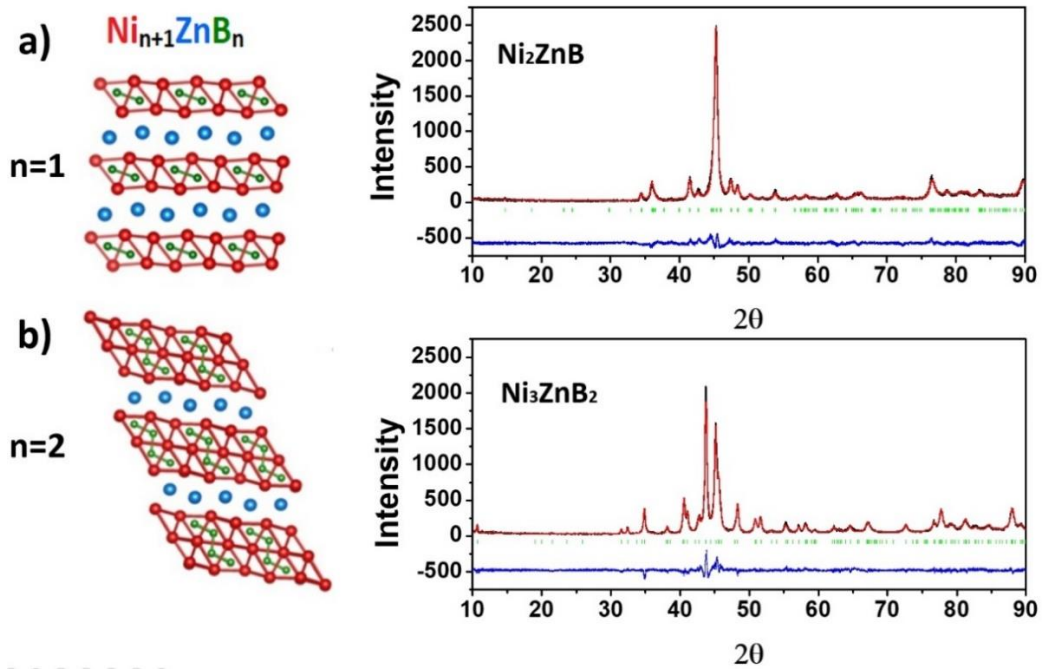

Figure 9. Crystal structures and Rietveld refinements of the powder XRD patterns of Ni_2ZnB (a) and Ni_3ZnB_2 (b). The red and the black curves represent the measured and the calculated patterns, respectively, whereas the blue curves show the intensity difference. The positions of the Bragg peaks are shown in green.

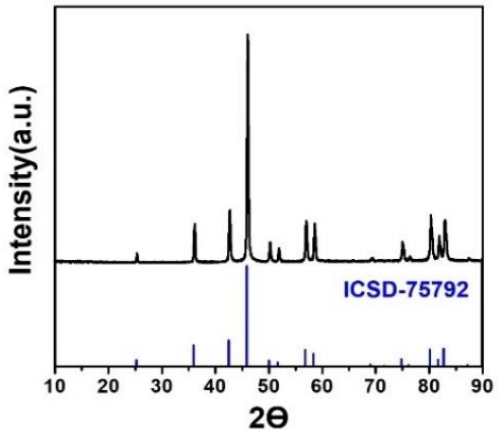

Figure 10. Powder XRD analysis of Ni_2B master alloy arc-melted prior to MAB Synthesis

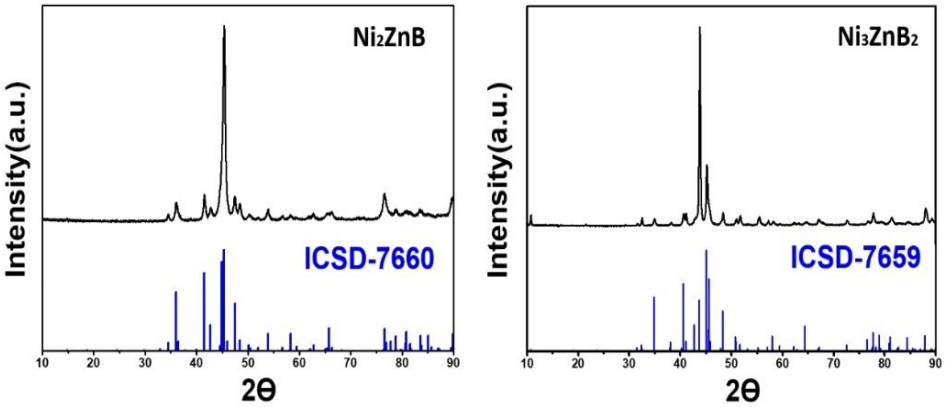

Figure 11. Powder XRD analysis of (a) Ni_2ZnB and (b) Ni_3ZnB_2 showing intensity miss matches when compared with theoretical patterns (blue), indicating preferred orientation of the crystallites.

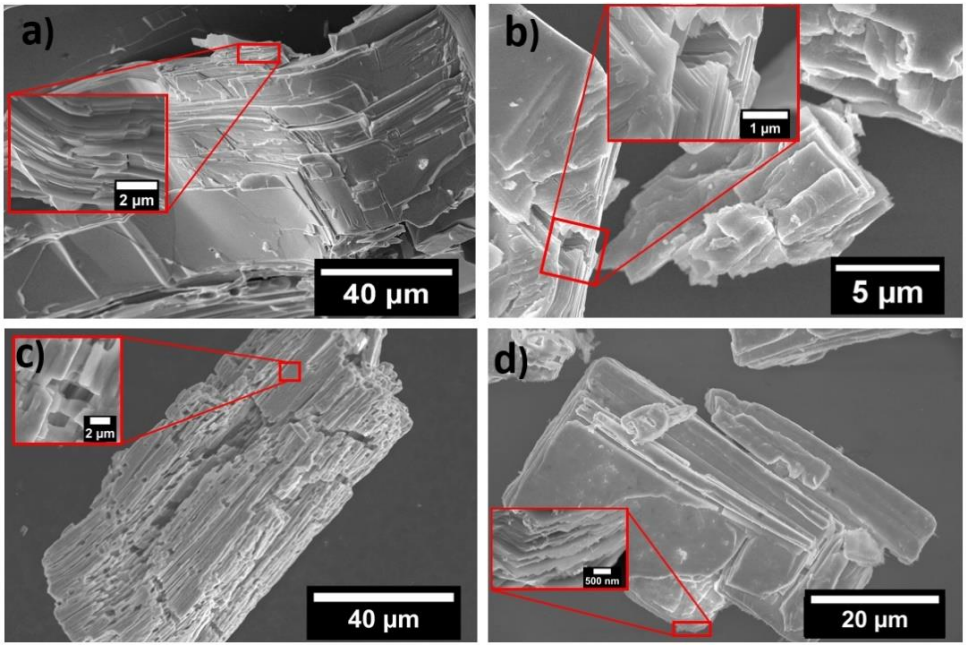

Figure 12. SEM images of the as-synthesized (a and b) and the 72hr HCl-etched (c and d) samples of Ni_2ZnB (a, c) and Ni_3ZnB_2 (b, d).

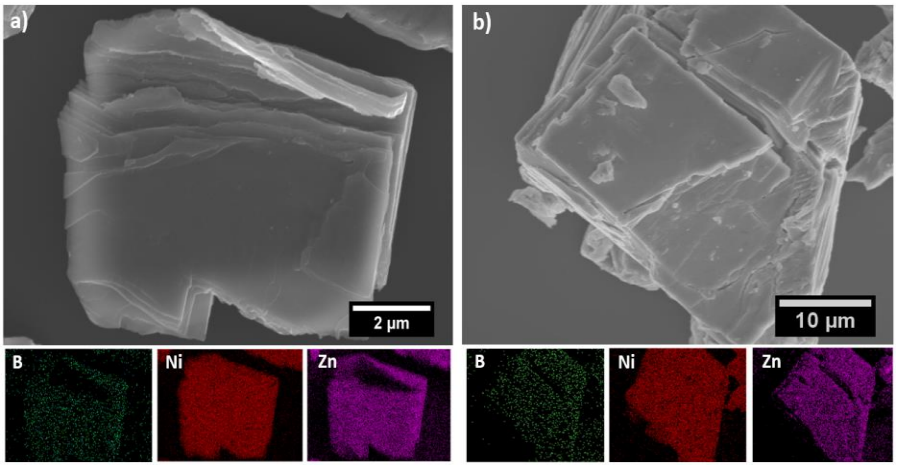

Figure 13. SEM image and EDS Analysis of as synthesized and un-etched (a) Ni_2ZnB and (b) Ni_3ZnB_2

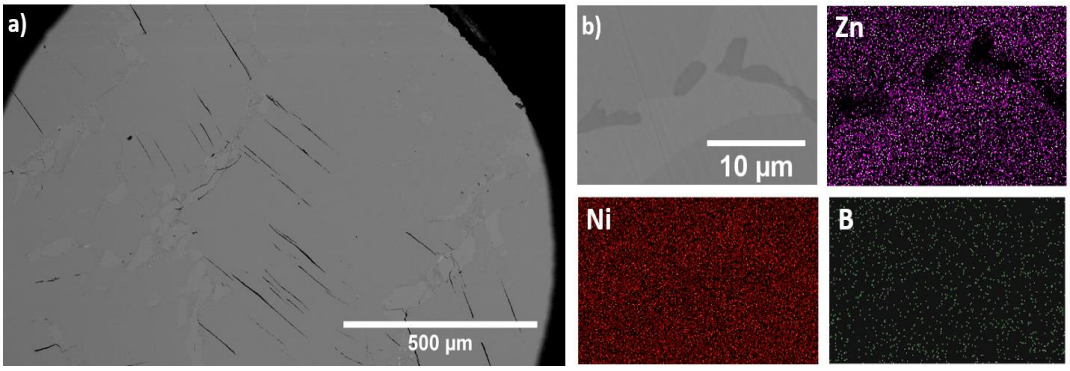

Figure 14. Backscattering SEM image of (a) as synthesized Ni_2ZnB button and (b) an enlarged part showing Ni-rich inclusions as proved by EDS Analysis.

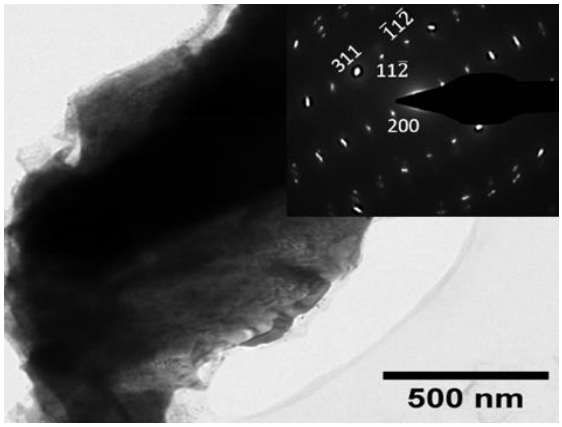

Figure 15. TEM image of a sonicated Ni_3ZnB_2 crystal and its selected area diffraction showing diffraction spots corresponding to the Ni_3ZnB_2 crystal structure (space group C2/m).

To investigate the possible Zn etching from Ni_2ZnB and Ni_3ZnB_2 bulk samples, several etchants (HCl, NaOH and $FeCl_3$/HCl) were tried. However, we found that only 1M HCl had the most promising results. The Ni_2ZnB and Ni_3ZnB_2 bulk samples were powdered and treated with 1M HCl acid for 72 hours. The prepared solutions were regularly shaken and ultrasonicated every 8 hours for about few minutes. Ultrasonication broke the bulk crystals into small pieces thereby accelerating the acid etching. After 72 hours, most of the sample had precipitated, leaving an almost colorless solution, an indication that a complete Zn removal, as observed in the case of Al etching in MAX phases such as $Ti_{n+1}AlC_n$, has not occurred. Instead, very small amounts of etched materials were obtained, and our preliminary analysis suggests that they contain less Zn than the bulk and the precipitated samples, thereby hinting at only partial etching, as observed in recent etching studies on Al-based MAB phases.[66, 74, 75] The acid-treated Ni_2ZnB and Ni_3ZnB_2 precipitates were investigated by PXRD, SEM, EDS, and ICP. According to PXRD, the Ni_2ZnB and Ni_3ZnB_2 samples remained crystalline, and their crystal structures did not change during the etching process (**Figure 16**). However, their morphologies were affected, as shown by SEM images in **Figures 12**. The SEM analysis of the etched Ni_2ZnB crystals shows that the top sheets were attacked by HCl leading to the emergence of pores and layer openings (**Figures 12c**). The pore sizes ranged from 100 nanometers to a few micrometers. The SEM analysis of etched Ni_3ZnB_2 crystals indicated that the top sheets were not attacked by the acid, as only the layer openings were observed (**Figure 12d**). This finding reveals that Ni_3ZnB_2 has more robust layers than Ni_2ZnB, which may be due to the thickness differences of the Ni-B slabs (**Figure 9 left**). Since our chemical analysis showed the same composition between these precipitates and the unetched samples, we hypothesize that the layer opening observed after etching is due to the ultrasonication. We are currently carrying out further ultrasonication experiments in different solutions to verify this hypothesis.

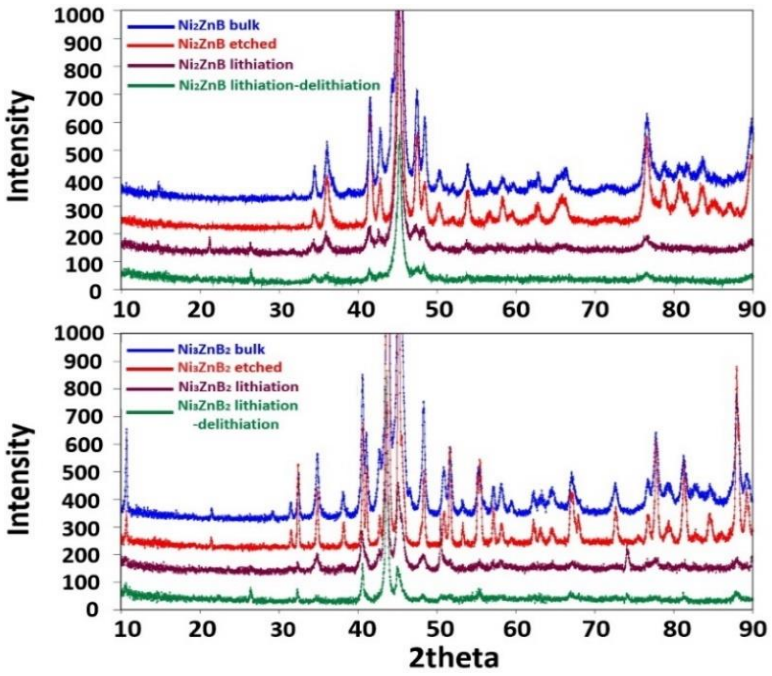

Figure 16. Magnified powder XRD patterns of (a) Ni_2ZnB and (b) Ni_3ZnB_2 before etching (blue), after etching (red), after lithiation (magenta) and lithiation-delithiation (green) cycle.

The BET surface areas of etched Ni_2ZnB and Ni_3ZnB_2 are 95.9 $m^2 g^{-1}$ and 0.7 $m^2 g^{-1}$, respectively. The pristine materials did not produce meaningful BET values, with the best measurement leading to a negligible value of 0.03 $m^2 g^{-1}$, indicating orders of magnitude improvement of the surface area after the acid treatment. After etching, the newly exposed surfaces are believed to be terminated by hydroxide or oxide groups like in MXenes. These surface species are capable of reversible redox reactions, thus interesting electrochemical properties relevant to battery materials can be expected. We have therefore examined the etched MAB phases in Li-ion half-cells using Li foil as the counter electrode. The MAB electrode was composed of 80 wt.% of Ni_2ZnB (or Ni_3ZnB_2), 10 wt.% of polyvinylidene difluoride (PVDF) as binder, and 10 wt.% of acetylene black as the conductive additive. **Figure 17a** shows the cycle stability and coulombic efficiency (CE) under various

lithiation-delithiation rates of 20 mA g^{-1}, 100 mA g^{-1} and 300 mA g^{-1}. At 20 mA g^{-1}, the first lithiation capacity of Ni_2ZnB electrode was approximately 180 mAh g^{-1} and a reversible capacity of ~110 mAh g^{-1} was achieved. At higher rates, the reversible capacities were ~90 mAh g^{-1} at 100 mA g^{-1} and ~70 mAh g^{-1} at 300 mA g^{-1}. The first cycle coulombic efficiency (CE) was 49.2% at 20 mA g^{-1}, and the CE in the following cycles improved fast to an average value of 99.3 %. In all the specific capacity measurements, Ni_2ZnB demonstrated a 20 mAh g^{-1} (at 100 mA g^{-1}) higher specific capacity than Ni_3ZnB_2 (**Figure 17a, middle**), which is likely due to the higher surface area of etched Ni_2ZnB. Both materials demonstrate excellent cycle stability with a slight incremental trend of capacity, which most probably results from accessibility of Li ions to active sites that has improved upon cycling.[34] The powder XRD analysis of the MAB phases after the first lithiation and delithiation (**Figure 16**) shows that the crystal structures of Ni_2ZnB and Ni_3ZnB_2 are retained. However, the intensity of the peaks significantly decreased, indicating that the crystallinity is reduced in these materials upon electrochemical reaction with Li. The representative lithiation-delithiation potential curves and cyclic voltammograms (CV) are shown in **Figure 17 (b-e)**, and both methods indicate significant irreversibility in the first cycle (leading to low initial CE), a behavior also reported for similar materials such as MXenes and their composites. To understand the origin of the irreversible capacity, the oxidation states of the surface elements were analyzed by X-ray photoelectron spectroscopy (XPS) after the acid etching, the first lithiation, and the first delithiation. As shown in **Figure 18a**, the Ni species on the surface of Ni_2ZnB after etching include metallic Ni (Ni $2p_{3/2}$ at 852.6 eV), Ni^{2+} (Ni $2p_{3/2}$ at 854.0 eV), and Ni^{3+} (Ni $2p_{3/2}$ at 855.6 eV). After the first lithiation the Ni^{3+} species was completely reduced to lower oxidation state. The Ni^{2+} species was also significantly reduced (using the peak of metallic Ni as the standard). After the delithiation, Ni^{3+} species re-emerged, however, the lower peak intensity relative to the etched sample indicates that the redox reaction of nickel is not completely reversible in the first cycle. The Zn species

(**Figure 18b**) on the surface of etched Ni_2ZnB show two states including metallic Zn (Zn $2p_{3/2}$ at 1021.9 eV) and an oxidized state (Zn $2p_{3/2}$ at 1026.3 eV). After the first lithiation, the oxidized Zn is completely reduced to the metallic state, and this reduction process is irreversible indicated by the XPS Zn 2p spectrum after the delithiation. As displayed in **Figures 18c** and **18d**, the Ni and Zn surface species on Ni_3ZnB_2 show the same behavior as observed in Ni_2ZnB. The surface boron species in both compounds are inert as indicated by their XPS B 1s spectra. Therefore, we suggest that the electrochemical redox reactions of Ni species on the surface contribute to the electrochemical performance of these two MAB phases. The irreversible reduction of Ni and Zn species in the first cycle is a major cause for the low initial CE in addition to the possible side reactions of solid electrolyte interphase formation.

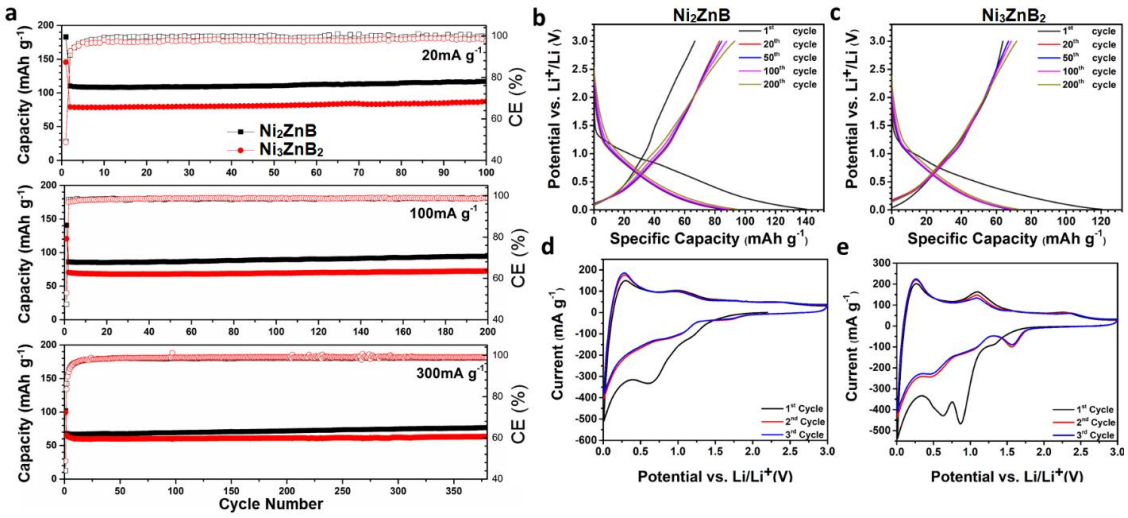

Figure 17. Electrochemical characterizations of Ni_2ZnB and Ni_3ZnB_2 electrodes. (a) Cycle stability of Ni_2ZnB and Ni_3ZnB_2 at various current rates; Representative lithiation and delithiation curves of (b) Ni_2ZnB and (c) Ni_3ZnB_2 at the rate of 100 mA g-1; Cyclic voltammetry of (d) Ni_2ZnB and (e) Ni_3ZnB_2 at 1 mV s^{-1} scan rate from 0.01 to 3.0 V vs Li/Li^+.

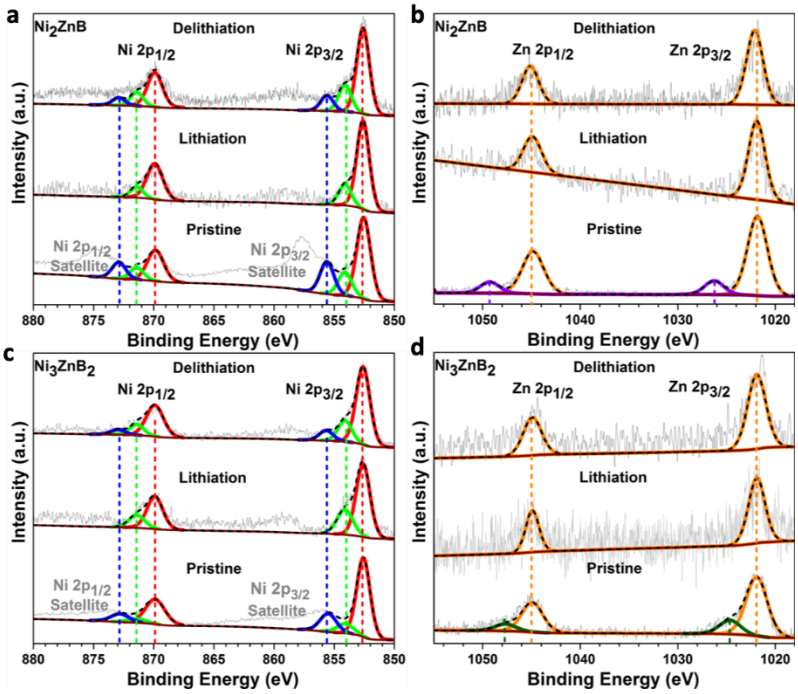

Figure 18. XPS Ni 2p and Zn 2p spectra of Ni_2ZnB (a, b) and Ni_3ZnB_2 (c, d) after acid etching (pristine) and after the first lithiation-delithiation cycle.

3.3 Conclusion

In this study, the syntheses of the MAB phases $Ni_{n+1}ZnB_n$ (n = 1, 2) were systematically investigated. The synthesized MAB phases were exposed to dilute HCl in order to study the effect of etching on their crystal structure. It was seen that most of the sample get partially attacked by the acid and form pores and sheet openings. These pores may have formed due to small Ni rich impurities in the microstructure. The battery performances of the unetched and etched MAB phases were investigated. While the bulk Ni_2ZnB and Ni_3ZnB_2 were not active, the etched phases showed a capacity of ~90 $mAhg^{-1}$ and ~75$mAhg^{-1}$, respectively. XPS and BET analyses suggest that increased surface area and electrochemical redox reactions of surface Ni species are responsible for the drastic change in battery performances. Future works should focus on increasing the surface area of these and other MAB phases containing elements that can undergo redox reactions toward applications in various metal-ion batteries.

Acknowledgements

This work was supported by the startup fund to BPTF at UC Riverside and the National Science Foundation Career award to BPTF (no. DMR-1654780). The CFAMM center at UC Riverside for electron microscopy and microanalysis. All the battery performance measurements and XPS analysis was done by Dr. Guo lab at UC Riverside.

Chapter 4

Highly Active and Abundant MAB phases $Ni_{n+1}ZnB_n$ (n = 1, 2) Toward Hydrogen Evolution

In this chapter we go through the electrocatalysis behavior of the proposed MAB phases for hydrogen evolution for the first time. We investigate different electrode forms of this MAB phase, demonstrating the pressed pellet with abundant basal plane surface, provides the lowest overpotential between all other MAB/MAX phases studied up to date. This chapter is adapted from the published manuscript:

DOI: *10.1002/aesr.202100052* - **Rezaie AA**, Lee E, Yapo JA, Fokwa BP. Advanced Energy and Sustainability Research:2100052.

4.1 Introduction

Fossil fuels attenuation and their hazardous impact on the environment have made alternative renewable energy sources highly attractive. Among all the renewable clean energy sources, hydrogen has been one of the most promising candidates due to its high energy density and numerous production routes.[88] Electrochemical water splitting through hydrogen evolution reaction (HER) is the most attractive method to produce hydrogen.[89] However, high cost and scarcity of the most efficient electrocatalysts (Platinum group metals) have made the process more challenging.[90] Thus, the study of highly active and abundant electrocatalysts would provide a path for a more sustainable and clean energy supply.

Two-dimensional materials such as graphene [3, 4], borophene [91, 92], phosphorene [93], *h*-BN [5], transition metal dichalcogenides (TMDs) [6] etc. have received a great deal of attention during the previous years due to their unique and enhanced properties compared to their parental bulk

forms. MoS_2, which is one of the most studied 2D materials for the HER is known to have only active edge sites, thus its basal plane is inactive making it a poor catalyst in bulk form.[94-96] In fact most TMDs have the same behavior. Therefore, discovering other two dimensional/layered materials which show HER active basal plane is of high current interest.[97] Recently, a new family of 2D carbides and nitrides named MXenes have seen high interest for a wide variety of applications including HER.[36] These 2D materials are directly exfoliated from their parent layered MAX phases ($M_{n+1}AX_n$ where M: Early transition metal, A: Main group element, X: C/N) by selectively etching out the "A" atoms.[7, 15] Similar to most TMDs, MAX electrocatalysts are not competitive towards HER. [14] In fact, they exhibit overpotentials (η_{10} at -10 mA/cm^2) ranging from -0.74 V to -0.88 V to drive a current density of -10 mA/cm^2.[98] Interestingly, theory suggests MXenes are more catalytically active in their doped form X-M_2C (X= B, N, P, S – M= Mo, Ti) compared to their pristine M_2C form.[99] A MAX-related family of layered ternary borides, called MAB phases is currently receiving increased interest.[8] Compared to MAX phases, MAB phases hold a large variety of structures. Typical MAB phases containing aluminum as the "A" element exhibit orthorhombic symmetry. However, they are more diverse and include phases such as hexagonal Ti_2InB_2 [72], tetragonal $Y_5Si_2B_8$ [76], tetragonal Ru_2ZnB_2 [100], hexagonal Cr_5Si_3B [47], hexagonal *i*-MAB phases [56], and monoclinic $Ni_{n+1}ZnB_n$.[70] Even though these MAB phases are chemically and structurally different from the MAX phases, they have similar properties such as high electrical conductivity [46], stiffness [46], and resistance to thermal shock.[63] In contrast to MAX phases whose chemical exfoliations to produce MXenes have been extensively studied, the exfoliation of MAB phases is still in its infancy, and only partially etched samples have been reported.[63, 66, 74, 75] Interestingly, partially etched MoAlB samples are active electrocatalysts for HER with η_{10} values of -0.40 V and -0.31 V, respectively.[66] The activity was ascribed to the exposed active basal plane sites due to partial Al-etching. Similarly, bulk Fe_2AlB_2 was found to be an excellent

OER electrocatalyst.[101] Consequently, the studied bulk MAB phases have shown far better electrocatalytic properties than their analogous MAX phases, hinting at an even greater potential for MBenes as future electrocatalyst candidates. While the synthesis of MBenes is still elusive they have been predicted as promising alternative candidates to substitute Pt as HER catalysts.[77] More theory studies have suggested MBenes as potential catalysts for nitrogen reduction reaction (NRR) and HER upon embedding single atoms such as V and Zn. Two studied Zn-$W_2B_2O_2$ and V-$W_2B_2O_2$ show close free Gibbs energy values to the upper point of the famous volcano plot (ΔG_H = -0.146 eV and 0.013 eV.[102, 103] However, the bulk MAB phases are still unexplored and warrant more attention given the above results and the fact that abundant bulk borides, especially those with layer-like AlB_2-type structures have been demonstrated to have excellent HER activities.[45, 104, 105]

Herein, we investigate $Ni_{n+1}ZnB_n$ MAB borides as HER catalysts for the first time. We demonstrate that a pellet electrode of $Ni_{n+1}ZnB_n$ exhibits abundant basal plane active sites that drive a 10 mA/cm^2 current density at the lowest overpotential of all MAB, MAX phases and their derivatives MXenes so far reported. In addition, we have carried out free energy density functional theory (DFT) calculations which have indeed identified many active sites on the Ni basal planes of these MAB phases.

4.2 Results & Discussion

The Ni-Zn-B system is very attractive, and many ternary phases have been discovered.[57-59] Among these phases, Ni_2ZnB and Ni_3ZnB_2 have an atomically laminated structure similar to all MAX/MAB phases. On the one hand, these monoclinic structures differ from the typical MAX phase $P6_3/mmc$ symmetry and the common orthorhombic MAB structure. On the other hand, they hold a general chemical composition ($Ni_{n+1}ZnB_n$) similar to MAX phases ($M_{n+1}AX_n$).[57, 70]

Phase-pure samples of $Ni_{n+1}ZnB_n$ (n = 1, 2) were synthesized as described previously in chapter 2 & 3. As shown in **Figure 19,** the Rietveld-refined powder X-ray diffraction (PXRD) patterns of both bulk phases show single-phase products. However, severe intensity mismatches were observed mainly for the (*00l*) reflections, but they were corrected using preferred orientation refinement along the *c*-axis, indicating a possible layer-like morphology of the samples. Indeed, scanning electron microscopy (SEM) images of the bulk products confirmed a stacking of thin sheets (**Figure 19**). Furthermore, the presence of the elements and their homogenous distribution were confirmed through Energy Dispersive X-ray Spectroscopy (EDS) and mapping, respectively (**Figure 20**).

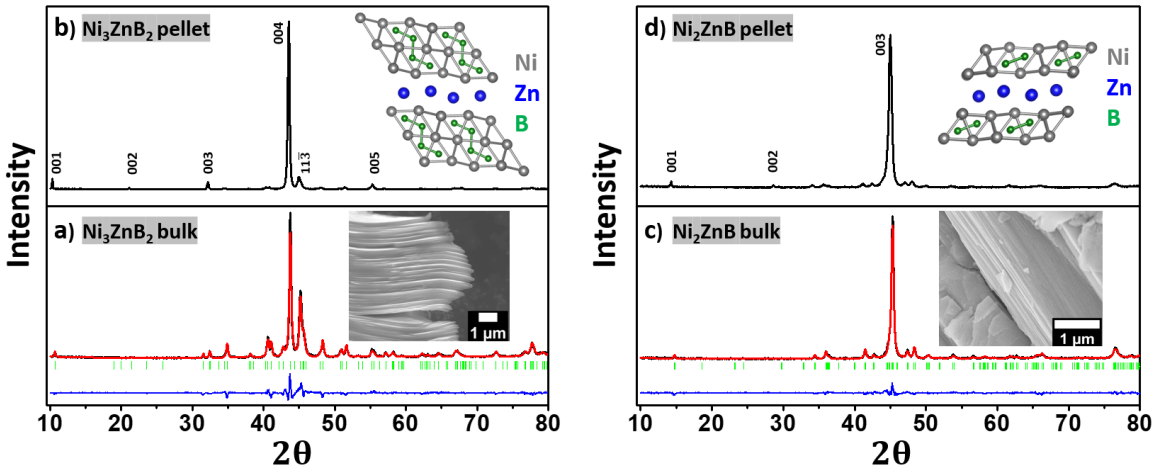

Figure 19. XRD patterns of a) as synthesized bulk Ni_3ZnB_2, b) pressed Ni_3ZnB_2 pellet c) bulk Ni_2ZnB, and d) pressed Ni_2ZnB pellet. Insets are the SEM images (a and c insets) and the crystal structures (b and d insets) of the two phases.

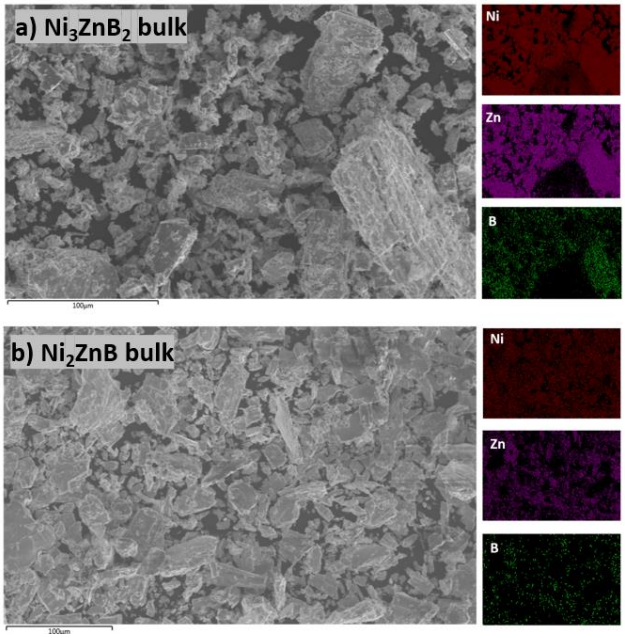

Figure 20. Elemental mapping of the MAB particles a) Ni_3ZnB_2 bulk b) Ni_2ZnB bulk.

X-ray photoelectron spectroscopy (XPS) was used to investigate the surface species on the synthesized Ni_3ZnB_2 and Ni_2ZnB powders. **Figure 21** shows that the Ni 2p, Zn 2p and B 1s spectra of the two phases are expectedly similar, and the peak fitting values are given in **Table 2**. The Ni 2p spectrum is deconvoluted into Ni $2p_{1/2}$ and Ni $2p_{3/2}$, which are composed of two different peaks corresponding to Ni^{2+} and Ni^0 species.[106, 107] In both phases, the metallic Ni^0 peaks show by far the highest intensities if compared to the Ni^{2+} peaks, indicating that the nickel oxide layer (from atmospheric exposure) present on the surface of these MAB phases is so thin that the bulk boride underneath dominates the XPS spectrum. A similar observation can be made for the Zn species, but the opposite situation is found for the B species. The Zn 2p spectrum is deconvoluted into Zn $2p_{1/2}$ and Zn $2p_{3/2}$ which are each composed of Zn^{2+} peaks from the thin zinc oxide layer and the Zn^0 peaks of the boride underneath.[108] The B1s spectra of both Ni_2ZnB and Ni_3ZnB_2 are each composed of two peaks corresponding to B^{3+} and B^0, the oxide peak being more intense than the

boride one. These XPS results indicate that all the above-mentioned species are present on the surfaces of these materials, thus suggesting them as potential active species for HER.

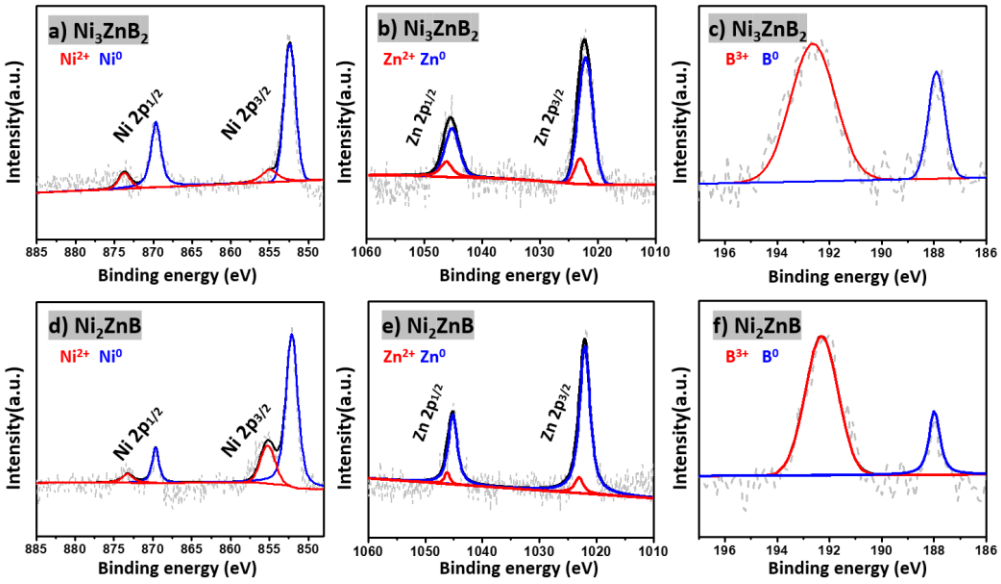

Figure 21. X-ray photoelectron spectroscopy spectra of Ni 2p, Zn 2p and B 1s for a-c) bulk Ni_3ZnB_2 and d-f) bulk Ni_2ZnB (dash line = measured data, solid line = fitted data).

Table 2. XPS peak position of Ni_3ZnB_2 and Ni_2ZnB for different surface species.

Phase	Species	Peak Position(eV)
Ni_3ZnB_2	Ni^0	852.4, 869.6
	Ni^{2+}	854.9, 873.4
	Zn	1022.1, 1045.2
	Zn^{2+}	1023.0, 1046.1
	B	187.9
	B^{3+}	192.6
Ni_2ZnB	Ni^0	852.1, 869.6
	Ni^{2+}	855.2, 873.1
	Zn	1022.03, 1045.11
	Zn^{2+}	1023.0, 1046.1
	B^0	187.9
	B^{3+}	192.3

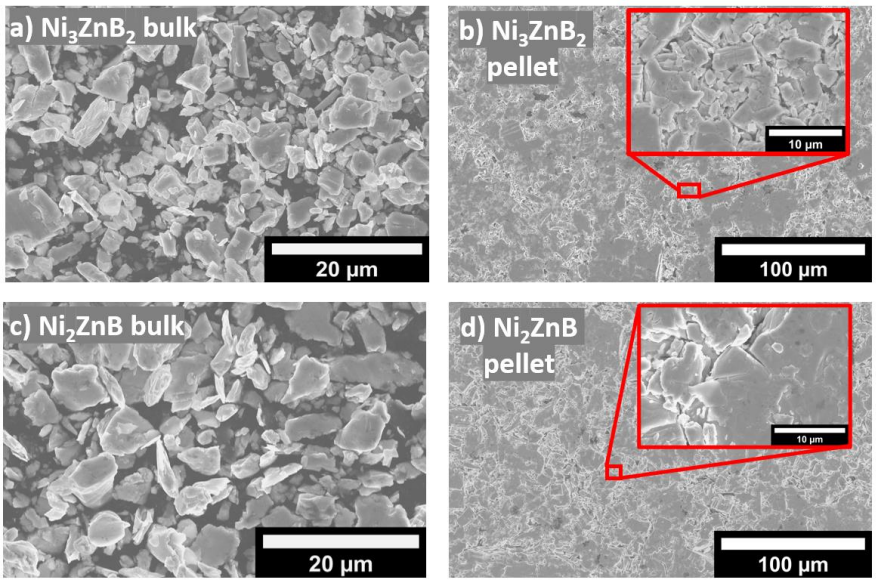

Figure 22. SEM micrographs of crushed bulk powders of a) Ni_3ZnB_2 and c) Ni_2ZnB and the corresponding pressed pellet electrodes (b and d).

To investigate the electrocatalytic HER activity of $Ni_{n+1}ZnB_n$, the crushed MAB particles (**Figures 22a and c**) were drop casted on a carbon cloth electrode using Nafion as a binder and examined in a 1 M KOH solution (check chapter 2 for details). The linear sweep voltammetry (LSV) curves show good performances for Ni_3ZnB_2 and Ni_2ZnB, requiring overpotentials (η_{10}) of -0.25 and -0.31 V, respectively, to reach a current density of 10 mA/cm^2 (**Figure 23a**). These values far exceed those of other experimentally evaluated MAB/MAX phases for HER. MAX phases generally do not show good catalytical activity. Among all the MAX phases, Mo_2Ga_2C was reported as one of the most promising HER electrocatalysts with an overpotential η_{10}= -0.74 V, [36] and the two most studied MAX phases, Ti_2AlC and Ti_3AlC_2, have even higher overpotential values (**Figure 23d**).[98] Interestingly, the few studied MAB phases are better electrocatalysts if compared to the MAX phases. MoAlB for example has the best HER activity so far with an overpotential of -0.40 V at 10 mA/cm^{-2} for non-etched crystals.[66] The lower overpotential of Ni_3ZnB_2 if compared to Ni_2ZnB may be due to the different metal to boron ratios. Previously, our group discovered a boron

dependency of molybdenum and vanadium borides electrocatalysts for HER.[45, 109] We found that the lower the M:B ratio (higher boron content) the better the overall HER activity. Interestingly, the 2 new electrocatalysts are significantly better than the two reported bulk metal-rich borides to date (Mo_2B, η_{10}= -0.41 V [45] and MoAlB, η_{10}= -0.40 V) despite having similar or even higher M:B ratio. One reason may be the presence of late transition metals (Ni and Zn), another may be related to the difference in the M:B ratio which affects the type of boron bonds in these MAB structures. In fact, Ni_3ZnB_2 shows not only a low M:B content (M:B = 2:1) but it also has the most B-B bonds (B_4 zigzag units) if compared to Ni_2ZnB (M:B = 3:1 and B_2 dumbbells). These arguments indeed support the 18 % lower overpotential observed for Ni_3ZnB_2.

As shown in **Figures 19 and 22** and as reported previously, the investigated bulk polycrystalline Ni_2ZnB and Ni_3ZnB_2 phases already hold a preferred orientation along the *c* direction (dominating basal planes), meaning that the basal planes may be preferably exposed during HER, hinting at a dominant role for the basal planes in the overall activity of these borides. To study the effect of the basal plane on the HER activity, new electrodes were prepared by pressing the powdered MAB phases to pellets using a die set (using a hydraulic press at room temperature, see SI for more details). This method exposes more basal planes of the MAB particles parallel to the force direction, forming a pellet with even more pronounced preferred orientation along the [*00l*] direction, as confirmed by PXRD (**Figure 19**) and through SEM images of the electrodes (**Figures 22b and 22d**). In fact, the PXRD patterns of the pressed pellet showed a single crystal-like behavior with mainly intensified (*00l*) peaks for both pellets. Other peaks were observed in the PXRD but with much smaller intensities if compared to the (*00l*) peaks. For instance, the $(11\bar{3})$ peak for Ni_3ZnB_2 should have been the highest intensity peak based on the theoretical pattern. However, after pressing only a small trace of this peak still prevailed while the (*00l*) peaks increased. To measure the HER activity of these pellet electrodes, the edges were covered with epoxy. Astonishingly, the

overpotentials of these pellet electrodes were lowered by 42-44 % if compared to the drop casted electrodes, reaching overpotentials of η_{10}= -0.14 V and -0.17 V for Ni_3ZnB_2 and Ni_2ZnB, respectively. These values are the lowest reported experimentally for any form of layered ternary metal-rich borides, to the best of our knowledge. This was further confirmed by measurements of the electrochemically active surface area through the double layer capacitance values (C_{dl} = 22.3 mF/cm^2 for n = 1 and 35.4 mF/cm^2 for n = 2) which were noticeably higher if compared to those of the drop casted electrodes (**Figures 24 and 25**). This drastic increase in the active area sites for the pellets, points to the role of the basal plane in the HER activity of these materials. The pellet also provides tightly packed MAB particles, thus facilitating the interlayer electron transfer in the electrode,[110] thereby increasing the activity. This was confirmed through charge transfer resistance (R_{ct}) measurements. In both cases the pressed pellets had much lower R_{ct} values if compared to the drop casted electrodes (**Figure 23c and Table 3**). Also, the Tafel plots (**Figure 23b**) of the pellet show smaller Tafel slope values if compared to the drop casted electrodes. These values fall near 120 mV/dec for the drop casted electrodes indicating that the Volmer reaction strongly controls the HER process for these electrodes.[111, 112] However, for the pellets, the Tafel slope values fall in between that of the Volmer reaction (Tafel slope ~120 mV/dec) and the Heyrovsky reaction (Tafel slope ~40 mV/dec), suggesting a more complex mechanism. Finally, the most active pellet electrodes were investigated for their long-term stability. The continuous cyclic voltammetry (CV) curve showed a good stability for all the electrodes after 3000 cycles with little change in the overpotential (**Figure 26**). Also, at high current density (-100 mA/cm^2) the pellet electrodes show better stabilities and activities if compared to the drop casted ones.

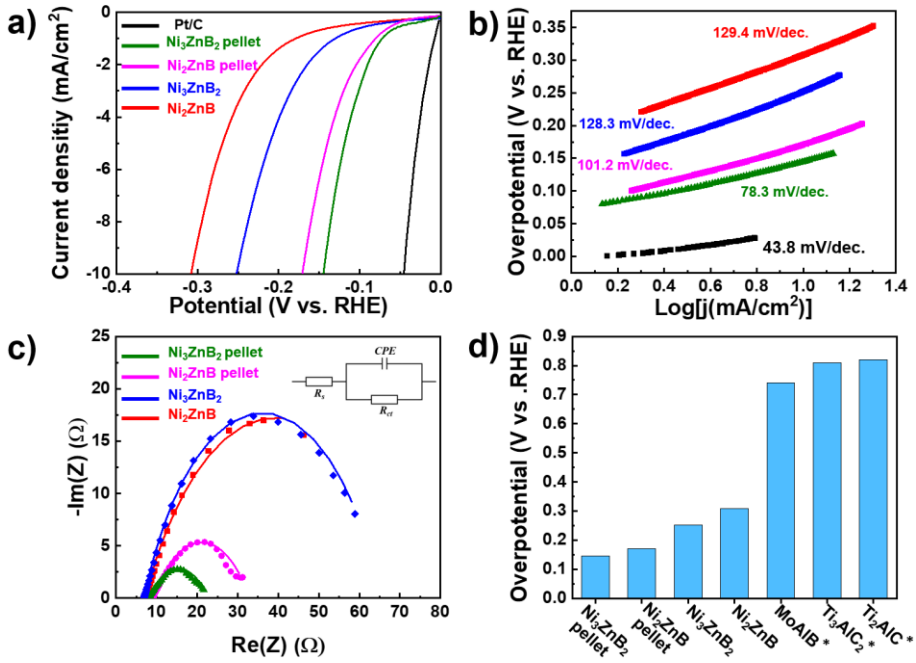

Figure 23. a) Polarization curves of various $Ni_{n+1}ZnB_n$ MAB electrodes in 1M KOH at a scan rate of 5 mV/s with iR-correction. b) Tafel plots derived from the polarization curves. c) Electrochemical impedance spectra (Nyquist plots): The points represent the experimental data, and the solid curves indicate the fitting lines. d) Overpotential of reported bulk MAB and MAX phases compared to different $Ni_{n+1}ZnB_n$ electrodes (* obtained from reference [98])

Table 3. Fitted EIS data.

	R_s [Ohm]	R_{ct} [Ohm]	CPE [F s^{a-1}]	a
Ni_2ZnB Bulk	7.08	64.51	0.017	0.626
Ni_2ZnB pellet	9.23	23.71	0.007	0.540
Ni_3ZnB_2 Bulk	6.96	58.26	0.0065	0.695
Ni_3ZnB_2 Pellet	8.18	14.61	0.0205	0.464

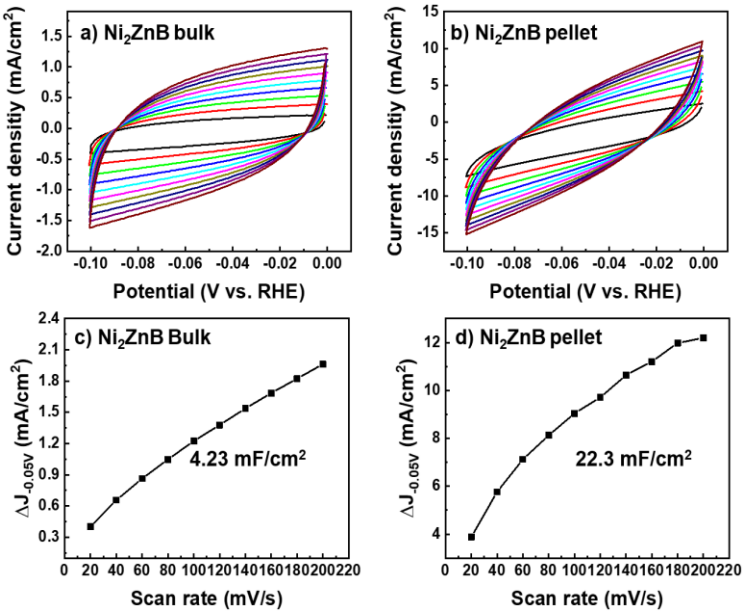

Figure 24. Cyclic voltammetry profiles and linear fitting of the capacitive currents versus scan rates obtained from cyclic voltammetry tests at 0.05 V vs. RHE to estimate Cdl for – a,c) Ni_2ZnB bulk b,d) Ni_2ZnB pellet.

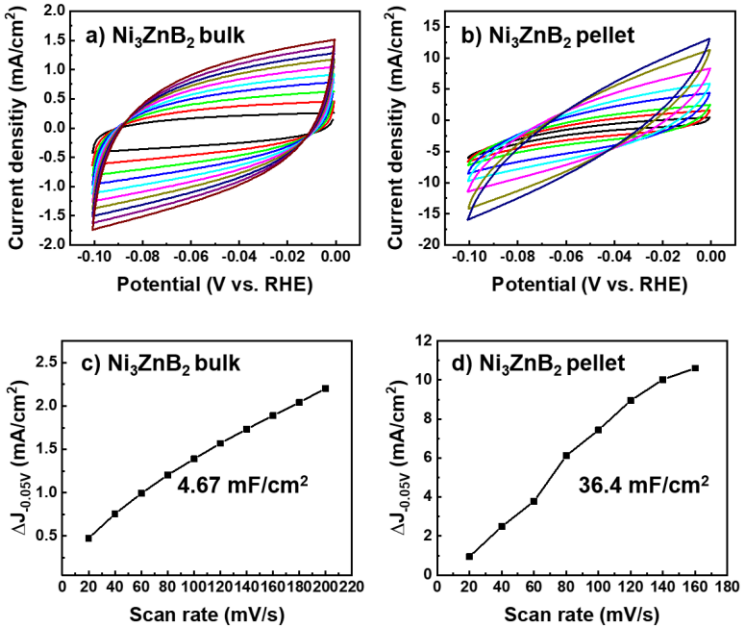

Figure 25. Cyclic voltammetry profiles and linear fitting of the capacitive currents versus scan rates obtained from cyclic voltammetry tests at 0.05 V vs. RHE to estimate Cdl for a,c) Ni_3ZnB_2 bulk, and b,d) Ni_3ZnB_2 pellet.

To understand the origin of high basal plane HER activity in these MAB borides, DFT calculations were carried out using the Gibbs free energy (ΔG_H) as the descriptor. In fact, ΔG_H for atomic hydrogen adsorbing on a catalyst surface has been shown to correlate with the experimentally measured HER activity of a variety of systems.[113, 114] Theoretically, the optimal HER activity is achieved when the ΔG_H value is close to zero since this ensures that the reaction rates for both H adsorbing and H_2 desorbing onto/off the surface is maximized. In this study, DFT calculations (at 25 % H coverage) were applied to survey the active sites on two surfaces for both Ni_2ZnB and Ni_3ZnB_2. Experimentally, the (00*l*) planes were found to dominate the PXRD patterns (**Figure 19**), indicating that they are the most exposed surfaces. Therefore, we have studied the (001) Ni- and Zn-terminated surfaces for their HER activities. It should be noted that the (00*l*) layer containing B atoms were not studied since for both Ni_2ZnB and Ni_3ZnB_2 structures the B atoms bond covalently with each other and with Ni atoms, in contrast to the weaker metallic bonds between Ni and Zn. The results for the Zn-terminated layer show that the considered sites are not as active as those on the Ni-terminated layer, thus they are not further discussed. The computed results for the Ni exposed surface for both materials are summarized in **Figure 27a**. The following three sites were found to be the most active for each surface (**Figures 27b and 27c)**; the hollow site (Hol) between three Ni atoms, the top site on a Ni atom (Top), and the site bridging two Ni atoms (Brdg). The calculated ΔG_H values for Ni_2ZnB were: -0.12 eV (Hol), 0.19 eV (Brdg), and 0.44 eV (Top); while -0.14 eV (Hol), 0.21 eV (Brdg), and 0.31 eV (Top) were obtained for Ni_3ZnB_2. From these values we can see that the Hol sites for both materials are the most HER active with ΔG_H values similar to that calculated for Hol Pt (111).[115] While the Top sites were the least active, they were still low enough to be considered as active sites. The ΔG_H values of Hol and Brdg sites are almost the same (0.02 eV difference) for the 2 phases, whereas those of the Top sites are significantly different (0.13 eV lower for Ni_3ZnB_2). This may explain the significantly better HER activity found

experimentally for Ni_3ZnB_2. These DFT results validate the experimental findings of high HER activity of both Ni_2ZnB and Ni_3ZnB_2 MAB phases, the latter being more active.

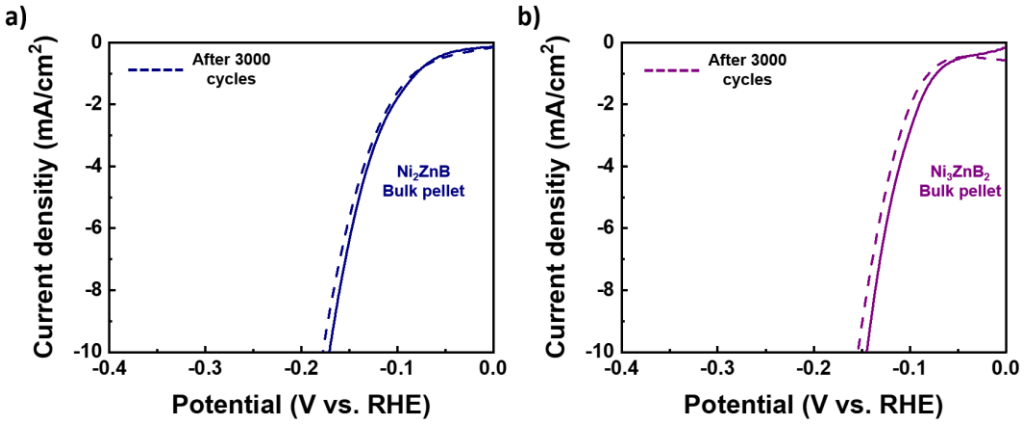

Figure 26. HER stability measurement of the pellet electrodes before and after 3000 cycles with a scan rate of 100 mV/s in 1 M KOH a) Ni_2ZnB bulk pellet b) Ni_3ZnB_2 bulk pellet.

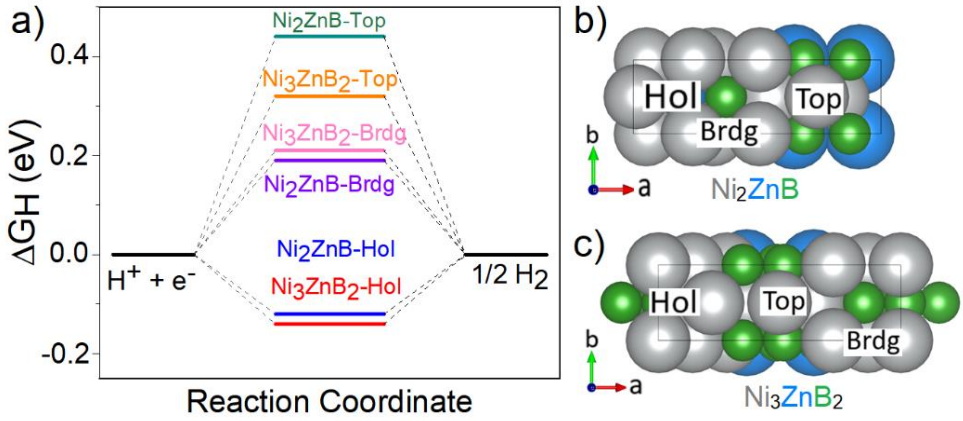

Figure 27. a) Gibbs free energy (ΔGH) of H-adsorption for different sites on the Ni exposed layer for both Ni_2ZnB and Ni_3ZnB_2. Superstructure models for b) Ni_2ZnB and c) Ni_3ZnB_2 showing the studied hollow (Hol), top (Top) and bridge (Brdg) sites.

4.3 Conclusion

The HER properties of different electrodes (drop casted and pressed pellet) of $Ni_{n+1}ZnB_n$ (n = 1, 2) MAB phases were investigated for the first time. The electrodes, analyzed through PXRD and

SEM, show high preferred orientation along the *c*-axis (exposed basal planes), the pressed pellet showing the highest. The pressed electrode had the best HER performance showing low overpotentials to drive a 10 mA/Cm^2 current density of - 0.17 V and - 0.14 V, for Ni_2ZnB and Ni_3ZnB_2, respectively. DFT free energy calculations showed that the nickel basal plane is more active than the zinc plane and that the hollow site is the most active site for both materials with free energy values close to that of the hollow site of Pt (111), thus supporting the experimental results. This study introduces $Ni_{n+1}ZnB_n$ as active basal plane electrocatalysts for hydrogen evolution and paves the way for applications of these and other MAB phases in clean energy reactions.

Acknowledgements

This work was supported by the startup fund to BPTF at UC Riverside and the National Science Foundation Career award to BPTF (no. DMR-1654780). The CFAMM center at UC Riverside for electron microscopy and microanalysis. This work used the Extreme Science and Engineering Discovery Environment (XSEDE), which is supported by NSF (no. ACI-1548562). The XPS data were collected with an instrument acquired through the NSF MRI program (DMR-0958796). I would like to thank Eunsoo Lee for performing the electrochemical testing and Johan Yapo for performing DFT Calculations.

Chapter 5

Fabrication of Nano Ternary Transition Metal Borides through a Simple Ultra-Sonication Technique

Herein, we go through the formation of nano Ni_3ZnB_2 through a simple ultrasonication technique in two different solutions. We investigate the layered morphology of the synthesized and sonicated MAB phase, its impact on exfoliation and finally compare the exfoliation yield and efficiency of this compound in ethanol and water media.

5.1 Introduction

The synthesis of graphene has introduced and inspired the formation of two-dimensional (2D) materials.[3, 4] Ever since, 2D materials such as phosphorene [93], h-BN [5], borophene [92], transition metal dichalcogenides (TMDs) [6] and very recently MXenes [7] have gained a great amount of attention due to their diversity and exclusive properties compared to their original bulk form. MXenes, a new family of 2D carbides and nitrides, are directly exfoliated from their parent layered MAX phases ($M_{(n+1)}AX_n$ – M: early transition metal, A: main group element, X: C, N). Very recently, ternary layered borides, a MAX related family, have become into high attention due to their layered structure and their capability to derive 2D transition metal borides (MBenes).[8] Contrary to MAX phases, whose chemical exfoliation to form MXenes have been extensively studied, the formation of 2D transition metal borides is still in its infancy and has not been studied much yet.[66, 74, 75]

Two-dimensional materials are mainly synthesized following two general methods: 1) top to bottom and 2) bottom to top. Chemical vapor deposition (CVD) is the most studied bottom-top method to synthesize 2D layers such as graphene and TMDs.[116, 117] However, the most conventional and studied method, is deriving 2D layers from analogous bulk solids consisting of

2D sheets stacking on each other. Mechanical exfoliation, known as scotch tape method, was applied as the very first method to form 2D graphene flakes from graphite.[3] However, this method is not scalable and is only applicable for vdW layered compounds. On the other hand, chemical exfoliation, is the most studied method to exfoliate non vdW layered materials. MXenes have been formed through chemically etching the "A" element out in the bulk MAX phases forming 2D MX layers. Although this method has been widely studied and MXenes show extraordinary properties, these 2D layers are mainly terminated with oxide, hydroxide or the etchant groups.[28, 29, 31] In order to increase the scalability, and limit the change in composition upon exfoliation, liquid-phase exfoliation (LPE) has been applied on bulk materials to form 2D layers, thin sheets and nano particles.[2, 26, 118, 119] In this method, the layered bulk material is sonicated in different organic or aqueous media. This causes the layered compound to exfoliate into thinner sheets due to materials inter-layer behavior. However, sonication may also cause fragment of the particles ending to smaller flakes.[6, 97]

Liquid phase exfoliation through ultrasonication has been widely used for vdW layered materials.[120] However, this method has been quit challenging to exfoliate non-vdW layered compounds such as MAX phases (exfoliated through selective etching).[26] Very recently, exfoliation of transition metal diborides, as ultra high-temperature ceramics (UHTC) materials has become interesting. MgB_2 is one of the most studied diborides for exfoliation in aquas solutions, led to formation chemically modified nano-sheets.[121, 122] Green et al. reported the formation of stable dispersion of different nano transition metal diborides in different aqueous solutions through bath and tip sonication.[118] Although TMBs have shown a potential of partial exfoliation toward nano sheets, there has not been a study on the other family of metal borides, such as MAB phases. Herein, we report in the exfoliation of Ni_3ZnB_2, as the first MAB phase studied for LPE, via two different exfoliation media (ethanol and DI water) as shown in **Figure 30**. It was observed that

Ni_3ZnB_2, holding a layered morphology (discussed in the previous chapters), potentially exfoliates forming nano sheets in both media. The nano-sheets formed a homogenous and steady colloidal dispersion in both cases. However, it was observed that the exfoliation yield is much higher in ethanol compared to DI water. The formed nano-sheets, and the colloidal dispersion were primarily studied via PXRD, and microscopy techniques to understand their morphology, lateral size, and crystal structure. This method may introduce a new method to form MAB nano and quasi 2D sheets (MABenes) for applications such as composite reinforcement fillers, additive manufacturing, and 3D printing.

5.2 Results and Discussion

Ni_3ZnB_2 (monoclinic, *C*2/*m*) was selected as the first MAB phase for liquid phase exfoliation. The synthesis, microstructure and morphology were reported in our previous works.[70, 123] This MAB phase consists of Ni-B slabs, sandwiched between zinc layers forming a layered morphology. It was observed that this nano-laminated compound tends to delaminate along its layers (basal plane delamination) upon applying sheer force. This may be due to weaker force between the layers, providing a paper like bending and delamination. **Figures 28 & 29** shows the basal delamination of Ni_3ZnB_2 crystals upon breaking them. This delamination has caused the formation of slabs ranging from couple hundred nano- to few micrometers. This hinted at the possible formation possibility of nano-layers upon more severe sheer forces and exfoliation energy. In the next step, the exfoliation of these MAB layers was investigated via the LPE method.

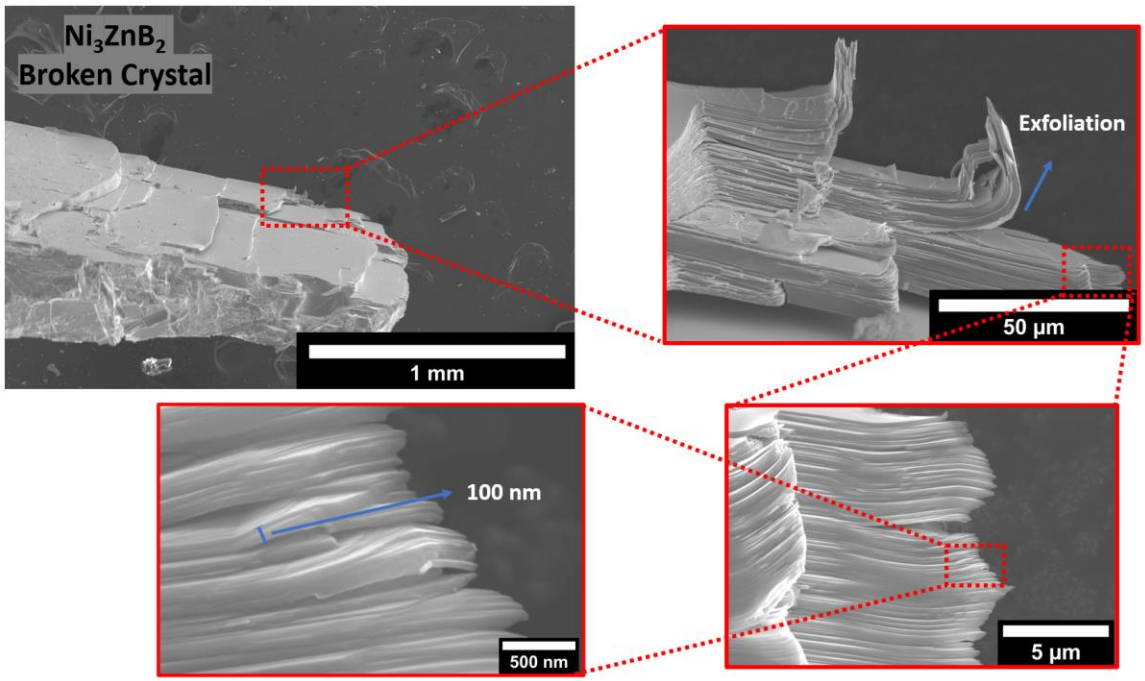

Figure 28. Ni_3ZnB_2 crystal delamination upon breaking

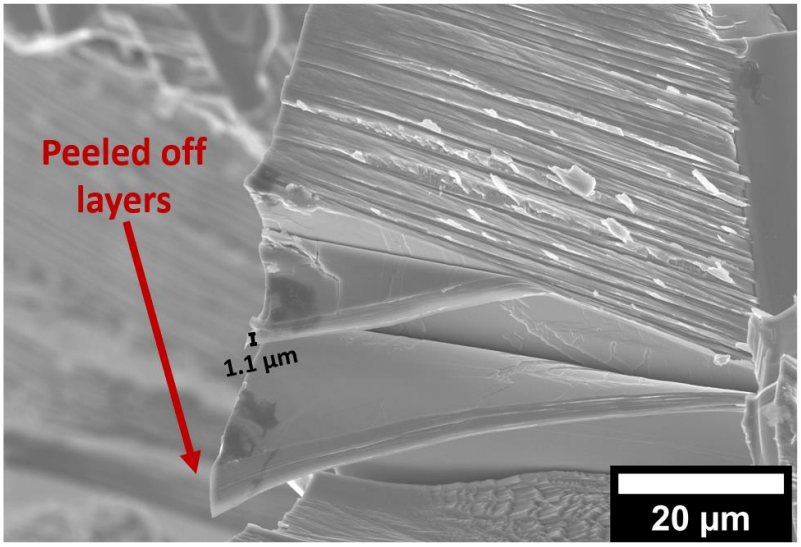

Figure 29. SEM image of Ni_3ZnB_2 peeled off layers

The Ni_3ZnB_2 MAB phase was ground and ultrasonicated in ethanol and water for 4 hours. The vials were put in a water-ice bath to avoid any heating and evaporation of solvents. Previously it was shown that for the transition metal borides the strength and mechanical properties of the compounds, the concentration of the solution and the solvent may affect the exfoliation yield.[118] Thus, a constant concentration of 25 mg/ml was selected for both trials. Four hours of sonication led to the formation of a colloidal dispersion for both ethanol and DI water media. On the one hand, after leaving the solution steady for 24hr, the aquas-based solution became transparent and turned toward a light-grey solution, hinting that most of the particles precipitated to the bottom of the vial. On the other hand, the colloidal solution in ethanol seems significantly more stable even after several days. The colloidal solutions and the Tindal effect of each are represented in **Figure 30**.

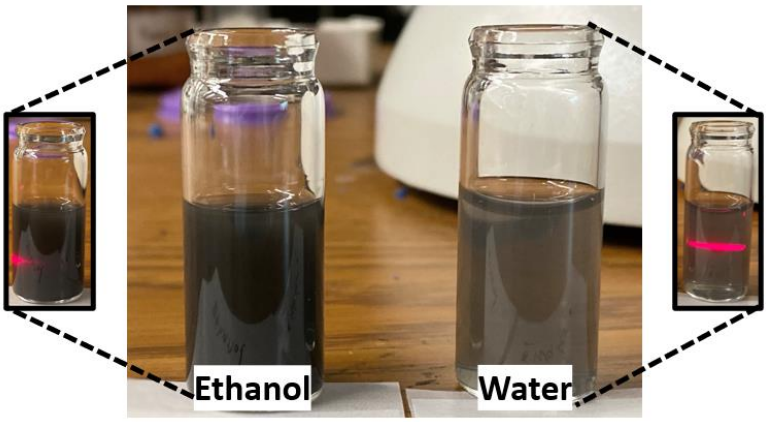

Figure 30. Liquid phase exfoliation of Ni_3ZnB_2 MAB phase - Colloidal dispersion of nano-particles in ethanol and water solvents after 24hrs

After 1hr of sonication, the colloidal dispersion of Ni_3ZnB_2 in ethanol was drop casted on a Si/SiO_2 wafer and analyzed for the initial particle size and the crystal structure of the particles. As shown in **Figure 31**, the particle size for the Ni_3ZnB_2 flakes had an average size from couple hundred nano meters all the way up to few microns. The yield of sonication is provided in **Table 4**. It was observed that ~ 11% of the MAB phases gets affected via sonication forming sub-micron particles.

However, upon time, the poorly exfoliated larger particles tend to precipitate leaving the smaller (nano-layers) particles behind. This observation hints that upon sonication, different centrifuge rates may collect and differentiate different size particles leading to collecting nano particles.

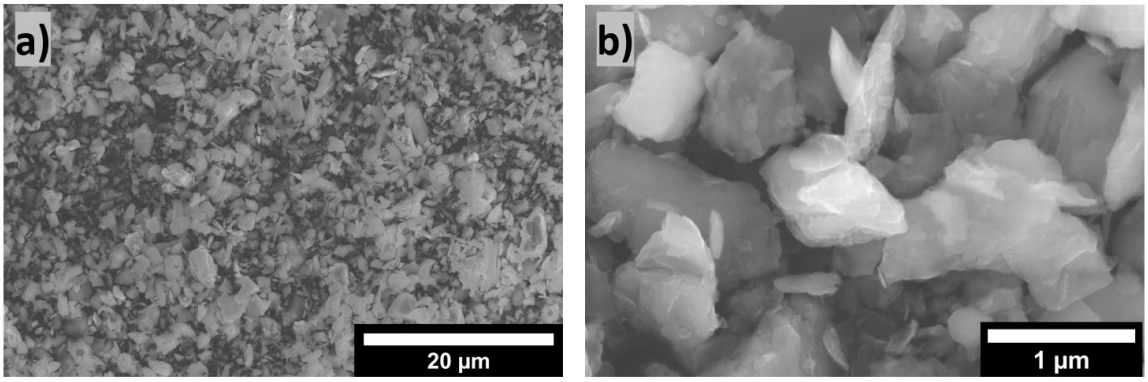

Figure 31. SEM images of drop-casted colloidal solution of Ni_3ZnB_2 in ethanol - 1hr steady

Table 4. Ni_3ZnB_2 sonication summery table

MAB Phase	Media	Steady Time	Yield %
Ni_3ZnB_2	Ethanol 4h	1h	~ 11.1 %
Ni_3ZnB_2	Ethanol 4h	24h	~ 3.5 %
Ni_3ZnB_2	Water 4h	24h	~ 1.5 %

Leaving the solution steady for 24 h, made the larger particles precipitate in the bottom of the vial. This led to the precipitation of the larger particles decreasing the sonication yield down to ~ 3%. The remaining floating particles in the colloidal solution were analyzed through PXRD and SEM to understand their morphology, particle size and any structural change which may have occurred upon sonication. The Tindal effect on the colloidal dispersion demonstrated the existence of nano

particles after 24 hours (**Figure 30**). In the next step, the supernatant was removed, and the floating nano particles were precipitated through centrifugation (all the particles were precipitated only after 10000 RPM – 7mins). After centrifugation, the supernatant was all clear and the Tyndall effect was not observed. **Figure 32** shows the powder XRD of the precipitated particles in comparison with the bulk Ni_3ZnB_2 MAB diffraction pattern. As seen in this figure, after 4h of sonication, the MAB phase maintains its monoclinic symmetry. However, the diffraction pattern for the collected particles show that the peaks have broadened and a decrease in intensity was observed hinting at a particle size decrease. This particle size decrease is more drastic for the 24h steady state (SS). The diffraction pattern for these particles show only the main two peaks at (004) and $(\bar{1}13)$ and all the other peaks are broadened and drastically reduced. The morphology of the nano sheets was observed under SEM. Flake like nanosheets with various lateral sizes and thicknesses were observed (**Figure 32**). These flakes were smaller and thinner compared to those from the 24h steady solution as expected **(Figure 31)**. Giving time to the solution to sit with no sonication and turbulence forces, induces the precipitation of larger particles (submicron) leaving the smaller particles behind. We should mention that sonication in ethanol, did not change the morphology of the Ni_3ZnB_2 MAB particles, keeping the nano-layered microstructure (**Figure 33**).

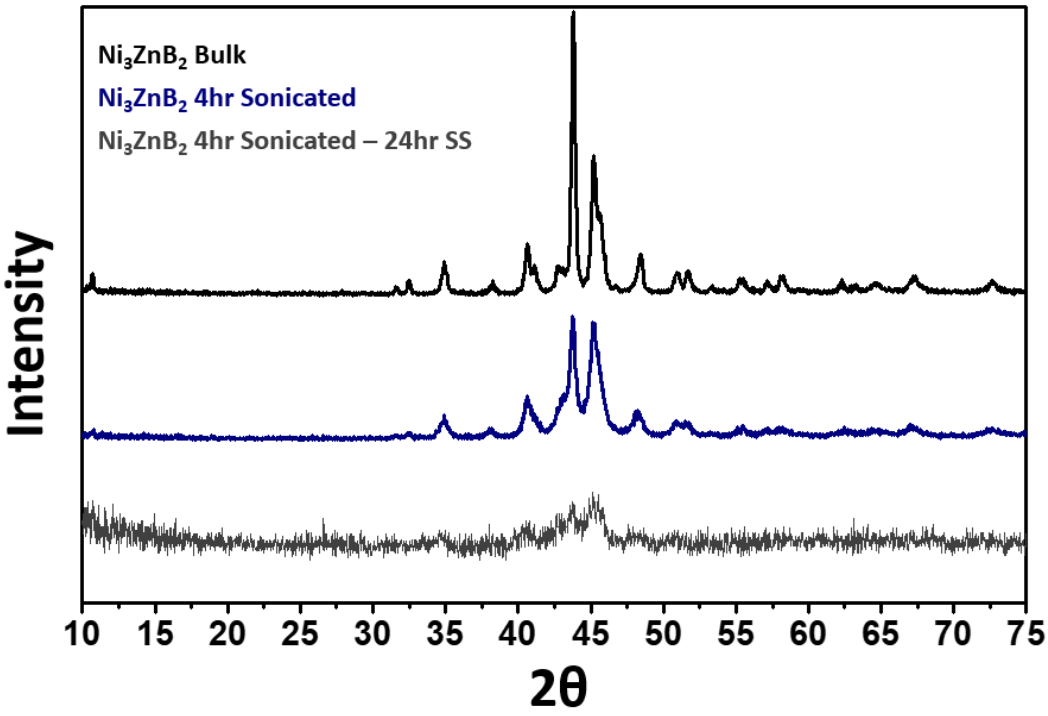

Figure 34. Powder X-ray diffraction patterns of Ni_3ZnB_2 before and after sonication in ethanol

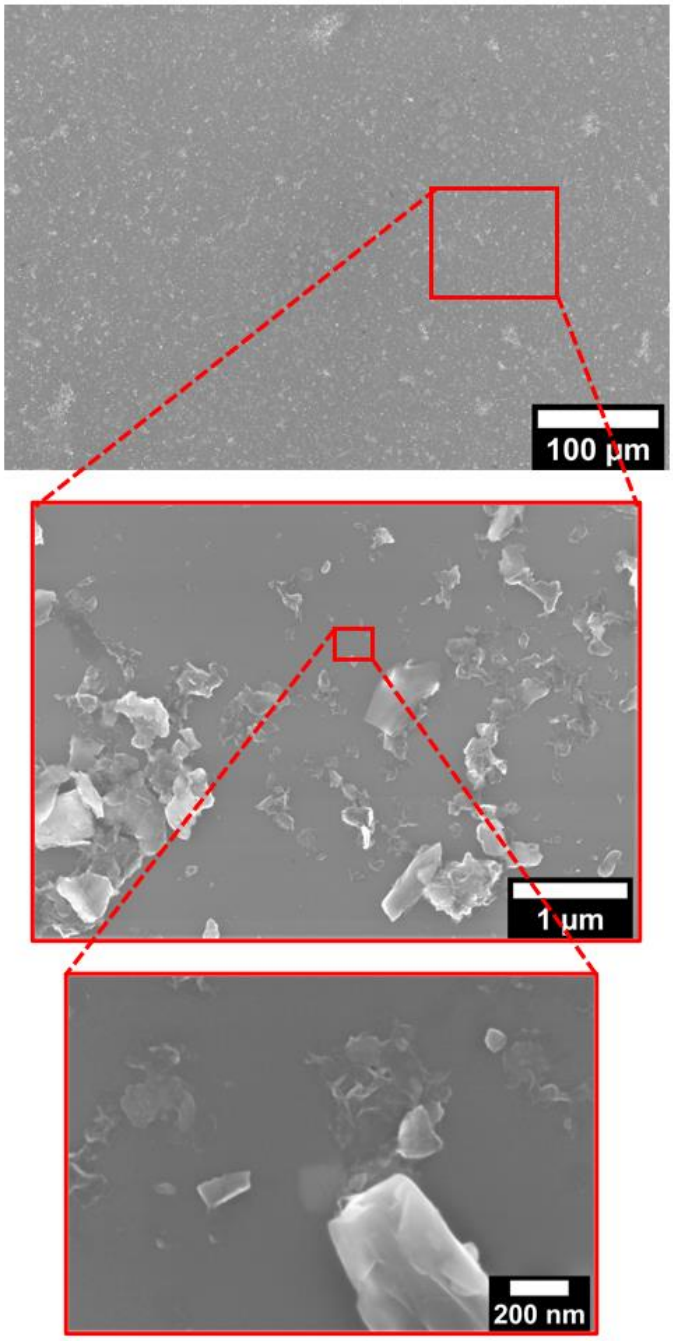

Figure 35. SEM images of Ni_3ZnB_2 sheets sonicated in ethanol for 4hr- drop-casted on Si/SiO_2 substrate after 24h

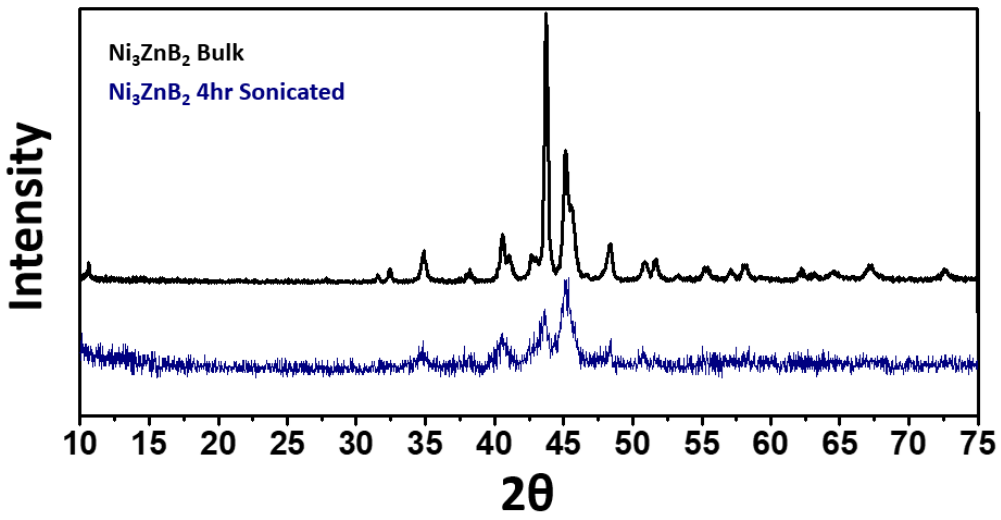

Figure 36. Powder X-ray diffraction patterns of Ni_3ZnB_2 before and after sonication in DI water

In another experiment, Ni_3ZnB_2 MAB exfoliation was studied in DI water and compared to ethanol. It was interestingly observed that water has a smaller yield of exfoliation compared to ethanol. The water sonication vial holds a more transparent color compared to ethanol (**Figure 30**) proving ethanol may be a more efficient solution for sonicating Ni_3ZnB_2. This finding corelates with sonication of other transition metal diborides in aqueous media. The PXRD for the collected particles 1hr after the sonication in water, did show a significant intensity decrease followed by broadening of the peaks, hinting at a great particle size decrease. However, no new peaks or shift was observed, demonstrating that upon sonication in water, no phase change has occurred to the MAB particles. Contrary to ethanol, most of the particles were precipitated after 24h, however the collected flake sample was not enough for PXRD measurement (~ yield 1.1%).

The sonicated MAB particles were drop-casted on a Si/SiO_2 wafer to study their morphology and particle size. Interestingly, it was observed that the morphology of the Ni_3ZnB_2 MAB particles changed upon sonication in water compared to ethanol. Thin folded sheets were observed

providing a fluffy microstructure covering most of the substrate surface (**Figure 35**). This morphology is similar to the MgB_2 processed and exfoliated in water.[124]

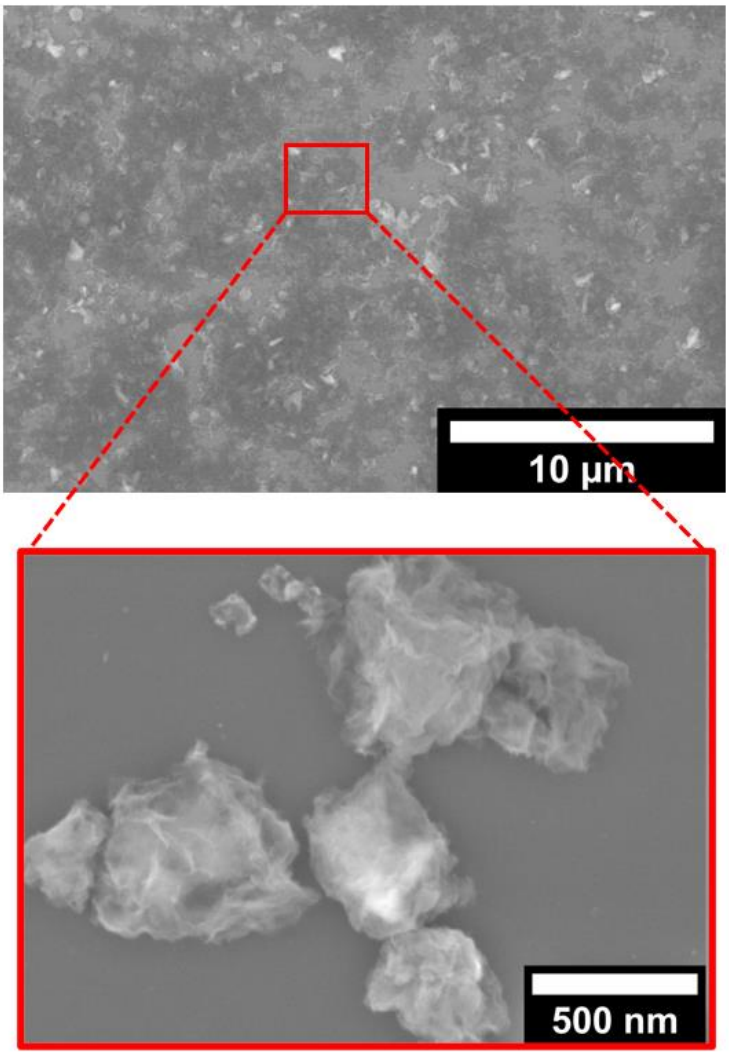

Figure 37. SEM images of Ni_3ZnB_2 sheets sonicated in water for 4hr and drop-casted on Si/SiO_2 substrate after 24h

5.3 Conclusion

In this study we have investigate the layered morphology of the nano-laminated Ni_3ZnB_2 MAB phase and its liquid phase exfoliation for the first time. We suggest, Ni_3ZnB_2, basal plane delamination as the main fracture mechanism for the obtained MAB nanosheets. Subsequently, we

studied the formation of Ni_3ZnB_2 nano flakes through sonicating the MAB particles in ethanol and DI water media. The obtained nano sheets were shown to retain its layered morphology and crystal structure based on SEM and PXRD analyses. Finally, it was observed that ethanol is a more efficient solution compared to water. However, thinner sheets were exfoliated in water. The demonstration of liquid phase exfoliation of Ni_3ZnB_2 may open doors for future MAB and layered transition metal borides applicable in additive manufacturing and 3D printing processes.

Chapter 6

Abundant Active Sites on Basal Plane and Edges of Layered vdW Fe_3GeTe_2 for Highly Efficient Hydrogen Evolution

In the final chapter of this dissertation, we focus on Fe_3GeTe_2 as a van der Waals layered compounds for hydrogen evolution. In the first step, the synthesized FGT compound was partially exfoliated via ultrasonication. Subsequently, the partially exfoliated layers were investigated for their hydrogen evolution (HER) properties. Finally, compacted electrodes of the FGT compound was fabricated and demonstrated as a highly efficient catalysts for hydrogen evolution. This work led to the discovery of basal plane and edge site HER activity of FGT for the first time. This chapter is adapted from the published manuscript:

DOI: 10.1021/acsmaterialslett.1c00048 - **Rezaie AA***, Lee E*, Luong D*, Yapo JA, Fokwa BP. ACS Materials Letters. 2021 Feb 22;3(4):313-9.

* A.A.R., E.L., and D.L. are co-first authors

6.1 Introduction

The development of clean and renewable energy is crucial in order to overcome the depletion of fossil fuels while meeting an increase in energy demand.[125, 126] Among all the renewable energy sources, hydrogen has been accepted as one of the most promising alternatives to fossil fuels due to its cleanliness, sustainability and high energy density.[127-129] Through water electrolysis, an environmental-friendly method, hydrogen can be produced to achieve sustainable energy production.[130-132] Currently, platinum-group metals and noble-metal compounds are considered the most efficient hydrogen evolution reaction (HER) electrocatalysts. However, high cost and scarcity of these precious metals impede large-scale utilization and commercialization.[90,

133] The development of a highly active and abundant electrocatalyst would overcome these difficulties, providing the necessary breakthrough for a sustainable and clean energy supply.

Van der Waals (vdW) layered materials have been known for several decades.[134] However, the interest in these materials has been renewed since the discovery of graphene as the first two-dimensional (2D) material.[3, 4] This and various other 2D materials beyond graphene have raised extensive interest in optical, electronic, and energy storage applications.[135-137] Due to intriguing properties, 2D materials are being explored as alternative electrocatalysts.[138-141] Most pristine vdW materials do not show electrochemical activity in their basal planes; thus to improve the activity of the basal plane various surface modifications such as defect engineering [142-144], interfacial engineering [145-147], and doping [148-150] are required. However, if the parent layered material demonstrates activity in the basal plane prior to surface modification, its electrochemical activity can be tremendously improved after further modifications. Consequently, recent research has been focused on the discovery of new basal-plane active vdW materials. Among all the vdW layered materials, Fe_3GeTe_2 (FGT), an itinerant ferromagnet with high stability and high Curie temperature (220 K), has attracted great interest recently in the field of spintronics. FGT has a hexagonal crystal symmetry with space group $P6_3/mmc$, consisting of a "Fe_3Ge" substructure sandwiched between two layers of Te atoms, which are weakly bonded by vdW forces as seen in **Figure 36e.**[151, 152] Very recently, FGT was suggested as a potential electrocatalyst candidate for the oxygen-evolution reaction (OER) and other gas adsorption reactions (CO, NO, etc.).[141, 153] However, no theoretical or experimental work has proposed FGT as an active material for HER, to the best of our knowledge. Herein, we report on the experimental and theoretical investigations of the HER activity of FGT for the first time. We have investigated FGT's electrochemical activity in three different forms: bulk, partially exfoliated layers (sonicated), and densified layers. We found that FGT is highly active in bulk form already, a finding confirmed by

density functional theory (DFT) calculations. Furthermore, the activity further increases with exfoliation and even more after densification.

6.2 Results and Discussion

The FGT sample was synthesized through a direct solid-state reaction according to previous reports. The sample was investigated by powder X-ray diffraction (PXRD) for phase and crystallinity determination, via energy dispersive X-ray spectroscopy (EDS) for elemental analysis and through scanning electron microscopy (SEM) for particle size and morphology determination. According to the PXRD pattern (**Figure 36b**), all peaks matched those reported for FGT, proving a single-phase synthesis and EDS mapping showed the presence of all three elements as well as their homogeneous distribution (**Figure 36f**). However, some intensity mismatches were observed in the PXRD pattern for the *(00l)* peaks, due to the preferred orientation along the c-axis as expected for flat, thin crystals (**Figure 36f**).

To increase the amount of exposed basal planes, the FGT sample was crushed, and the resulting powder was dispersed in ethanol and ultrasonicated in a vial which was immersed in an ice-water bath for two hours. Ultrasonication of the FGT powder resulted in smaller particles (**Figure 37**). In addition, PXRD shows an intensity increase for the (002) peak (**Figure 36c**), indicating abundance of exposed (002) layers and conforming partial exfoliation of the bulk crystals. Interestingly, the (106) peak has become one of the most prevalent intensities, indicating exposure of edges through layer breaking.

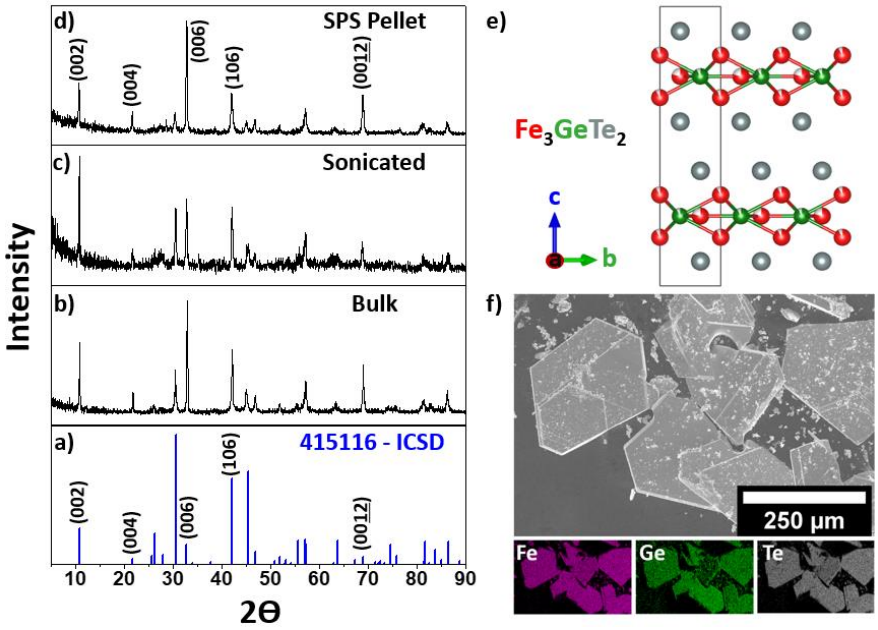

Figure 38. Powder X-ray diffraction patterns of FGT: (a) calculated, (b) FGT bulk, (c) sonicated FGT, and (d) SPS pellet. (e) Crystal structure and (f) SEM images and EDS mappings of as synthesized FGT crystals.

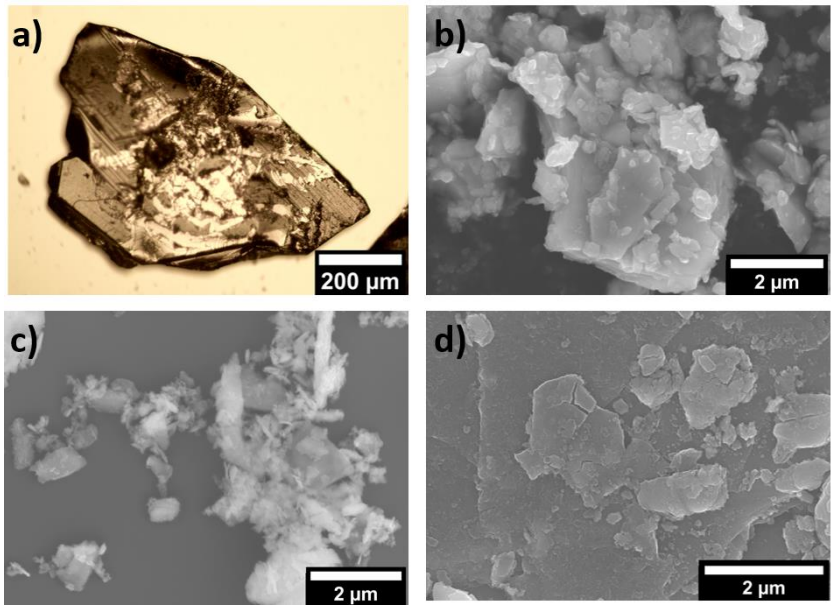

Figure 39. Micrographs of FGT a) Optical image of bulk crystal – b-d) SEM images of as-synthesized powder, after sonication, and SPS pellet, respectively

The surface chemical composition and the core-level binding energy of the bulk and sonicated FGT were investigated by X-ray photoelectron spectroscopy (XPS). **Figure 38** and **Table 5** show the oxidation states of the Fe 2p, Ge 3d, and Te 3d species on the analyzed surfaces. As shown in **Figure 38a**, the high-resolution Fe 2p spectrum is deconvoluted into Fe $2p_{1/2}$ and Fe $2P_{3/2}$: The two peaks at 706.6 eV/719.8 eV originate from the metallic iron (Fe^0in FGT). The two other doublets at 710.9 eV and 724.6 eV (with 713.2 and 726.21 eV satellites) [154-157] can be ascribed to Fe^{3+} from the surface oxide layer. The Ge 3d spectrum (**Figure 38b**) is deconvoluted into Ge $3d_{3/2}$ and Ge $3d_{5/2}$, with the peaks at 29.3/29.8 eV assigned to metallic germanium (Ge^0 in FGT), while those at 31.8 eV (Ge^{2+}) and 32.4 eV (Ge^{4+}) correspond to germanium oxide peaks.[158-160] Finally, the Te 3d spectrum (**Figure 38c**) is deconvoluted into Te $3d_{3/2}$ and Te $3d_{5/2}$, with the peaks at 572.9/583.3 eV ascribed to metallic tellurium (Te^0 in FGT) and those at 576.4/586.8 eV assigned to Te^{4+}.[161, 162] Comparing the non-oxides peaks (Fe^0, Ge^0, and Te^0) to each other in both samples (bulk and sonicated), it is obvious that Te^0 is by far the most abundant on the surface, an indication of a Te-terminated basal plane in FGT, as expected for this Te-terminated vdW atomic structure. The oxide peaks in all the species reveal that air-exposed surface atoms of FGT have been oxidized. However, this oxide layer is likely very thin because the FGT peaks (Fe^0, Ge^0, and Te^0) are still clearly detectable by XPS. Sonication diminishes the FGT's peak intensities, thereby increasing the amount of surface oxides because more surface area is exposed to oxygen as the particles become smaller. These surface oxides may affect the HER activity of FGT; however, our density functional theory (DFT) calculations show that FGT is already an active HER electrocatalyst on its own. Nevertheless, the effect of the oxides on FGT's HER activity warrants further investigations in the future.

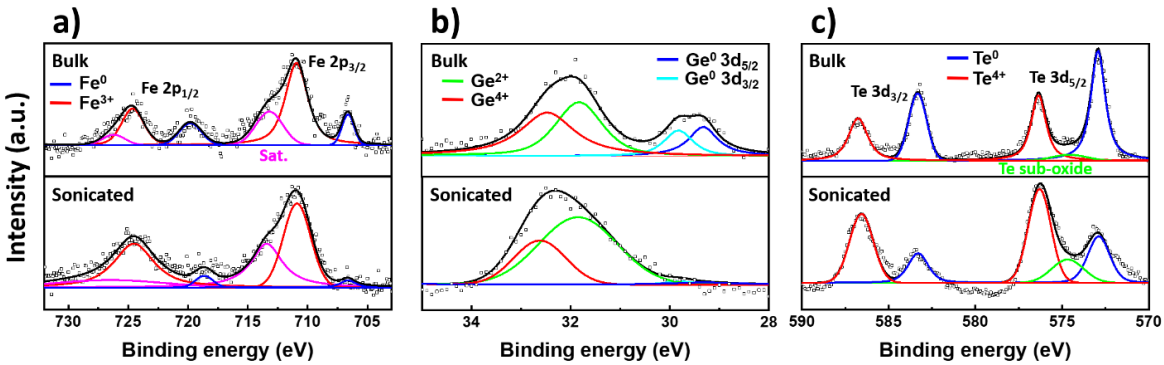

Figure 40. X-ray photoelectron spectroscopy spectra of (a) Fe 2p, (b) Ge 3d, and (c) Te 3d for bulk and sonicated FGT samples. Experimental and fitting data are indicated as (□) and solid lines, respectively.

Table 5. XPS peak position and full width at half maximum (FWHM) parameters for Fe 2p, Ge 3d, and Te 2d of FGT

	Species	Peak position (eV)	FWHM (eV)
Bulk sample	Fe^{0}	706.6, 719.8	1.2, 2.2
	Fe^{3+}	710.9, 724.6	2.22, 2.19
	Satellite	713.2, 726.21	2.66, 2.23
	Ge^{0}	29.3, 29.8	0.69, 0.68
	Ge^{2+}	31.8	1.11
	Ge^{4+}	32.4	1.3
	Te^{0}	572.9, 583.3	0.98, 1.21
	Te^{4+}	576.4, 586.8	1.01, 1.29
Sonicated sample	Fe^{0}	706.6, 718.6	1.49, 1.72
	Fe^{3+}	710.9, 724.5	2.69, 3.94
	Satellite	713.42, 726.5	3.12, 10.7
	Ge^{0}	29.8	1
	Ge^{2+}	31.8	1.86
	Ge^{4+}	32.6	1.23
	Te^{0}	572.9, 583.3	1.49, 1.36
	Te^{4+}	576.3, 586.6	1.54, 1.61
Sonicated sample after HER	Fe^{0}	706.6, 718.5	0.9, 3.41
	Fe^{3+}	710.7, 724.1	3.4, 6
	Satellite	713.2, 727.6	5.97, 16.6
	Ge^{0}	29.8	1
	Ge^{2+}	31.3	1.55
	Ge^{4+}	32.4	1.54
	Te^{0}	573.0, 583.3	1.96, 1.42
	Te^{4+}	576.5, 587.0	1.73, 1.86

The HER activities of the bulk and sonicated FGT samples were examined in 1 M KOH solution and their electrodes were prepared via a drop-cast method. The linear sweep voltammetry (LSV) curve of the bulk FGT powder exhibits an overpotential of $\eta_{10} = -0.337$ V at 10 mA/cm^2 (**Figure 39a**). In comparison, bulk FGT is far better than the most popular layered materials studied as HER catalysts; bulk hexagonal 2H-MoS_2 ($\eta_{10} = -0.83$ V) [95] and 2H-$MoTe_2$ ($\eta_{10} = -0.65$ V)[163], whose active sites are limited solely to the edges. To improve their activity, the basal plane of these materials is usually activated by different surface modifications, the best value ($\eta_{10} = -0.31$ V) being recorded for the 2H-MoS_2 directly grown on carbon cloth. Interestingly, puckering the chalcogenide layer has proven to be another successful way to activate the basal plane. For example, the basal planes in 3R-MoS_2 [95] and 1T'-$MoTe_2$ [163] are active showing improved overpotentials of $\eta_{10} = -0.52$ V and $\eta_{10} = -0.34$ V, respectively. FGT has an overpotential comparable to 1T'-$MoTe_2$, hinting at its basal plane activity even though it has an undistorted hexagonal crystal structure with honeycomb Te layers. As demonstrated by PXRD analysis, the bulk FGT sample shows preferred orientation along the *c* axis [basal plane, (00*l*) reflections], a further indication that the observed activity might be related to the exposed basal plane. Furthermore, XPS analysis shows that Te dominates the surface, a further hint that the Te basal plane is exposed. Indeed, our DFT calculations show that the flat Te layer in FGT is as active as the puckered Te layer in 1T'-$MoTe_2$.

To confirm and improve this result, we have investigated a sonicated FGT sample, which has more basal planes exposed than the bulk, as shown by PXRD. However, the sonication can also break the layers and provide edge sites which can further impact activity; for example, the PXRD (**Figure 36c**) shows that the (106) layers are among the most abundant in the sample. Compared to the bulk powder, the sonicated sample shows a significant enhancement (33%) in HER activity with an overpotential of $\eta_{10} = -0.222$ V. To understand this result, we have estimated the available

surface-active sites using the electrochemical active surface area (ECSA) method. ESCA was estimated from the electrochemical double-layer capacitance (C_{dl}), the larger the C_{dl} value the more active sites are present.[164] **Figure 40** shows that the C_{dl} value (22.9 mF/cm^2) of the sonicated powder is larger than that of the bulk powder (16.2 mF/cm^2), confirming that the sonicated sample has more active sites than the bulk. There are two reasons for the increased activity: The exfoliation of the FGT crystals which exposes more basal planes (**Figure 36c**) and the decrease in particle size (**Figure 37**) which exposes more edge sites. However, the increased formation of oxide layers on the surface after sonication could also play a role.

Improving the HER activity of vdW transition metal dichalcogenides (TMDs) is currently one of the most attractive research areas, where defect engineering is being used for activating the inactive basal planes of hexagonal TMDs. For monoclinic 1T'-$MoTe_2$, which has an active basal plane, a different strategy was recently employed to boost its HER activity: In fact, its catalytic performance was improved dramatically when the electrode was held at a cathodic bias. As a result, the overpotential required to maintain a current density of 10 mA cm^{-2} improved from −0.320 V to −0.178 V.[165] This is an extraordinary result which showcases the ease with which the HER activity of basal-plane active materials can be improved. During our recent studies of another group of basal-plane active materials (transition metal diborides), we discovered that their HER activity can be drastically improved by efficiently covering the electrode, thus taking advantage of the basal-plane activity.[104, 166, 167] We have applied this strategy to further improve the activity of FGT. The sonicated FGT sample was compressed into a pellet through spark plasma sintering (SPS) at room temperature to achieve a densified disk. As shown in **Figure 41c,** the electrode surface is denser than the other electrodes. This type of electrode exposes more basal planes compared to the drop-cast method; however, the sonication also breaks the layers and provides edge sites which can further impact activity. As shown in **Figure 41c,** the disk-type electrode

provides a homogenous coverage of the FGT particles if compared to the other electrodes (**Figures 41 a & b**). The PXRD pattern of the SPS pellet (**Figure 36d**) shows an intensity increase of the (*00l*) peaks pointing toward a preferred orientation and the presence of more basal planes. Interestingly, this PXRD pattern is almost identical to that recorded for a single crystal of FGT (**Figure 42**), thus hinting at a nearly single-crystal-like layer arrangement of the FGT particles in the SPS pellet. However, as pointed out above the (106) peak remains one of the dominant intensities and thus may have an impact on activity (see theory section below). This condensed, highly oriented (single-crystal-like) electrode dramatically improves all electrochemical parameters of FGT. The obtained overpotential ($\eta_{10} = -0.105$ V) is not only more than twice lower than that of the sonicated sample ($\eta_{10} = -0.222$ V), but it is also the lowest value reported so far for all bulk TMDs electrocatalysts, to the best of our knowledge. Furthermore, the path for the electrodes to transfer electrons from the electrode' substrate (in this work, it is a Cu plate) to the active sites is hugely facilitated by the better electrode coverage of the densified electrode, leading to a more than twofold increase in the C_{dl} value (52.7 mF/cm^2) if compared to that of the sonicated sample (22.9 mF/cm^2), thus confirming the overpotential findings. Interlayer electron transfer is the dominant mechanism for HER activity in layered materials [110], so by reducing the distance between the particles (densification), this makes it easier for electrons to traverse through the layered particles. This is further supported by the EIS data in **Figure 39c and Table 6**. The charge transfer resistance (R_{ct}) derived from the Nyquist plot can be fitted using an equivalent circuit model consisting of a series resistance (R_s, mainly the solution resistance) and a constant phase element (CPE). The SPS electrode has a much smaller R_{ct} (9.71 Ω) than the sonicated electrode (24.6 Ω), supporting the idea that electrons will move faster in the former and thus boosting its charge transfer rate during HER.

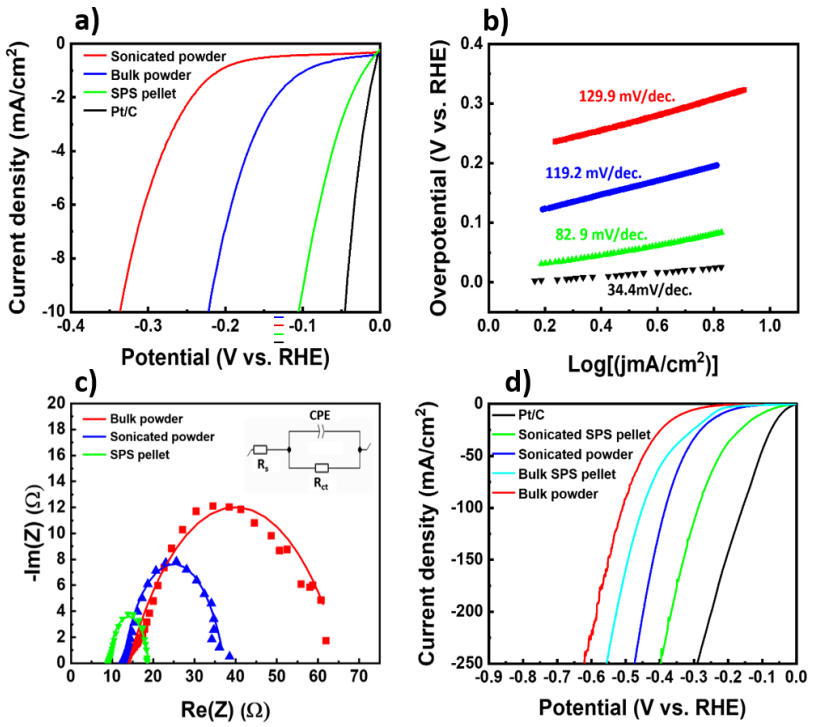

Figure 41. a) Polarization curves of FGT (for various electrode types) and Pt/C. The data is recorded in 1 M KOH at a scan rate of 5 mV/s with iR-correction. b) Tafel plots obtained using the polarization curves in "a". c) Electrochemical impedance spectroscopy (EIS) Nyquist plots of various FGT electrodes in 1 M KOH. The points represent the experimental data and the lines are the fitting data. d) Polarization curves of different FGT electrodes at high current density in 1 M KOH at a scan rate of 5 mV/s with iR-correction.

Table 6. Fitted EIS data for different FGT electrodes

Electrode type	R_s [Ohm]	R_{ct} [Ohm]	CPE [F s^{a-1}]	a
Bulk powder	14.0	52.0	4.02 e^{-3}	0.551
Sonicated powder	12.6	24.6	4.06 e^{-3}	0.708
SPS pellet	9.16	9.71	0.210 e^{-2}	0.813

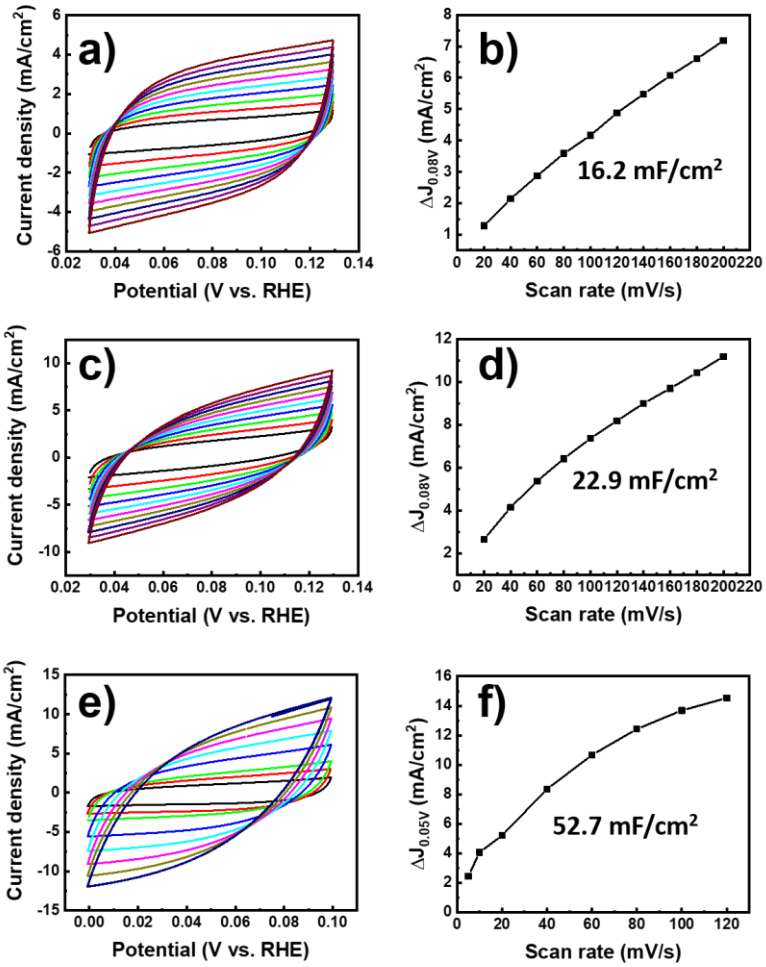

Figure 42. Cyclic voltammetry profiles and linear fitting of the capacitive currents versus scan rates obtained from cyclic voltammetry tests at 0.05 V vs. RHE to estimate Cdl for (a, b) bulk powder, (c, d) sonicated powder, and (e, f) SPS pellet type electrode in 1M KOH

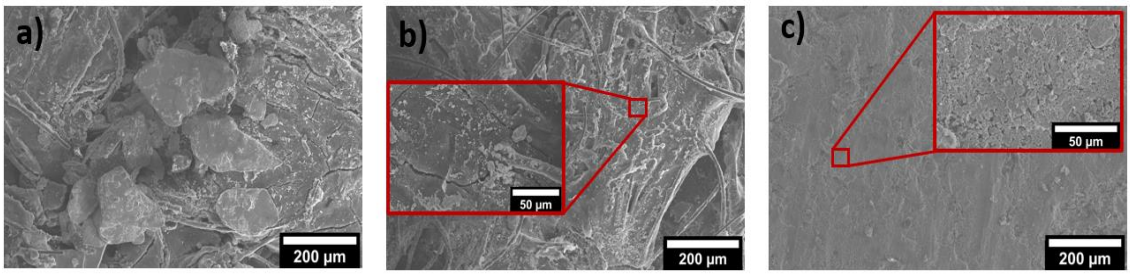

Figure 43. SEM micrographs of the prepared FGT electrodes of a) as-synthesized sample, b) sonicated sample, and c) SPS pellet.

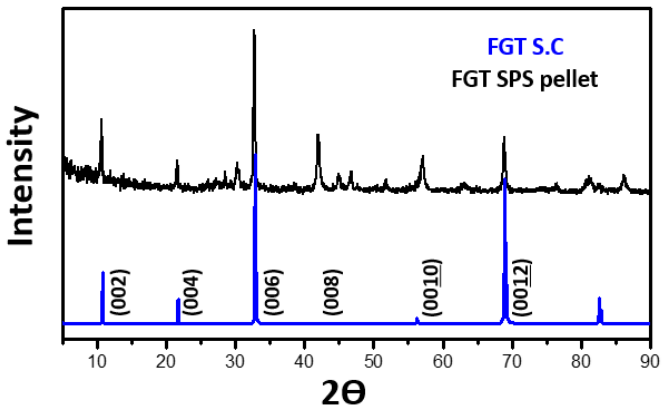

Figure 44. X-ray diffraction of the FGT SPS pellet compared to that of an FGT single crystal (S.C)

The Tafel slope is an inherent catalyst property regulated by the rate-determining step of HER, with a small slope being desirable to drive a large catalytic current density at low overpotential. From the Tafel plots (**Figure 39b**), the bulk powder and the sonicated powder display a slope of 134.6 mV/dec and 125.1 mV/dec respectively. The SPS pellet demonstrates a superior HER activity with the lowest Tafel slope (97.3 mV/dec), indicating a much more efficient HER with faster kinetics versus the other two electrodes. Additionally, the Tafel slope values of the bulk powder and the sonicated powder near 120 mV/dec indicate that the Volmer reaction strongly controls the HER process,[111, 168] whereas the SPS pellet shows the Tafel slope falling in between of Volmer reaction (Tafel slope ~120 mV/dec) and Heyrovsky reaction (Tafel slope ~ 40 mV/dec) due to the complexity of the reaction observed in highly active bulk catalysts.[104] Continuous cyclic voltammetry (CV) was employed to evaluate the stability of FGT (**Figure 43**). All the electrodes reveal good stability after 3000 cycles. Furthermore, the catalysts were analyzed through a chronoamperometric test (**Figure 43 b, d, and f**). At a fixed overpotential, all the electrodes yielded a stable current density of about 10 mA/cm^2 for 24 h, further consolidating their high durability.

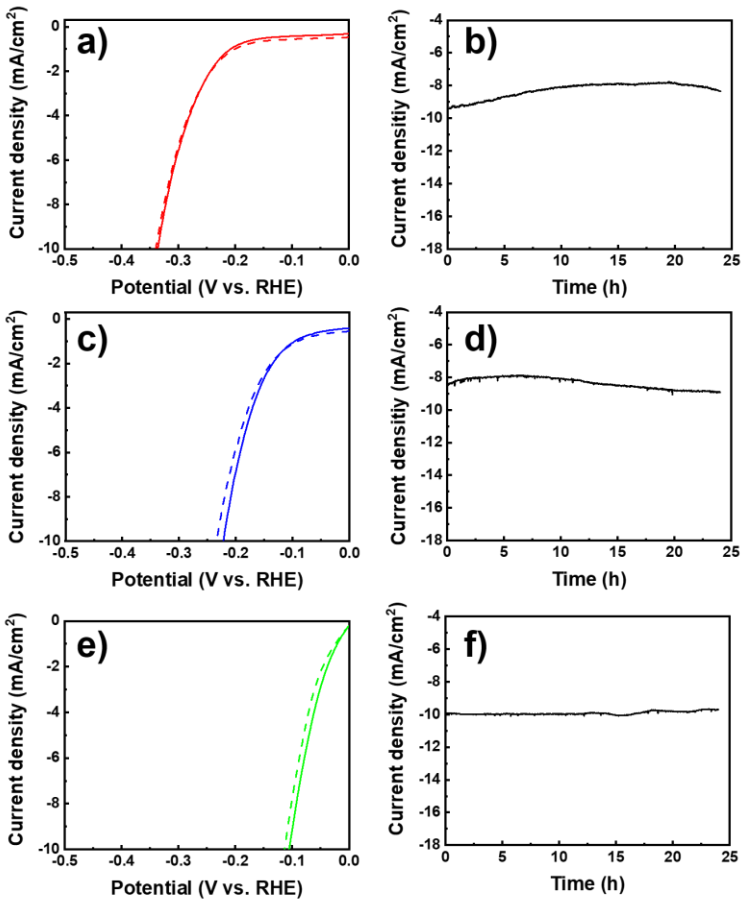

Figure 45. HER stability measurement of a) bulk powder, c) sonicated powder, and e) SPS pellet FGT electrode before and after 3000 cycles with a scan rate of 100 mV s-1 1 M KOH, Chronoamperometry curve of b) bulk powder, d) sonicated powder, and f) SPS pellet FGT

First-principles DFT calculations were performed to study the active sites of FGT by considering different H-adsorption sites on two different layers, the basal plane (002) and an edge plane (106). For the (002) all tellurium layer the following sites were considered: (1) on top (Top) of a Te atom, (2) on a hollow site (Hol-1) above an Fe atom and (3) on a hollow site (Hol-2) above a Ge atom (**Figure 44b**). For the mixed tellurium/iron (106) layer the following sites were considered: (4) on top (Top-1) of one Fe atom, (5) on top of a separate Fe atom (Top-2), and (6) on top of a Te atom (Top-3) (**Figure 44c)**. The binding energy (ΔE_H) and the Gibbs free energy (ΔG_H)

for H-adsorption were evaluated (see supporting information for more details) for all these sites and compared with those reported for 1T'-$MoTe_2$. As shown in **Figure 44a**, the calculated ΔG_H values for the basal (002) layer of FGT are 1.30 eV, 1.38 eV, and 1.98 eV for the Top, Hol-1 and Ho1-2 sites, respectively, while for the (106) layer the obtained ΔG_H values are -0.45 eV, -0.26 eV, and 0.21 eV for the Top-1, Top-2 and Top-3, respectively. Bulk $MoTe_2$ is known for high basal plane activity in its monoclinic polymorph 1T'-$MoTe_2$,[163, 169] thus it is the perfect candidate for comparison. The basal plane of this material also contains many active sites on its distorted tellurium layer, two of which have the best ΔG_H values; 0.86 eV and 1.72 eV for H-adsorption on top of the lower Te and on top of the higher Te, respectively.[169] Comparing the basal plane results of the two phases, it is quite astonishing that the top sites (most active sites for the FGT basal plane) in both compounds have almost the exact ΔG_H values if the average (1.29 eV) is used in the case of 1T'-$MoTe_2$, thus predicting similar HER activity for the basal plane in these two compounds. Indeed, the experimental HER activity measurements presented above for bulk FGT show nearly the same overpotential (η_{10}= −0.337 V, in KOH) as bulk 1T'-$MoTe_2$ (η_{10}= −0.34 V, in H_2SO_4). To the best of our knowledge, FGT is the first HER electrocatalyst found so far in the class of hexagonal vdW materials with an active undistorted hexagonal Te layer, since the hexagonal polymorph of $MoTe_2$ was found not to be competitive for HER in the bulk. Furthermore, the results for the (106) layer suggests the presence of an even more active layer for FGT with ΔG_H values that are much closer to zero (from -0.45 to 0.21 eV) in comparison to those calculated for the basal planes of FGT and 1T'-$MoTe_2$. This result supports the far better HER activity found for the sonicated sample if compared to the bulk, because smaller particles expose more edge sites which are more active. However, the XPS results showed that a thin oxide layer is present on the surface of these materials, suggesting that the real active sites may be hybrid layers composed of the thin oxide layer and the different active FGT layers underneath. The hybrid model is further supported

by the fact that a further oxidation (**Figure 45**) of the FGT sample through ball-milling has resulted in a significantly bad catalyst despite obvious reduction of particle size according to PXRD.

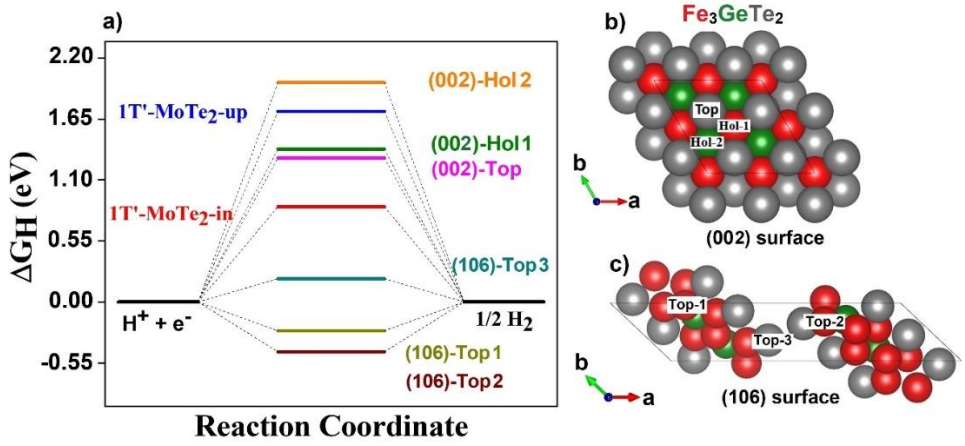

Figure 46. a) The Gibbs free energy (ΔGH) of H-adsorption on several active sites of FGT and 1T'-MoTe2 from.52 b) FGT superstructure models generated for (002) and (106) surfaces with the top and hollow sites indicated.

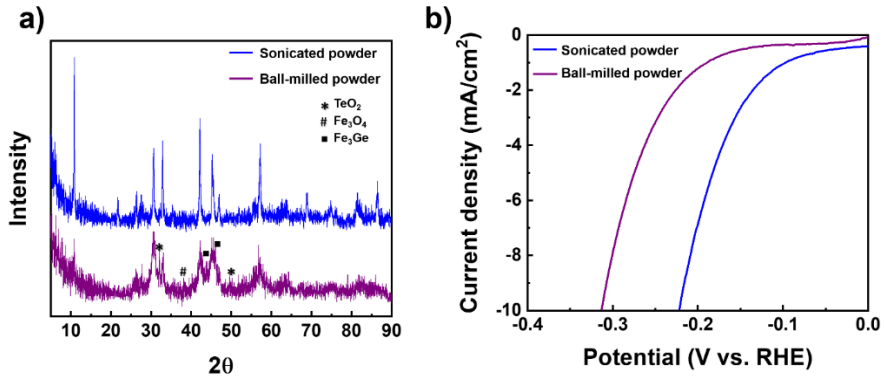

Figure 47. X-ray diffraction of the ball-milled FGT sample showing some oxide peaks (a) and polarization curves of the sonicated and ball-milled FGT samples in 1 M KOH at a scan rate of 5 mV/s with iR-correction.

6.3 Conclusion

In conclusion, FGT has been successfully synthesized by a solid-state reaction and the sample was characterized by PXRD, EDS and SEM analyses. In addition, its electrochemical properties were studied experimentally and theoretically. Three types of electrodes (bulk powder,

sonicated powder, and SPS-densified pellet) were prepared to explore the HER activity. The results indicated that the HER activity of the sonicated FGT, which exposes more basal and edge planes, is higher than that of the bulk. Moreover, the SPS pellet electrode, which is the densest and whose PXRD showed single-crystal-like preferred orientation along the *c* direction but also the presence of some edge planes, requires the smallest overpotential ($\eta_{10} = -0.105$ V) among all bulk TMDs reported so far. All the electrodes have excellent long-term stability and durability, displaying no significant HER activity loss after 3000 cycles and 24 hours of operation in an alkaline electrolyte. To understand the excellent HER activity of FGT, DFT calculations were performed. The calculated ΔG_H values of the hexagonal basal plane Te layer was found to be nearly equal to that of the puckered Te layer in monoclinic $MoTe_2$ (1T'-$MoTe_2$), supporting the basal plane activity of FGT. Furthermore, the calculated ΔG_H values of another prevalent (106) layer (edge layer) are even closer to zero, thus supporting the increased in activity with particle size reduction, which favors increased edge sites. Furthermore, the presence of a thin oxide layer on top of the active FGT layers as found by XPS suggests that the real active surface is likely a hybrid FGT/oxide layer. This study introduces FGT as a highly HER active hexagonal vdW material with active basal plane and edge sites, thus paving the way for further studies of related iron-based vdW materials, their composites, and their surface functionalization as high-performing electrocatalysts.

Acknowledgements

This work was supported by the startup fund to BPTF at UC Riverside and a partial support from the National Science Foundation Career award to BPTF (no. DMR-1654780). The authors would like to thank Suveen N. Mathaudhu and Steven Herzberg for their advice and access to the SPS machine. The San Diego Supercomputer Center (SDSC) is gratefully acknowledged for providing

computing resources. The XPS data were collected with an instrument acquired through the NSF MRI program (DMR-0958796). This work has been done and discussed equally with me, Eunsoo Lee and Diana Luong my lab mates. I would like to thank them for their time and consult in this project. I would also like to thank Johan Yapo for providing the DFT calculation.

Chapter 7

Conclusion

The research presented in this dissertation studies the synthesis and characterization of layered compounds focusing mainly on MAB phases, investigates their possible exfoliation toward 2D and quasi 2D sheets and finally introduces them as potential materials for energy applications such as Li-ion batteries and hydrogen evolution.

In the first part of this dissertation, $Ni_{(n+1)}ZnB_n$ (n=1, 2) nano laminated MAB phases were synthesized through a two-step melt solidification technique leading to formation of highly pure, preferred oriented MAB sheets. Studying these MAB phases for possible chemical exfoliation in HCl, led to the formation of high surface area MAB particles with modified surface species which led to the discovery of the first MAB phases with potential as Li-ion battery materials (Chapter 3). Subsequently, the proposed MAB phases were studied for their hydrogen evolution properties. Both Ni_2ZnB and Ni_3ZnB_2 were investigated for their basal plane activity via investigating highly densified pressed pellets of these MAB phases. Although bulk Ni_2ZnB and Ni_3ZnB_2 already had a comparable overpotential compared to all other MAB / MAX phases, the their pressed electrodes had even better HER performance showing low overpotentials to drive a 10 mA cm^{-2} current density of -0.17 V and -0.14 V for Ni_2ZnB and Ni_3ZnB_2, respectively. Finally, DFT free energy calculations showed that the nickel basal plane is more active than the zinc basal plane, supporting the experimental results (chapter 4). While studying and characterizing the synthesized layered $Ni_{(n+1)}ZnB_n$ MAB phases, it was observed that they tend to delaminate and break along their basal plane, hinting at the possibility of forming quasi-2D sheets through consistent and more severe forces such as liquid phase exfoliation. It was observed that Ni_3ZnB_2 partially exfoliates in both ethanol and water forming MAB nano-sheets (chapter 5). In the final section of this thesis, the

hexagonal vdW layered Fe_3GeTe_2 was demonstrated as basal plane and edge site active HER catalyst. The FGT layered compounds was partially exfoliated through ultrasonication. Exposing more of the basal plane and edge sites improved the overpotential. Finally, like the MAB electrodes, pressed pellets of the FGT were fabricated. These densified electrodes showed an impressive overpotential of -0.105 V to drive a current density of 10 mA/cm^2. These results demonstrated the high basal plane and edge sites HER activity of FGT.

References:

[1] J.A. Wilson, A. Yoffe, The transition metal dichalcogenides discussion and interpretation of the observed optical, electrical and structural properties, Advances in Physics, 18 (1969) 193-335.

[2] V. Nicolosi, M. Chhowalla, M.G. Kanatzidis, M.S. Strano, J.N. Coleman, Liquid exfoliation of layered materials, Science, 340 (2013) 1226419.

[3] K.S. Novoselov, A.K. Geim, S.V. Morozov, D. Jiang, Y. Zhang, S.V. Dubonos, I.V. Grigorieva, A.A. Firsov, Electric field effect in atomically thin carbon films, Science, 306 (2004) 666-669.

[4] A.C. Neto, F. Guinea, N.M. Peres, K.S. Novoselov, A.K. Geim, The electronic properties of graphene, Reviews of Modern Physics, 81 (2009) 109.

[5] L. Song, L. Ci, H. Lu, P.B. Sorokin, C. Jin, J. Ni, A.G. Kvashnin, D.G. Kvashnin, J. Lou, B.I. Yakobson, Large scale growth and characterization of atomic hexagonal boron nitride layers, Nano letters, 10 (2010) 3209-3215.

[6] Q.H. Wang, K. Kalantar-Zadeh, A. Kis, J.N. Coleman, M.S. Strano, Electronics and optoelectronics of two-dimensional transition metal dichalcogenides, Nature Nanotechnology, 7 (2012) 699.

[7] M. Naguib, M. Kurtoglu, V. Presser, J. Lu, J. Niu, M. Heon, L. Hultman, Y. Gogotsi, M.W. Barsoum, Two-dimensional nanocrystals produced by exfoliation of Ti3AlC2, Advanced Materials, 23 (2011) 4248-4253.

[8] M. Ade, H. Hillebrecht, Ternary borides Cr2AlB2, Cr3AlB4, and Cr4AlB6: The first members of the series (CrB2) n CrAl with n= 1, 2, 3 and a unifying concept for ternary borides as MAB-phases, Inorganic Chemistry, 54 (2015) 6122-6135.

[9] S. Kota, E. Zapata-Solvas, A. Ly, J. Lu, O. Elkassabany, A. Huon, W.E. Lee, L. Hultman, S.J. May, M.W. Barsoum, Synthesis and characterization of an alumina forming nanolaminated boride: MoAlB, Scientific Reports, 6 (2016) 26475.

[10] M. Barsoum, T. El-Raghy, Synthesis and characterization of a remarkable ceramic, Ti3SiC2, Journal of American Ceramic Society, 79 (1996) 1953-1956.

[11] W. Jeitschko, H.t. Nowotny, F. Benesovsky, Carbides of formula T2MC, Journal of the Less Common Metals, 7 (1964) 133-138.

[12] J. Schuster, H. Nowotny, C. Vaccaro, The ternary systems: CrAlC, VAlC, and TiAlC and the behavior of H-phases (M2AlC), Journal of Solid State Chemistry, 32 (1980) 213-219.

[13] M. Barsoum, T. El-Raghy, Room-temperature ductile carbides, Metallurgical and Materials Transactions A, 30 (1999) 363-369.

[14] M. Barsoum, T. El-Raghy, M. Ali, Processing and characterization of Ti 2 AlC, Ti 2 AlN, and Ti 2 AlC 0.5 N 0.5, Metallurgical and Materials Transactions A, 31 (2000) 1857-1865.

[15] M.W. Barsoum, T. El-Raghy, The MAX phases: Unique new carbide and nitride materials: Ternary ceramics turn out to be surprisingly soft and machinable, yet also heat-tolerant, strong and lightweight, American Scientist, 89 (2001) 334-343.

[16] H. Högberg, L. Hultman, J. Emmerlich, T. Joelsson, P. Eklund, J.M. Molina-Aldareguia, J.-P. Palmquist, O. Wilhelmsson, U. Jansson, Growth and characterization of MAX-phase thin films, Surface and Coatings Technology, 193 (2005) 6-10.

[17] M.W. Barsoum, MAX phases: properties of machinable ternary carbides and nitrides, John Wiley & Sons 2013.

[18] P. Eklund, M. Beckers, U. Jansson, H. Högberg, L. Hultman, The Mn+ 1AXn phases: Materials science and thin-film processing, Thin Solid Films, 518 (2010) 1851-1878.

[19] T. El-Raghy, M.W. Barsoum, A. Zavaliangos, S.R. Kalidindi, Processing and mechanical properties of Ti3SiC2: II, effect of grain size and deformation temperature, Journal of American Ceramic Society, 82 (1999) 2855-2860.

[20] S.B. Li, H.X. Zhai, Synthesis and reaction mechanism of Ti3SiC2 by mechanical alloying of elemental Ti, Si, and C powders, Journal of American Ceramic Society, 88 (2005) 2092-2098.

[21] W. Zhou, B. Mei, J. Zhu, X. Hong, Rapid synthesis of Ti2AlC by spark plasma sintering technique, Materials Letters, 59 (2005) 131-134.

[22] E. Pickering, W.J. Lackey, S. Crain, CVD of Ti3SiC2, Chemical Vapor Deposition, 6 (2000) 289-295.

[23] T. Goto, T. Hirai, Chemically vapor deposited Ti3SiC2, Materials Research Bulletin, 22 (1987) 1195-1201.

[24] M.W. Barsoum, M. Radovic, Elastic and mechanical properties of the MAX phases, Annual Review of Materials Research, 41 (2011) 195-227.

[25] J. Xu, M.-Q. Zhao, Y. Wang, W. Yao, C. Chen, B. Anasori, A. Sarycheva, C.E. Ren, T. Mathis, L. Gomes, Demonstration of Li-ion capacity of MAX phases, ACS Energy Letters, 1 (2016) 1094-1099.

[26] S. Zhao, Y. Dall'Agnese, X. Chu, X. Zhao, Y. Gogotsi, Y. Gao, Electrochemical Interaction of Sn-Containing MAX Phase (Nb2SnC) with Li-Ions, ACS Energy Letters, 4 (2019) 2452-2457.

[27] G. Deysher, C.E. Shuck, K. Hantanasirisakul, N.C. Frey, A.C. Foucher, K. Maleski, A. Sarycheva, V.B. Shenoy, E.A. Stach, B. Anasori, Synthesis of Mo4VAlC4 MAX Phase and Two-Dimensional Mo4VC4 MXene with 5 Atomic Layers of Transition Metals, ACS Nano, 14 (2019) 2014-217.

[28] M. Naguib, V.N. Mochalin, M.W. Barsoum, Y. Gogotsi, 25th anniversary article: MXenes: a new family of two-dimensional materials, Advanced Materials, 26 (2014) 992-1005.

[29] M. Alhabeb, K. Maleski, B. Anasori, P. Lelyukh, L. Clark, S. Sin, Y. Gogotsi, Guidelines for Synthesis and Processing of Two-Dimensional Titanium Carbide (Ti3C2T x MXene), Chemistry of Materials, 29 (2017) 7633-7644.

[30] M.Q. Zhao, C.E. Ren, Z. Ling, M.R. Lukatskaya, C. Zhang, K.L. Van Aken, M.W. Barsoum, Y. Gogotsi, Flexible MXene/carbon nanotube composite paper with high volumetric capacitance, Advanced Materials, 27 (2015) 339-345.

[31] M. Naguib, O. Mashtalir, J. Carle, V. Presser, J. Lu, L. Hultman, Y. Gogotsi, M.W. Barsoum, Two-dimensional transition metal carbides, ACS Nano, 6 (2012) 1322-1331.

[32] M. Naguib, J. Come, B. Dyatkin, V. Presser, P.-L. Taberna, P. Simon, M.W. Barsoum, Y. Gogotsi, MXene: a promising transition metal carbide anode for lithium-ion batteries, Electrochemistry Communications, 16 (2012) 61-64.

[33] M. Naguib, J. Halim, J. Lu, K.M. Cook, L. Hultman, Y. Gogotsi, M.W. Barsoum, New two-dimensional niobium and vanadium carbides as promising materials for Li-ion batteries, Journal of the American Chemical Society, 135 (2013) 15966-15969.

[34] O. Mashtalir, M.R. Lukatskaya, M.Q. Zhao, M.W. Barsoum, Y. Gogotsi, Amine-Assisted Delamination of Nb2C MXene for Li-Ion Energy Storage Devices, Advanced Materials, 27 (2015) 3501-3506.

[35] Z. Lin, D. Sun, Q. Huang, J. Yang, M.W. Barsoum, X. Yan, Carbon nanofiber bridged two-dimensional titanium carbide as a superior anode for lithium-ion batteries, Journal of Materials Chemistry A, 3 (2015) 14096-14100.

[36] Z.W. Seh, K.D. Fredrickson, B. Anasori, J. Kibsgaard, A.L. Strickler, M.R. Lukatskaya, Y. Gogotsi, T.F. Jaramillo, A. Vojvodic, Two-dimensional molybdenum carbide (MXene) as an efficient electrocatalyst for hydrogen evolution, ACS Energy Letters, 1 (2016) 589-594.

[37] H.-Y. Chung, M.B. Weinberger, J.B. Levine, A. Kavner, J.-M. Yang, S.H. Tolbert, R.B. Kaner, Synthesis of ultra-incompressible superhard rhenium diboride at ambient pressure, Science, 316 (2007) 436-439.

[38] P. Rogl, H. Nowotny, Studies of the (Sc, Zr, Hf)-(Rh, Ir)-B systems, Journal of the Less Common Metals, 67 (1979) 41-50.

[39] R. Kiessling, The borides of some transition elements, Journal of Electrochemical Society, 98 (1951) 166.

[40] T. Bjurström, Röntgenanalyse der systeme eisen-bor, kobalt-bor und nickel-bor, Friedländer, Almqvist & Wiksell, 1933.

[41] F. Bertaut, P. Blum, Etude des borures de chrome, COMPTES RENDUS HEBDOMADAIRES DES SEANCES DE L ACADEMIE DES SCIENCES, 236 (1953) 1055-1056.

[42] A.K. Iyer, Y. Zhang, J.P. Scheifers, B.P. Fokwa, Structural variations, relationships and properties of M2B metal borides, Journal of Solid State Chemistry, 270 (2019) 618-635.

[43] M. Sagawa, S. Fujimura, N. Togawa, H. Yamamoto, Y. Matsuura, New material for permanent magnets on a base of Nd and Fe, Journal of Applied Physics, 55 (1984) 2083-2087.

[44] J. Nagamatsu, N. Nakagawa, T. Muranaka, Y. Zenitani, J. Akimitsu, Superconductivity at 39 K in magnesium diboride, Nature, 410 (2001) 63-64.

[45] H. Park, A. Encinas, J.P. Scheifers, Y. Zhang, B.P. Fokwa, Boron-Dependency of Molybdenum Boride Electrocatalysts for the Hydrogen Evolution Reaction, Angewandte Chemie International Edition, 56 (2017) 5575-5578.

[46] Y. Zhou, H. Xiang, F.-Z. Dai, Z. Feng, Electrical conductive and damage-tolerant nanolaminated MAB phases Cr2AlB2, Cr3AlB4 and Cr4AlB6, Materials Research Letters, 5 (2017) 440-448.

[47] Y. Zhou, H. Xiang, F.-Z. Dai, Z. Feng, Cr5Si3B and Hf5Si3B: New MAB phases with anisotropic electrical, mechanical properties and damage tolerance, Journal of Materials Science & Technology, 34 (2018) 1441-1448.

[48] J. Liu, S. Li, B. Yao, J. Zhang, X. Lu, Y. Zhou, Thermal stability and thermal shock resistance of Fe2AlB2, Ceramics International, 44 (2018) 16035-16039.

[49] F. Halla, W. Thury, Über boride von Molybdän und Wolfram, Zeitschrift für Anorganische und Allgemeine Chemie, 249 (1942) 229-237.

[50] W. Jeitschko, Die Kristallstruktur von MoAlB, Monatshefte für Chemie und verwandte Teile anderer Wissenschaften, 97 (1966) 1472-1476.

[51] Y. Zhang, S. Okada, T. Atoda, T. Yamabe, I. Yasumori, Synthesis of a new compound WAlB by the use of aluminium flux, Yogyo-Kyokai-Shi(Journal of Ceramic Society Japan), 95 (1987) 374-380.

[52] H. Becher, K. Krogmann, E. Peisker, Über das ternäre borid Mn2AlB2, Zeitschrift für Anorganische und Allgemeine Chemie, 344 (1966) 140-147.

[53] N. Chaban, I. KUZ'MA, Ternary systems Cr-Al-B and Mn-Al-B, Akademiia Nauk SSSR, Izvestiia, Neorganicheskie Materialy, 9 (1973) 1908-1911.

[54] K. Petry, W. Jung, Ternäre Boride der Rutheniums mit Aluminium und Zink, Zeitschrift Fur Kristallographie, 182 (1988) 153.

[55] Y. Zhou, H. Xiang, F.Z. Dai, Z. Feng, Y5Si2B8: A theoretically predicted new damage-tolerant MAB phase with layered crystal structure, Journal of American Ceramic Society, 101 (2018) 2459-2470.

[56] M. Dahlqvist, Q. Tao, J. Zhou, J. Palisaitis, P.O. Persson, J. Rosen, Theoretical Prediction and Synthesis of a Family of Atomic Laminate Metal Borides with In-Plane Chemical Ordering, Journal of the American Chemical Society, 142 (2020) 18583-18591.

[57] F. Failamani, R. Podloucky, J. Bursik, G. Rogl, H. Michor, H. Müller, E. Bauer, G. Giester, P. Rogl, Boron-phil and boron-phob structure units in novel borides Ni3Zn2B and Ni2ZnB: experiment and first principles calculations, Dalton Transactions, 47 (2018) 3303-3320.

[58] Z.P. Malik, O. Sologub, A. Grytsiv, G. Giester, P.F. Rogl, Crystal Structure of Novel Ni–Zn Borides: First Observation of a Boron–Metal Nested Cage Unit: B20Ni6, Inorganic Chemistry, 50 (2011) 7669-7675.

[59] A.G. Z Malik, P Rogl, G Giester, J Bursik, Phase relations and structural features in the system Ni–Zn–B, Journal of Solid State Chemistry 198 (2013) 150-161.

[60] Z. Malik, A. Grytsiv, H. Michor, G. Rogl, S. Puchegger, H. Müller, M. Kriegisch, E. Bauer, C. Eisenmenger-Sittner, P. Rogl, Physical properties of the ternary borides Ni21Zn2B20 and Ni3ZnB2, Journal of Alloys and Compounds, 550 (2013) 302-307.

[61] T. Rackl, L. Eisenburger, R. Niklaus, D. Johrendt, Syntheses and physical properties of the MAX phase boride Nb 2 SB and the solid solutions N b 2 S B x C 1− x (x= 0–1), Physical Review Materials, 3 (2019) 054001.

[62] T. Rackl, D. Johrendt, The MAX phase borides Zr2SB and Hf2SB, Solid State Sciences, 106 (2020) 106316.

[63] H. Zhang, H. Xiang, F.-z. Dai, Z. Zhang, Y. Zhou, First demonstration of possible two-dimensional MBene CrB derived from MAB phase Cr2AlB2, Journal of Materials Science & Technology, 34 (2018) 2022-2026.

[64] S. Kota, W. Wang, J. Lu, V. Natu, C. Opagiste, G. Ying, L. Hultman, S.J. May, M.W. Barsoum, Magnetic properties of Cr2AlB2, Cr3AlB4, and CrB powders, Journal of Alloys and Compounds, 767 (2018) 474-482.

[65] H. Zhang, F.-z. Dai, H. Xiang, Z. Zhang, Y. Zhou, Crystal structure of Cr4AlB4: A new MAB phase compound discovered in Cr-Al-B system, Journal of Materials Science & Technology, 35 (2019) 530-534.

[66] L.T. Alameda, C.F. Holder, J.L. Fenton, R.E. Schaak, Partial etching of Al from MoAlB single crystals to expose catalytically active basal planes for the hydrogen evolution reaction, Chemistry of Materials, 29 (2017) 8953-8957.

[67] S. Kota, Y. Chen, J. Wang, S.J. May, M. Radovic, M.W. Barsoum, Synthesis and characterization of the atomic laminate Mn2AlB2, Journal of European Ceramic Society, 38 (2018) 5333-5340.

[68] L. Verger, S. Kota, H. Roussel, T. Ouisse, M. Barsoum, Anisotropic thermal expansions of select layered ternary transition metal borides: MoAlB, Cr2AlB2, Mn2AlB2, and Fe2AlB2, Journal of Applied Physics, 124 (2018) 205108.

[69] L. Lewis, R. Barua, B. Lejeune, Developing magnetofunctionality: Coupled structural and magnetic phase transition in AlFe2B2, Journal of Alloys and Compounds, 650 (2015) 482-488.

[70] A.A. Rezaie, Z. Yan, J.P. Scheifers, J. Zhang, J. Guo, B.P.T. Fokwa, Synthesis and Li-ion Electrode Properties of Layered MAB phases Nin+1ZnBn (n = 1, 2), Journal of Materials Chemistry A, 8, (2020) 1646-1651.

[71] W. Jung, K. Petry, TERNARY BORIDES OF RUTHENIUM WITH ALUMINUM AND ZINC, ZEITSCHRIFT FUR KRISTALLOGRAPHIE, R OLDENBOURG VERLAG ROSENHEIMER STR 145 POSTFACH 801360, W-8000 MUNICH 80 …, 1988, pp. 153-154.

[72] J. Wang, T.-N. Ye, Y. Gong, J. Wu, N. Miao, T. Tada, H. Hosono, Discovery of hexagonal ternary phase Ti 2 InB 2 and its evolution to layered boride TiB, Nature Communications, 10 (2019) 1-8.

[73] H. Zhang, F.-Z. Dai, H. Xiang, X. Wang, Z. Zhang, Y. Zhou, Phase pure and well crystalline Cr2AlB2: A key precursor for two-dimensional CrB, Journal of Materials Science & Technology, 35 (2019) 1593-1600.

[74] L.T. Alameda, P. Moradifar, Z.P. Metzger, N. Alem, R.E. Schaak, Topochemical deintercalation of Al from MoAlB: stepwise etching pathway, layered intergrowth structures, and two-dimensional MBene, Journal of the American Chemical Society, 140 (2018) 8833-8840.

[75] L.T. Alameda, R.W. Lord, J.A. Barr, P. Moradifar, Z.P. Metzger, B.C. Steimle, C.F. Holder, N. Alem, S.B. Sinnott, R.E. Schaak, Multi-Step Topochemical Pathway to Metastable Mo2AlB2 and Related Two-Dimensional Nanosheet Heterostructures, Journal of the American Chemical Society, 141 (2019) 10852-10861.

[76] Z. Jiang, P. Wang, X. Jiang, J. Zhao, MBene (MnB): a new type of 2D metallic ferromagnet with high Curie temperature, Nanoscale Horizons, 3 (2018) 335-341.

[77] B. Zhang, J. Zhou, Z. Guo, Q. Peng, Z. Sun, Two-dimensional chromium boride MBenes with high HER catalytic activity, Applied Surface Sciences, 500 (2020) 144248.

[78] Z. Guo, J. Zhou, Z. Sun, New two-dimensional transition metal borides for Li ion batteries and electrocatalysis, Journal of Materials Chemistry A, 5 (2017) 23530-23535.

[79] J. Rodriguez-Carvajal, FullProf 2000: A Rietveld refinement and pattern matching analysis program, Version: April, (2008).

[80] M.R. Lukatskaya, O. Mashtalir, C.E. Ren, Y. Dall'Agnese, P. Rozier, P.L. Taberna, M. Naguib, P. Simon, M.W. Barsoum, Y. Gogotsi, Cation intercalation and high volumetric capacitance of two-dimensional titanium carbide, Science, 341 (2013) 1502-1505.

[81] F. Shahzad, M. Alhabeb, C.B. Hatter, B. Anasori, S.M. Hong, C.M. Koo, Y. Gogotsi, Electromagnetic interference shielding with 2D transition metal carbides (MXenes), Science, 353 (2016) 1137-1140.

[82] Z. Guo, L. Zhu, J. Zhou, Z. Sun, Microscopic origin of MXenes derived from layered MAX phases, RSC Advances, 5 (2015) 25403-25408.

[83] J. Stuart, M. Lefler, C.P. Rhodes, S. Licht, High Energy Capacity TiB2/VB2 Composite Metal Boride Air Battery, Journal of Electrochemical Society, 162 (2015) A432-A436.

[84] H. Yang, Y. Wang, X. Ai, C. Cha, Metal borides: competitive high capacity anode materials for aqueous primary batteries, Electrochemical Solid-State Letters, 7 (2004) A212-A215.

[85] A. Manthiram, J.C. Knight, S.T. Myung, S.M. Oh, Y.K. Sun, Nickel-rich and lithium-rich layered oxide cathodes: progress and perspectives, Advanced Energy Materials, 6 (2016) 1501010.

[86] N. Nitta, F. Wu, J.T. Lee, G. Yushin, Li-ion battery materials: present and future, Materials Today, 18 (2015) 252-264.

[87] S.S. S Bhan, A Lal, The B--Ni--Zn(Boron--Nickel--Zinc) System, Journal of Alloy Phase Diagrams(India), 6 (1990) 147-152.

[88] A.J. Bard, M.A. Fox, Artificial photosynthesis: solar splitting of water to hydrogen and oxygen, Accounts of Chemical Research, 28 (1995) 141-145.

[89] J.D. Holladay, J. Hu, D.L. King, Y. Wang, An overview of hydrogen production technologies, Catalysis Today, 139 (2009) 244-260.

[90] J. Feng, F. Lv, W. Zhang, P. Li, K. Wang, C. Yang, B. Wang, Y. Yang, J. Zhou, F. Lin, Iridium-based multimetallic porous hollow nanocrystals for efficient overall-water-splitting catalysis, Advanced Materials, 29 (2017) 1703798.

[91] Z.A. Piazza, H.-S. Hu, W.-L. Li, Y.-F. Zhao, J. Li, L.-S. Wang, Planar hexagonal B 36 as a potential basis for extended single-atom layer boron sheets, Nature Communications, 5 (2014) 3113.

[92] A.J. Mannix, X.-F. Zhou, B. Kiraly, J.D. Wood, D. Alducin, B.D. Myers, X. Liu, B.L. Fisher, U. Santiago, J.R. Guest, Synthesis of borophenes: Anisotropic, two-dimensional boron polymorphs, Science, 350 (2015) 1513-1516.

[93] H. Liu, A.T. Neal, Z. Zhu, Z. Luo, X. Xu, D. Tománek, P.D. Ye, Phosphorene: an unexplored 2D semiconductor with a high hole mobility, ACS Nano, 8 (2014) 4033-4041.

[94] B. Hinnemann, P.G. Moses, J. Bonde, K.P. Jørgensen, J.H. Nielsen, S. Horch, I. Chorkendorff, J.K. Nørskov, Biomimetic hydrogen evolution: MoS2 nanoparticles as catalyst for hydrogen evolution, Journal of the American Chemical Society, 127 (2005) 5308-5309.

[95] R.J. Toh, Z. Sofer, J. Luxa, D. Sedmidubský, M. Pumera, 3R phase of MoS 2 and WS 2 outperforms the corresponding 2H phase for hydrogen evolution, Chemical Communications, 53 (2017) 3054-3057.

[96] T.F. Jaramillo, K.P. Jørgensen, J. Bonde, J.H. Nielsen, S. Horch, I. Chorkendorff, Identification of active edge sites for electrochemical H2 evolution from MoS2 nanocatalysts, Science, 317 (2007) 100-102.

[97] A.A. Rezaie, E. Lee, D. Luong, J.A. Yapo, B.P. Fokwa, Abundant Active Sites on the Basal Plane and Edges of Layered van der Waals Fe3GeTe2 for Highly Efficient Hydrogen Evolution, ACS Materials Letters, 3 (2021) 313-319.

[98] N.F. Rosli, M.Z.M. Nasir, N. Antonatos, Z.k. Sofer, A. Dash, J. Gonzalez-Julian, A.C. Fisher, R.D. Webster, M. Pumera, MAX and MAB Phases: Two-Dimensional Layered Carbide and Boride Nanomaterials for Electrochemical Applications, ACS Applied Nano Materials, 2 (2019) 6010-6021.

[99] B. Ding, W.-J. Ong, J. Jiang, X. Chen, N. Li, Uncovering the electrochemical mechanisms for hydrogen evolution reaction of heteroatom doped M2C MXene (M= Ti, Mo), Applied Surface Sciences, 500 (2020) 143987.

[100] S. Kota, M. Sokol, M.W. Barsoum, A progress report on the MAB phases: atomically laminated, ternary transition metal borides, International Materials Reviews, 65 (2020) 226-255.

[101] D.K. Mann, J. Xu, N.E. Mordvinova, V. Yannello, Y. Ziouani, N. González-Ballesteros, J.P. Sousa, O.I. Lebedev, Y.V. Kolen'ko, M. Shatruk, Electrocatalytic water oxidation over AlFe 2 B 2, Chemical Science, 10 (2019) 2796-2804.

[102] B. Li, Y. Wu, N. Li, X. Chen, X. Zeng, Arramel, X. Zhao, J. Jiang, Single-metal atoms supported on MBenes for robust electrochemical hydrogen evolution, ACS Applied Materials & Interfaces, 12 (2020) 9261-9267.

[103] M. Yao, Z. Shi, P. Zhang, W.-J. Ong, J. Jiang, W.-Y. Ching, N. Li, Density Functional Theory Study of Single Metal Atoms Embedded into MBene for Electrocatalytic Conversion of N2 to NH3, ACS Applied Nano Materials, 3 (2020) 9870-9879.

[104] H. Park, Y. Zhang, E. Lee, P. Shankhari, B.P. Fokwa, High-Current-Density HER Electrocatalysts: Graphene-like Boron Layer and Tungsten as Key Ingredients in Metal Diborides, ChemSusChem, 12 (2019) 3726-3731.

[105] H. Park, E. Lee, M. Lei, H. Joo, S. Coh, B.P. Fokwa, Canonic-Like HER Activity of Cr1–xMoxB2 Solid Solution: Overpowering Pt/C at High Current Density, Advanced Materials, 32 (2020) 2000855.

[106] Y. Okamoto, Y. Nitta, T. Imanaka, S. Teranishi, Surface characterisation of nickel boride and nickel phosphide catalysts by X-ray photoelectron spectroscopy, Journal of the Chemical Society, Faraday Transactions 1: Physical Chemistry in Condensed Phases, 75 (1979) 2027-2039.

[107] H. Sun, Y. Ye, Z. Tian, S. Wu, J. Liu, C. Liang, Ni 3+ doped cobalt–nickel layered double hydroxides as high-performance electrode materials for supercapacitors, RSC Advances, 7 (2017) 49010-49014.

[108] E. Diler, B. Lescop, S. Rioual, G.N. Vien, D. Thierry, B. Rouvellou, Initial formation of corrosion products on pure zinc and MgZn2 examinated by XPS, Corrosion Science, 79 (2014) 83-88.

[109] E. Lee, H. Park, H. Joo, B.P. Fokwa, Unexpected Correlation Between Boron Chain Condensation and Hydrogen Evolution Reaction (HER) Activity in Highly Active Vanadium Borides: Enabling Predictions, Angewandte Chemie International Edition, 59 (2020) 11774-11778.

[110] W. Zhou, M. Chen, M. Guo, A. Hong, T. Yu, X. Luo, C. Yuan, W. Lei, S. Wang, Magnetic enhancement for hydrogen evolution reaction on ferromagnetic MoS2 catalyst, Nano Letters, 20 (2020) 2923-2930.

[111] D.Y. Chung, S.-K. Park, Y.-H. Chung, S.-H. Yu, D.-H. Lim, N. Jung, H.C. Ham, H.-Y. Park, Y. Piao, S.J. Yoo, Edge-exposed MoS 2 nano-assembled structures as efficient electrocatalysts for hydrogen evolution reaction, Nanoscale, 6 (2014) 2131-2136.

[112] W. Sheng, H.A. Gasteiger, Y. Shao-Horn, Hydrogen oxidation and evolution reaction kinetics on platinum: acid vs alkaline electrolytes, Journal of Electrochemical Society, 157 (2010) B1529.

[113] E. Skúlason, G. S. Karlberg, J. Rossmeisl, T. Bligaard, J. Greeley, H. Jónsson, J. K. Nørskov, Physical Chemistry Chemical Physics, 9 (2007) 3241-3250.

[114] C. Tsai, K. Chan, J.K. Nørskov, F. Abild-Pedersen, Theoretical insights into the hydrogen evolution activity of layered transition metal dichalcogenides, Surface Sciences, 640 (2015) 133-140.

[115] S. Gupta, M.K. Patel, A. Miotello, N. Patel, Metal boride-based catalysts for electrochemical water-splitting: A review, Advanced Functunal Materials, 30 (2020) 1906481.

[116] C. Mattevi, H. Kim, M. Chhowalla, A review of chemical vapour deposition of graphene on copper, Journal of Materials Chemistry, 21 (2011) 3324-3334.

[117] J. Jeon, S.K. Jang, S.M. Jeon, G. Yoo, Y.H. Jang, J.-H. Park, S. Lee, Layer-controlled CVD growth of large-area two-dimensional MoS 2 films, Nanoscale, 7 (2015) 1688-1695.

[118] A. Yousaf, M.S. Gilliam, S.L. Chang, M. Augustin, Y. Guo, F. Tahir, M. Wang, A. Schwindt, X.S. Chu, D.O. Li, Exfoliation of Quasi-Two-Dimensional Nanosheets of Metal Diborides, The Journal of Physical Chemistry C, 125 (2021) 6787-6799.

[119] Y. Guo, A. Gupta, M.S. Gilliam, A. Debnath, A. Yousaf, S. Saha, M.D. Levin, A.A. Green, A.K. Singh, Q.H. Wang, Exfoliation of boron carbide into ultrathin nanosheets, Nanoscale, 13 (2021) 1652-1662.

[120] J. Shen, Y. He, J. Wu, C. Gao, K. Keyshar, X. Zhang, Y. Yang, M. Ye, R. Vajtai, J. Lou, Liquid phase exfoliation of two-dimensional materials by directly probing and matching surface tension components, Nano Letters, 15 (2015) 5449-5454.

[121] H. Nishino, T. Fujita, N.T. Cuong, S. Tominaka, M. Miyauchi, S. Iimura, A. Hirata, N. Umezawa, S. Okada, E. Nishibori, Formation and characterization of hydrogen boride sheets derived from MgB2 by cation exchange, Journal of the American Chemical Society, 139 (2017) 13761-13769.

[122] S.K. Das, K. Jasuja, Chemical exfoliation of layered magnesium diboride to yield functionalized nanosheets and nanoaccordions for potential flame retardant applications, ACS Applied Nano Materials, 1 (2018) 1612-1622.

[123] A.A. Rezaie, E. Lee, J.A. Yapo, B.P.T. Fokwa, Highly Active and Abundant MAB Phases Nin+1ZnBn (n = 1, 2) toward Hydrogen Evolution, Advanced Energy and Sustainability Research, (2021) 2100052.

[124] H. Nishino, T. Fujita, A. Yamamoto, T. Fujimori, A. Fujino, S.-i. Ito, J. Nakamura, H. Hosono, T. Kondo, Formation mechanism of boron-based nanosheet through the reaction of MgB2 with water, The Journal of Physical Chemistry C, 121 (2017) 10587-10593.

[125] J. Chow, R.J. Kopp, P.R. Portney, Energy resources and global development, Science, 302 (2003) 1528-1531.

[126] I. Roger, M.A. Shipman, M.D. Symes, Earth-abundant catalysts for electrochemical and photoelectrochemical water splitting, Nature Reviews Chemistry, 1 (2017) 1-13.

[127] J.A. Turner, Sustainable hydrogen production, Science, 305 (2004) 972-974.

[128] F. Bonaccorso, L. Colombo, G. Yu, M. Stoller, V. Tozzini, A.C. Ferrari, R.S. Ruoff, V. Pellegrini, Graphene, related two-dimensional crystals, and hybrid systems for energy conversion and storage, Science, 347 (2015) 1246501.

[129] Z. Xie, P. He, L. Du, F. Dong, K. Dai, T. Zhang, Comparison of four nickel-based electrodes for hydrogen evolution reaction, Electrochimica Acta, 88 (2013) 390-394.

[130] C.C. McCrory, S. Jung, I.M. Ferrer, S.M. Chatman, J.C. Peters, T.F. Jaramillo, Benchmarking hydrogen evolving reaction and oxygen evolving reaction electrocatalysts for solar water splitting devices, Journal of American Chemical Society, 137 (2015) 4347-4357.

[131] N.S. Lewis, D.G. Nocera, Powering the planet: Chemical challenges in solar energy utilization, Proceedings of the National Academy of Sciences, 103 (2006) 15729-15735.

[132] T.R. Cook, D.K. Dogutan, S.Y. Reece, Y. Surendranath, T.S. Teets, D.G. Nocera, Solar energy supply and storage for the legacy and nonlegacy worlds, Chemical Reviews, 110 (2010) 6474-6502.

[133] S. Park, Y. Shao, J. Liu, Y. Wang, Oxygen electrocatalysts for water electrolyzers and reversible fuel cells: status and perspective, Energy & Environmental Science, 5 (2012) 9331-9344.

[134] J. Dillon Jr, H. Kamimura, J. Remeika, Magneto-optical properties of ferromagnetic chromium trihalides, Journal of Physics and Chemistry of Solids, 27 (1966) 1531-1549.

[135] R. Mas-Balleste, C. Gomez-Navarro, J. Gomez-Herrero, F. Zamora, 2D materials: to graphene and beyond, Nanoscale, 3 (2011) 20-30.

[136] K.F. Mak, J. Shan, Photonics and optoelectronics of 2D semiconductor transition metal dichalcogenides, Nature Photonics, 10 (2016) 216.

[137] E. Pomerantseva, Y. Gogotsi, Two-dimensional heterostructures for energy storage, Nature Energy, 2 (2017) 1-6.

[138] H. Li, C. Tsai, A.L. Koh, L. Cai, A.W. Contryman, A.H. Fragapane, J. Zhao, H.S. Han, H.C. Manoharan, F. Abild-Pedersen, Activating and optimizing MoS 2 basal planes for hydrogen evolution through the formation of strained sulphur vacancies, Nature materials, 15 (2016) 48-53.

[139] D. Voiry, R. Fullon, J. Yang, C.d.C.C. e Silva, R. Kappera, I. Bozkurt, D. Kaplan, M.J. Lagos, P.E. Batson, G. Gupta, The role of electronic coupling between substrate and 2D MoS 2 nanosheets in electrocatalytic production of hydrogen, Nature Materials, 15 (2016) 1003-1009.

[140] Y. Wang, Y. Li, T. Heine, PtTe Monolayer: Two-Dimensional Electrocatalyst with High Basal Plane Activity toward Oxygen Reduction Reaction, Journal of the American Chemical Society, 140 (2018) 12732-12735.

[141] Y. Zhao, J. Gu, Z. Chen, Oxygen Evolution Reaction on 2D Ferromagnetic Fe3GeTe2: Boosting the Reactivity by the Self-Reduction of Surface Hydroxyl, Advanced Functunal Materials, 29 (2019) 1904782.

[142] D. Li, Y. Jia, G. Chang, J. Chen, H. Liu, J. Wang, Y. Hu, Y. Xia, D. Yang, X. Yao, A defect-driven metal-free electrocatalyst for oxygen reduction in acidic electrolyte, Chem, 4 (2018) 2345-2356.

[143] Y. Li, K. Yin, L. Wang, X. Lu, Y. Zhang, Y. Liu, D. Yan, Y. Song, S. Luo, Engineering MoS2 nanomesh with holes and lattice defects for highly active hydrogen evolution reaction, Applied Catalysis B: Environmental, 239 (2018) 537-544.

[144] G. Ou, P. Fan, X. Ke, Y. Xu, K. Huang, H. Wei, W. Yu, H. Zhang, M. Zhong, H. Wu, Defective molybdenum sulfide quantum dots as highly active hydrogen evolution electrocatalysts, Nano Research, 11 (2018) 751-761.

[145] Z. Zhu, H. Yin, C.T. He, M. Al-Mamun, P. Liu, L. Jiang, Y. Zhao, Y. Wang, H.G. Yang, Z. Tang, Ultrathin transition metal dichalcogenide/3d metal hydroxide hybridized nanosheets to enhance hydrogen evolution activity, Advanced Materials, 30 (2018) 1801171.

[146] M.-R. Gao, J.-X. Liang, Y.-R. Zheng, Y.-F. Xu, J. Jiang, Q. Gao, J. Li, S.-H. Yu, An efficient molybdenum disulfide/cobalt diselenide hybrid catalyst for electrochemical hydrogen generation, Nature Communications, 6 (2015) 1-7.

[147] H. Hong, C. Liu, T. Cao, C. Jin, S. Wang, F. Wang, K. Liu, Interfacial engineering of van der waals coupled 2D layered materials, Advanced Materials Interfaces, 4 (2017) 1601054.

[148] Y. Qin, H.-H. Wu, L.A. Zhang, X. Zhou, Y. Bu, W. Zhang, F. Chu, Y. Li, Y. Kong, Q. Zhang, Aluminum and nitrogen codoped graphene: Highly active and durable electrocatalyst for oxygen reduction reaction, ACS Catalysis, 9 (2018) 610-619.

[149] Z. Luo, Y. Ouyang, H. Zhang, M. Xiao, J. Ge, Z. Jiang, J. Wang, D. Tang, X. Cao, C. Liu, Chemically activating MoS 2 via spontaneous atomic palladium interfacial doping towards efficient hydrogen evolution, Nature Communications, 9 (2018) 1-8.

[150] Y. Zhao, J. Wan, H. Yao, L. Zhang, K. Lin, L. Wang, N. Yang, D. Liu, L. Song, J. Zhu, Few-layer graphdiyne doped with sp-hybridized nitrogen atoms at acetylenic sites for oxygen reduction electrocatalysis, Nature Chemistry, 10 (2018) 924-931.

[151] N.K. Abrikosov, L. Bagaeva, L. Dudkin, Phase equilibria in Fe-Ge-Te system, Izv. Akad. Nauk SSSR, Neorg. Mater, 21 (1985) 1680-1686.

[152] H.J. Deiseroth, K. Aleksandrov, C. Reiner, L. Kienle, R.K. Kremer, Fe3GeTe2 and Ni3GeTe2–Two New Layered Transition-Metal Compounds: Crystal Structures, HRTEM Investigations, and Magnetic and Electrical Properties, Europeen Journal of Inorganic Chemistry,, 2006 (2006) 1561-1567.

[153] Z. Cui, C. Xiao, Y. Lv, Q. Li, R. Sa, Z. Ma, Adsorption behavior of CO, CO2, H2, H2O, NO, and O2 on pristine and defective 2D monolayer Ferromagnetic Fe3GeTe2, Applied Surface Sciences, 527 (2020) 146894.

[154] Y. Yan, B.Y. Xia, X. Ge, Z. Liu, A. Fisher, X. Wang, A flexible electrode based on iron phosphide nanotubes for overall water splitting, Chemistry–A European Journal, 21 (2015) 18062-18067.

[155] A.P. Grosvenor, S.D. Wik, R.G. Cavell, A. Mar, Examination of the bonding in binary transition-metal monophosphides MP (M= Cr, Mn, Fe, Co) by X-ray photoelectron spectroscopy, Inorganic Chemistry, 44 (2005) 8988-8998.

[156] R. Li, L. Zhang, L. Shi, P. Wang, MXene Ti3C2: An Effective 2D Light-to-Heat Conversion Material, ACS Nano, 11 (2017) 3752-3759.

[157] R. Liang, L. Shen, F. Jing, N. Qin, L. Wu, Preparation of MIL-53 (Fe)-reduced graphene oxide nanocomposites by a simple self-assembly strategy for increasing interfacial contact: efficient visible-light photocatalysts, ACS Applied Materials & Interfaces, 7 (2015) 9507-9515.

[158] V. Grossi, L. Ottaviano, S. Santucci, M. Passacantando, XPS and SEM studies of oxide reduction of germanium nanowires, Journal of Non-crystalline Solids, 356 (2010) 1988-1993.

[159] Y. Huang, J.-P. Xu, L. Liu, P.-T. Lai, W.-M. Tang, N 2-Plasma-Treated Ga 2 O 3 (Gd 2 O 3) as Interface Passivation Layer for Ge MOS Capacitor With HfTiON Gate Dielectric, IEEE Transactions on Electron Devices, 63 (2016) 2838-2843.

[160] Q. Xie, S. Deng, M. Schaekers, D. Lin, M. Caymax, A. Delabie, X.-P. Qu, Y.-L. Jiang, D. Deduytsche, C. Detavernier, Germanium surface passivation and atomic layer deposition of high-k dielectrics—A tutorial review on Ge-based MOS capacitors, Semiconductor Science and Technology, 27 (2012) 074012.

[161] Z. Yang, M. Xu, X. Cheng, H. Tong, X. Miao, Manipulation of dangling bonds of interfacial states coupled in GeTe-rich GeTe/Sb 2 Te 3 superlattices, Scientific Reports, 7 (2017) 1-9.

[162] M.O. Reese, C.L. Perkins, J.M. Burst, S. Farrell, T.M. Barnes, S.W. Johnston, D. Kuciauskas, T.A. Gessert, W.K. Metzger, Intrinsic surface passivation of CdTe, Journal of Applied Physics, 118 (2015) 155305.

[163] J.C. McGlynn, I. Cascallana-Matías, J.P. Fraser, I. Roger, J. McAllister, H.N. Miras, M.D. Symes, A.Y. Ganin, Molybdenum ditelluride rendered into an efficient and stable electrocatalyst for the hydrogen evolution reaction by polymorphic control, Energy Technology, 6 (2018) 345-350.

[164] S. Trasatti, O. Petrii, Real surface area measurements in electrochemistry, Pure and Applied Chemistry, 63 (1991) 711-734.

[165] J.C. McGlynn, T. Dankwort, L. Kienle, N.A. Bandeira, J.P. Fraser, E.K. Gibson, I. Cascallana-Matías, K. Kamarás, M.D. Symes, H.N. Miras, The rapid electrochemical activation of MoTe 2 for the hydrogen evolution reaction, Nature Communications, 10 (2019) 1-9.

[166] H. Park, E. Lee, M. Lei, H. Joo, S. Coh, B.P. Fokwa, Canonic-Like HER Activity of Cr1–xMoxB2 Solid Solution: Overpowering Pt/C at High Current Density, Advanced Materials, 32 (2020) 2000855.

[167] E. Lee, H. Park, H. Joo, B.P. Fokwa, Unexpected Correlation Between Boron Chain Condensation and Hydrogen Evolution Reaction (HER) Activity in Highly Active Vanadium Borides: Enabling Predictions, Angewandte Chemie International Edition, 132 (2020) 11872-11876.

[168] W. Sheng, H.A. Gasteiger, Y. Shao-Horn, Hydrogen oxidation and evolution reaction kinetics on platinum: acid vs alkaline electrolytes, Journal of The Electrochemical Society, 157 (2010) B1529-B1536.

[169] H. You, Z. Zhuo, X. Lu, Y. Liu, Y. Guo, W. Wang, H. Yang, X. Wu, H. Li, T. Zhai, 1T′-MoTe2-Based On-Chip Electrocatalytic Microdevice: A Platform to Unravel Oxidation-Dependent Electrocatalysis, CCS Chemistry, 1 (2019) 396-406.